FPGA IMPLEMENTATION OF FIELD ORIENTED CONTROL FOR PERMANENT MAGNET SYNCHRONOUS MOTOR

A THESIS SUBMITTED TO
THE GRADUATE SCHOOL OF NATURAL AND APPLIED SCIENCES
OF
MIDDLE EAST TECHNICAL UNIVERSITY

BY

GİZEM IRMAK

IN PARTIAL FULFILLMENT OF THE REQUIREMENTS
FOR
THE DEGREE OF MASTER OF SCIENCE
IN
ELECTRICAL AND ELECTRONICS ENGINEERING

DECEMBER 2019

Approval of the thesis:

FPGA IMPLEMENTATION OF FIELD ORIENTED CONTROL FOR PERMANENT MAGNET SYNCHRONOUS MOTOR

submitted by **GİZEM IRMAK** in partial fulfillment of the requirements for the degree of **Master of Science in Electrical and Electronics Engineering Department, Middle East Technical University** by,

Prof. Dr. Halil Kalıpçılar
Dean, Graduate School of **Natural and Applied Sciences** _____

Prof. Dr. İlkay Ulusoy
Head of Department, **Electrical and Electronics Engineering** _____

Assoc. Prof. Dr. Afşar Saranlı
Supervisor, **Electrical and Electronics Engineering, METU** _____

Examining Committee Members:

Prof. Dr. Kemal Leblebicioğlu
Electrical and Electronics Engineering, METU _____

Assoc. Prof. Dr. Afşar Saranlı
Electrical and Electronics Engineering, METU _____

Prof. Dr. Işık Çadırcı
Electrical and Electronics Engineering, Hacettepe University _____

Assist. Prof. Dr. Ozan Keysan
Electrical and Electronics Engineering, METU _____

Assist. Prof. Dr. Emine Bostancı
Electrical and Electronics Engineering, METU _____

Date:

I hereby declare that all information in this document has been obtained and presented in accordance with academic rules and ethical conduct. I also declare that, as required by these rules and conduct, I have fully cited and referenced all material and results that are not original to this work.

Name, Surname: GİZEM IRMAK

Signature :

ABSTRACT

FPGA IMPLEMENTATION OF FIELD ORIENTED CONTROL FOR PERMANENT MAGNET SYNCHRONOUS MOTOR

IRMAK, GİZEM
M.S., Department of Electrical and Electronics Engineering
Supervisor: Assoc. Prof. Dr. Afşar Saranlı

December 2019, 99 pages

The thesis study focuses on the fully operational FPGA implementation for the current/torque control of a Permanent Magnet Synchronous Motor. 3-phase synchronous motors with permanent magnets can be categorized into two categories as Permanent Magnet Synchronous Motor (PMSM) and Brushless Direct Current (BLDC) motor. The main difference between PMSM and BLDC is the shape of the induced back-EMF voltage. While BLDC motors have trapezoidal shaped back-EMF, PMSMs have a sinusoidal back-EMF. In order to take advantage of PMSM, the waveform of motor phase currents should also be created as sinusoidal waveform. For this purpose, Sinusoidal Commutation (SC) and Field Oriented Control (FOC) are the most common strategies in the literature. FOC with Space Vector PWM (SVPWM) is superior to SC in terms of wider speed operation range and higher torque efficiency and hence is the focus of this thesis. Within the scope of our study, Proportional Integral (PI) and Linear Quadratic Regulator (LQR) current and speed controller alternatives are designed. These alternatives are compared in a simulation environment for the considered PMSM. In order to analyze the performance, a detailed system model of the considered PMSM is also created. Matlab/Simulink is used for the construction and

test of the simulation models. For the hardware validation and performance evaluation of the design, the PI current/torque controller is implemented in FPGA using VHDL language. Hardware experimental work is conducted on a custom design electronic board. Torque tracking ability of the current controller is analysed by using a number of test setups. Additionally, comparative performance analysis of the two competing commutation methods, namely the FOC and trapezoidal implementations, has been done. Apart from a fully functional FPGA realization, our study demonstrates the superiority of FOC over trapezoidal commutation in terms of reduction in both torque ripple and required sampling rate.

Keywords: Permanent Magnet Synchronous Motor, Field Oriented Control, Space Vector Pulse Width Modulation, FPGA

ÖZ

SÜREKLİ MIKNATISLI SENKRON MOTORUN ALAN YÖNLENDİRMELİ KONTROLÜNÜN FPGA UYGULAMASI

IRMAK, GİZEM
Yüksek Lisans, Elektrik ve Elektronik Mühendisliği Bölümü
Tez Yöneticisi: Doç. Dr. Afşar Saranlı

Aralık 2019 , 99 sayfa

Bu tez çalışmasında, Sürekli Mıknatıslı Senkron Motor (SMSM) için tasarlanan akım/tork kontrolörün Alan Programlanabilir Kapı Dizini (FPGA) üzerinde gerçekleştirilmesine odaklanılmıştır. Sürekli mıknatıslı üç faz senkron motorlar; SMSM ve Fırçasız Doğru Akım Motoru (FDAM) olmak üzere iki gruba ayrılabilir. SMSM ve FDAM arasındaki ana fark, indüklenen zıt elektromotor kuvvet (EMF) voltajının şeklidir. FDAM üzerinde ikizkenar yamuk biçimli zıt EMF voltajı indüklenirken, SMSM üzerinde ise sinüs biçimli zıt EMF voltajı indüklenir. SMSM'nin avantajlarından faydalanabilmek için, motor faz akımları sinüs biçiminde oluşturulmalıdır. Bu amaçla Alan Yönlendirmeli Kontrol (AYK) ve Sinüs Biçimli Komütasyon (SBK) yöntemleri literatürde sıkça kullanılmaktadır. AYK'nin Uzay Vektör Darbe Genişliği Modülasyonu (UVDGM) bazlı uygulaması, geniş hız çalışma aralığı ve düşük tork dalgalanması sunduğundan SBK'ye göre daha üstündür. Bu nedenle de tezin odak noktası olarak belirlenmiştir. Çalışma kapsamında, Oransal Integral (PI) ve Doğrusal İkinci Derece Düzenleyici (LQR) bazlı akım ve hız kontrolcüleri tasarlanmıştır. Bu iki alternatif kontrolcü, ilgili SMSM baz alınarak benzetim ortamında karşılaştırılmıştır. Performans analizinin yapılabilmesi için, SMSM'nin detaylı benzetimi Matlab/Simulink

üzerinde yapılmıştır. Tasarımın donanım doğrulama ve performans değerlendirme çalışmaları için PI kontrolör, seçilen donanım tasarım dili (VHDL) kullanılarak FPGA üzerinde gerçekleştirilmiştir. Donanım deneysel çalışmaları, özel tasarım elektronik bir kart üzerinde yürütülmüştür. Akım kontrolcünün akım/tork takip yeteneği çeşitli testler kullanılarak değerlendirilmiştir. Bu çalışmalara ek olarak, AYK ve ikizkenar yamuk biçimli komütasyon metotları arasında da karşılaştırmalı performans analizi yapılmıştır. Bu deneylerin sonucunda, AYK'nin ikizkenar yamuk biçimli komütasyon metodu karşısında daha düşük tork dalgalanması sergilediği ve daha düşük örnekleme oranına ihtiyaç duyduğu gözlenmiştir.

Anahtar Kelimeler: Sürekli Mıknatıslı Senkron Motor, Alan Yönlendirmeli Kontrol, Uzay Vektör Darbe Genişliği Modulasyonu, FPGA

"It is good to have an end to journey toward, but it is the journey that matters in the end."

Ursula Kroeber Le Guin

ACKNOWLEDGMENTS

I would like to express my sincere gratitude to my supervisor Assoc. Prof. Dr. Afşar SARANLI for his guidance, patience, encouragements and insight throughout my research. It has been a great honour and pleasure working with him.

I am very grateful to TÜBİTAK-SAGE (*The Scientific and Technological Research Council of Turkey - Defense Industries Research and Development Institute*) for giving me opportunity to conduct this study and providing the necessary equipment throughout my thesis. Additionally, I would like to show my deepest appreciation to my colleagues, who supported this work in both technical and moral aspects. Also, I am grateful to all my friends for their continuous encouragement.

I would like to extend my sincere gratitude to Önder YAZLIK for his guidance and contributions throughout the preparation of this thesis.

Finally, I want to thank my family for their life long support that motivates me at the every stage of the work. It could have been impossible to write this thesis without their patience and love.

TABLE OF CONTENTS

ABSTRACT v

ÖZ vii

ACKNOWLEDGMENTS x

TABLE OF CONTENTS xi

LIST OF TABLES xvi

LIST OF FIGURES xvii

LIST OF ABBREVIATIONS xxii

CHAPTERS

1 INTRODUCTION AND MOTIVATION 1

1.1 Introduction 1

1.2 Scope and Contributions 2

1.3 Outline of Thesis 3

2 LITERATURE REVIEW 5

2.1 Trapezoidal Commutation 6

2.2 Sinusoidal Commutation 6

2.3 Field Oriented Control 7

2.4 Choice of Commutation Method for Permanent Magnet Motors . . . 7

2.5 PWM Methods for FOC 10

2.6 Motivations for FPGA based Design 10

3 THEORY OF OPERATION 13

3.1 Introduction 13

3.2 Domain Transformation 13

3.3 Mathematical Model of PMSM 15

3.4 Field Oriented Control 16

3.5 Space Vector Pulse Width Modulation 17

3.5.1 Determination of V_{ref} and θ 19

3.5.2 Switching Time Duration T_a, T_b and T_0 19

3.5.3 Space Vector Modulation Scheme 20

3.6 PI Controller Design 21

3.6.1 PI Controller Design Procedure 23

3.6.1.1 PI Controller Loop i_d 23

3.6.1.2 PI Controller Loop for i_q 24

3.6.1.3 PI Controller Loop w_r 25

3.7 State Feedback Controller Design 27

4 HARDWARE DESCRIPTION 31

4.1 Introduction 31

4.2 Electronic Board 32

4.2.1 Control Unit 32

4.2.2 Motor Driver Circuitry 33

4.2.3 Current Sensing Block 33

4.2.4 Position Sensing Block 34

4.3 Focused PMSM 35

5 SIMULINK MODEL 37

5.1 Introduction 37

5.2 Permanent Magnet Synchronous Motor Block 37

5.3 Park Transformation 39

5.4 dq to alpha-beta Transformation 40

5.5 Reference Vector Calculation 40

5.6 Space Vector PWM 41

5.7 Voltage Source Inverter 44

5.8 Verification of the Model 44

5.9 PI Controller Based Design 45

5.9.1 Step Speed Command under Load Torque 47

5.9.2 Speed Reversal Test under Load 48

5.9.3 Chirp Speed Command 49

5.10 LQR Controller Based Design 51

5.10.1 Step Speed Command under Load Torque 53

5.10.2 Speed Reversal Test under Load 55

5.10.3 Chirp Speed Command 58

5.11 Performance Comparison of the Controllers 59

5.11.1 Step Speed Response Behaviour of Controllers 59

5.11.2 Speed Reversal Behaviour of Controllers 60

5.11.3 Conclusion 61

6 FPGA IMPLEMENTATION 63

6.1 Current Controller 63
6.1.1 Motor Feedback Currents Reading 64
6.1.1.1 Currents Acquisition 64
6.1.1.2 Offset Currents Calculation 66
6.1.1.3 Phase Current Summation and Averaging 67
6.1.2 Park Transformation 68
6.1.3 PI Controller 70
6.1.4 Inverse Park Transformation 74
6.1.5 Space Vector PWM Calculation 75
6.1.6 Space Vector PWM Modulation 76
6.1.6.1 Sector Detection 77
6.1.6.2 SVPWM Pulse Time Calculation 78
6.1.6.3 Space Vector Modulation Scheme 78
6.2 Resolver Reading 79
7 EXPERIMENTAL WORK 81
7.1 Introduction 81
7.2 Current Tests 81
7.3 Torque Tests 83
7.3.1 Load Brake Results of FOC Commutation 84
7.3.2 Load Brake Results of Six-Step Commutation 85
7.4 Torque-Speed Tests 87
7.4.1 Torque-Speed Results of FOC Commutation 87
7.4.2 Torque-Speed Results of Six-Step Commutation 88

7.5 Supply Current Measurement under Load Brake 89

7.6 Discussion of the Results 91

8 CONCLUSION AND FUTURE WORKS 93

REFERENCES 95

LIST OF TABLES

TABLES

Table 2.1 Comparison of Commutation Techniques [25], [38], [37] 10

Table 3.1 Timing Characteristics of IRF7580 21

Table 4.1 BM-2706 Parameters 35

Table 5.1 Motor Parameters for Rotor Reference Frame Model 38

Table 5.2 Chirp Signal Parameters 50

Table 5.3 Chirp Signal Parameters for LQR 58

Table 6.1 Current Sensor and ADC Parameters 66

Table 6.2 CORDIC IP for Root Function 76

Table 6.3 CORDIC IP for Arctan Function 76

LIST OF FIGURES

FIGURES

Figure 2.1 Torque Output of Trapezoidal Driven BLDC [37] 8

Figure 2.2 Torque Output of Trapezoidal Driven PMSM [37] 9

Figure 3.1 Clarke and Park Transformations 14

Figure 3.2 abc to dq Transformation [30] 14

Figure 3.3 Rotating dq Reference Frame [8] 15

Figure 3.4 Space Vector Representation [42] 19

Figure 3.5 Switching Patterns for Six Sectors in Circle [42] 20

Figure 3.6 Switching Time Waveforms of IRF7580 [17] 21

Figure 3.7 Block Diagram of Field Oriented Control [3] 22

Figure 3.8 Bode Diagram of i_d Closed Loop 23

Figure 3.9 Step Response of i_d Closed Loop 24

Figure 3.10 Bode Diagram of i_q Closed Loop 25

Figure 3.11 Step Response of i_q Closed Loop 25

Figure 3.12 Bode Diagram of w_r Closed Loop 26

Figure 3.13 Step Response of w_r Closed Loop 26

Figure 3.14 Block Diagram of LQR Controller [8] 28

Figure 4.1 Block Diagram of Control System 31

Figure 4.2 Voltage Source Inverter Topology 33

Figure 5.1 Permanent Magnet Synchronous Machine Motor Block 38

Figure 5.2 PMS Machine Block Symbol 39

Figure 5.3 Configuration of Permanent Magnet Synchronous Machine . . . 39

Figure 5.4 Park Transformation Block 39

Figure 5.5 dq to $\alpha\beta$ transformation 40

Figure 5.6 Reference Voltage Vector Calculation 41

Figure 5.7 Sector Detection 42

Figure 5.8 SVPWM Block 43

Figure 5.9 Voltage Source Inverter Block 44

Figure 5.10 Produced abc and dq Currents, Constant i_q Command, 0 to 0.2 Nm Load 45

Figure 5.11 Produced abc and dq Voltages, Constant i_q Command, 0 to 0.2 Nm Load 45

Figure 5.12 Simulink Model of the System with PI Controller 46

Figure 5.13 Speed Response, Step Command, 0.2 to 0.5 Nm Load 47

Figure 5.14 Produced Torque and Iq, Step Command, 0.2 to 0.5 Nm Load . . 47

Figure 5.15 Feedback abc and dq axis currents, Step Command, 0.2 to 0.5 Nm Load 48

Figure 5.16 Speed Response, Speed Reversal, T=0.3 Nm 48

Figure 5.17 Produced Torque and Iq, Speed Reversal, T=0.3 Nm 49

Figure 5.18 Feedback abc and dq axis currents, Speed Reversal, T_{load}=0.3 Nm 49

Figure 5.19 Speed Response to Chirp Speed Command 50

Figure 5.20 Zoom in Speed Response to Chirp Speed Command 51

Figure 5.21 Simulink Model of the System with LQR Controller 52

Figure 5.22 Speed Response, Step Command, 0.2 to 0.5 Nm Load 53

Figure 5.23 Produced Torque and Iq, Step Command, 0.2 to 0.5 Nm Load . . 54

Figure 5.24 Phase Currents, Step Command 54

Figure 5.25 dq Current Response, Step Command 55

Figure 5.26 Speed Response, Speed Reversal, T=0.3 Nm 56

Figure 5.27 Produced Torque and Iq, Speed Reversal, T=0.3 Nm 56

Figure 5.28 Phase Currents, Speed Reversal, T=0.3 Nm 57

Figure 5.29 dq Current Response, Speed Reversal, T=0.3 Nm 57

Figure 5.30 Speed Response to Chirp Speed Command 58

Figure 5.31 Zoom in Speed Response to Chirp Speed Command 59

Figure 6.1 Functional Block Diagram of Current Controller 63

Figure 6.2 Feedback Current Reading Block 65

Figure 6.3 Current Sampling Scheme 68

Figure 6.4 Park VHDL Block 69

Figure 6.5 PI Controller with Tracking anti-windup [12] 71

Figure 6.6 PI Controller with Conditional anti-windup [12] 72

Figure 6.7 PI VHDL Block 72

Figure 6.8 PI Module State Machine Diagram 73

Figure 6.9 Inverse Park VHDL Block 74

Figure 6.10 Switching Pattern 77

Figure 6.11 Three Phase Bridge Inverter 78

Figure 6.12 Ideal Gate States for Sector-1 79

Figure 6.13 Actual Gate States for Sector-1 79

Figure 7.1 Laboratory Setup for Current Measurements 82

Figure 7.2 dq Current Response, $I_{d_ref} = 0A$, $I_{q_ref} = 1.5A_{pp}$ 300 Hz Rectangular Current Command 82

Figure 7.3 Phase Currents, $I_{d_ref} = 0A$, $I_{q_ref} = 1.5A_{pp}$ 300 Hz Rectangular Current Command 83

Figure 7.4 Locked Shaft Setup 84

Figure 7.5 Measured Torque, 1000 mA I_q Command, FOC 84

Figure 7.6 Measured I_q, 1000 mA I_q Command, FOC 85

Figure 7.7 Torque Test under 2500 mA-pp Square I_q Current Command for FOC 85

Figure 7.8 Measured Torque, 1000 mA Current Command, Six-Step Commutation 86

Figure 7.9 Measured Torque, 3000 mA_{pp} Square Current Command, Six-Step Commutation 86

Figure 7.10 Measured Torque, 2000 mA I_q Command, 0.3 Nm Load, FOC . 88

Figure 7.11 Measured I_q and Speed, 2000 mA I_q Command, 0.3 Nm Load, FOC 88

Figure 7.12 Measured Torque, 3000 mA Current Command, 0.3 Nm Load, Six-Step 89

Figure 7.13 Measured Active Phase Current and Speed, 3000 mA Current Command, 0.3 Nm Load, Six-Step 89

Figure 7.14 Measured Supply Current and Produced Torque, FOC 90

Figure 7.15 Measured Supply Current and Produced Torque, Six-Step 90

LIST OF ABBREVIATIONS

AC	Alternating Current
ADC	Analog-to-Digital Converter
BLDC	Brushless Direct Current
DC	Direct Current
DDR3	Double Data Rate 3
DSP	Digital Signal Processor
DTC	Direct Torque Control
EMF	Electromotive Force
FOC	Field Oriented Control
FLC	Fuzzy Logic Controller
FPGA	Field Programmable Gate Array
IC	Integrated Circuit
IGBT	Insulated Gate Bipolar Transistor
IP	Intellectual Property
LQR	Linear Quadratic Regulator
MOSEET	Metal-Oxide Semiconductor Field-Effect Transistor
MPC	Model Predictive Controller
PCB	Printed Circuit Board
PMSM	Permanent Magnet Synchronous Motor
PWM	Pulse Width Modulation
RAM	Random Access Memory
RPM	Revolution per Minute
SoC	System on Chip
SPWM	Sinusoidal Pulse Width Modulation

SMC	Sliding Mode Controller
SPI	Serial Peripheral Interface
SSI	Serial Synchronous Interface
SVPWM	Space Vector Pulse Width Modulation
THD	Total Harmonic Distortion
THIPWM	Third Harmonic Injection Pulse Width Modulation
VHDL	Very High Speed Integrated Circuit Hardware Description Language
VVC	Voltage Vector Control
v_d, v_q	d, q axis voltages (V)
i_d, i_q	d, q axis currents (A)
L_d, L_q	d, q axis self inductances (H)
R_s	stator resistance per phase (Ω)
λ_d, λ_q	d, q axis flux linkages (Wb)
λ_{af}	mutual flux due to permanent magnet (Wb)
P	number of pole pairs
θ_r	angle between stator phase A and the rotor (rad)
w_r	rotor speed (rad/s)
B	damping constant (N/rad/s)
T_e	electric torque (Nm)
T_l	load torque (Nm)
J	moment of inertia ($Kg.m^2$)
p	derivative operator

CHAPTER 1

INTRODUCTION AND MOTIVATION

1.1 Introduction

Electrical motors convert electrical energy to mechanical energy. They are mainly classified according to phase numbers; single phase and three phase motor. Three phase motors are also divided into two groups as asynchronous and synchronous. Unlike asynchronous motor, synchronous motor runs synchronously with the frequency of AC voltage supply. Permanent Magnet Synchronous Motor (PMSM) is used more and more in different kind of fields such as robotics, machine industry, aerospace, military [9]. This trend results from development in production of high performance permanent magnets. Permanent magnets, which have better performance metrics, residual magnetism and coercivity, lead to higher power density, efficiency, torque to inertia ratio [31]. They have also advantages such as easiness of control, reliability, longer life expectancy, simplicity of control circuits, preferrable size and weight as compared to induction or conventional Direct Current (DC) motors [48]. Fast acceleration and deceleration, improved torque controllability at zero speed, smooth rotation, small torque ripple at low speeds and capability of wide speed range of operation can be listed as the other valuable qualities of PMSMs [3].

Although PMSM and Brushless Direct Current motor (BLDC) belong to the synchronous motor family, their motor construction methodologies also differ in sense of stator windings and rotor magnets [20]. The main difference between PMSM and BLDC results from induced back Electromotive Force (EMF). While BLDC motors have trapezoidal back EMF, PMSMs have sinusoidal back EMF.

PMSM and BLDC have some advantages and disadvantages according to different performance parameters. For instance, PMSM offers better performance in terms of torque smoothness and lower acoustic noise. However, it requires more complex

control scheme and more accurate position information. On the other hand, BLDC offers higher peak torque than PMSM while torque capacity of BLDC deteriorates at high speeds [25]. In order to make use of an advantages of PMSM with sinusoidal back EMF, motor phase currents should be created as sinusoidally shaped waveform. Therefore, use of sinusoidal commutation or Field Oriented Control (FOC) is more preferable to trapezoidal alternative.

The choice between these two commutation methods can be made according to system requirements. Although sinusoidal commutation is relatively easy to implement, FOC is more commonly used. The reason for this choice is wider bandwidth offered by FOC. Since phase currents are expressed as time-varying in sinusoidal commutation, integral components of controllers results in certain amount of delay. Consequently, bandwidth of the system becomes narrower as compared to the other method. In addition to advantages of wider operation range, FOC also offers less Total Harmonic Distortion (THD), improved Power Factor (PF) and less switching losses [1]. Additionally, FOC approach reduces current ripples and improves efficiency. These qualities are sufficient to meet general design constraints. Therefore, design and implementation of FOC will be covered in this thesis.

1.2 Scope and Contributions

In the scope of the thesis, a number of commutation, PWM and controller methods are investigated in order to control PMSM efficiently. As a result of literature survey and system requirements, FOC is intended to be applied with collaboration of SVPWM.

In order to examine the effects of design choices, the system is modelled in MATLAB/Simulink for two different speed controllers. System model is created from scratch by using basic Simulink blocks. Comparative analysis of two speed controller is made. By modelling the system, insight about system is gained. Also, re-usability is intended by designing re-configurable model. By this way, the constructed model can be used for different different PMSM with small modifications on parameter settings.

Since the chosen vector control and PWM strategy have heavy computational requirements, there is a need of high speed computational IC. With the acceleration in IC

design technology, FPGA (Field Programmable Gate Array) has increased capability and resource. Additionally, FPGA offers reduced cost and power consumption as compared to DSP (Digital Signal Processor). Therefore, torque controller is chosen to be implemented on FPGA with use of VHDL (Very High Speed Integrated Circuit Hardware Description Language). During coding process of controller IP (Intellectual Property), required measures are taken so as to achieve reconfigurable controller module. It means that controller could be modified in order to be used in PMSM having different motor constants.

In order to verify the design, different tests are conducted on a hardware. This hardware is an electronic board which is a product of TÜBİTAK SAGE. This board is composed of analog and digital circuits which are responsible of drive and control tasks of the motor. There are several customized board alternatives in industry. Even if one could think that use of industrial cards is practical, it is quite the contrary. Since industrial boards have limited capabilities such as restricted output voltage, motor speed, output current, operating temperature, operating frequency, measures, weight etc. Most of the time, it is hard to match project's specifications with capabilities of an industrial board. Additionally, they do not always offer optimal control algorithms, which causes non-ideal controller performance metrics. Therefore, it is not practical to use custom motor controller/drivers in mission-critical systems.

After explanation of the design and test processes of FOC based controller, another control algorithm based on six-step commutation is examined. Thus it is aimed to observe previously mentioned performance improvement. This comparison clarifies advantages of newly implemented system over commonly preferred six-step method.

1.3 Outline of Thesis

In the rest of the thesis organization will be as following: In Chapter 2, previous works are compared and examined. In Chapter 3, theory behind the implementation of design is discussed. Relevant equations are given and demonstrations are made to clarify the design process. In Chapter 4, system, on which design is realised and experiments are conducted, is described. In Chapter 5, Simulink model of candidate controllers are explained. In Chapter 6, VHDL design process is explained with

VHDL block diagram and state machines. In Chapter 7, different test setups are presented and results of the experiments are discussed. In Chapter 8, overall work, carried out through the thesis, is discussed and future work advices are addressed.

CHAPTER 2

LITERATURE REVIEW

Permanent magnet motors have been studied extensively by researchers because of their efficiency in servo applications. Brushless DC motors and PMSMs are two highly preferred members of this family. In 1988, Pillay and Krishnan derived PMSM mathematical model from previously defined wound rotor synchronous machine model with exceptions about damper windings and excitation [32]. After clarification of mathematical model, a great number of studies have been conducted about the vector control of PMSM.

Field Oriented Control, Voltage Vector Control (VVC) and Direct Torque Control (DTC) could be classified as populer vector control methods, used for PMSM [6]. Direct Torque Control offers simpler structure as compared to FOC since its has no need of pulse width modulation, explicit rotor position except for start-up. Although method is simple and has good dynamic behaviour, it is not suitable for high precision system due to high stator current ripples in steady state [11]. DTC also has some other disadvantages such as requirement of fast sampling time, variable switching frequency and two hysteresis controllers [10]. Voltage Vector Control is another vector control method. It does not require position sensor and coordinate transformation as in case of FOC [10]. Despite of computational simplicity and insensitivity to motor parameters, it suffers from higher torque ripple and overshoot [43].

Assuming that FOC is chosen as a preferred vector control method, it is also possible to classify system further according to speed control strategy. The most investigated control methodologies in the literature can be listed as fuzzy logic, neural networks, PI (Proportional Integral), state space control, sliding mode and model predictive [16].

The FOC method can be also categorized into two main groups as direct and indirect. The difference between direct and indirect FOC is an use of position sensor. Since

position sensor is involved in direct FOC, the control is more accurate and faster as compared with indirect FOC [6].

In contrast to conventional brushed DC motor, commutation takes place in stator instead of rotor in a PMSM. Mechanical commutators are replaced by electronic switches. Electronic switching is realized by three main elements which are DC voltage source, controller and inverter [41]. As previoulsy stated that permanent magnet brushless DC motors can be divided into two groups such as BLDC and PMSM. The one with trapezoidal back EMF is called as BLDC while PMSM have sinusoidally shaped back EMF. Although they differ from each other in terms of back EMF shape, the need of electronic commutation circuitry is common. In addition to this circuitry, commutation strategy is also needed. Trapezoidal (six-step), sinusoidal and field oriented control can be listed as commonly used commutation methods [25].

2.1 Trapezoidal Commutation

Trapezoidal commutation is the simplest strategy among three of them. Only hall-effect sensor is used to realize commutation. There is no need of additional sensor to measure the position. This eases the design effort and cost.

In trapezoidal commutation, only two of the phases are active at any instance. One of them is responsible for sourcing and the other is sinking current. According to the position information obtained from hall sensors, two of the phases are energized. In any position, there is one ideal pair of phases which should be activated in order to get maximum possible torque. As a result of predetermined sequence, six-step commutation is easy to implement. On the other hand, it is also disadvantageous in terms of torque ripple resulting from non-linearities of commutation scheme. Therefore, it is mostly preferred for simple applications.

2.2 Sinusoidal Commutation

Unlike trapezoidal commutation, three of the phases are active at the same time in sinusoidal drive. It results in sinusoidally shaped phase currents. In order to obtain sinusoidally shaped currents, PWM should have higher frequency as compared to trapezoidal commutation [41]. As a result of matching back EMF and current wave-

forms, smoother torque is obtained. It enables more precise motor control as compared to trapezoidal commutation. On the other hand, sinusoidal commutation needs more accurate position information. Therefore, encoder or resolver are preferred because of their high resolution output. This need for advanced position information increases design complexity and cost.

Although sinusoidal commutation has better low speed performance as compared to trapezoidal commutation, it is difficult to handle in high speed because of increased frequency of back EMF. As a consequence of increased back EMF frequency, produced phase currents should also be change with higher frequency. Therefore, PI controllers have difficulty in tracking phase currents. Because of limited frequency response of PI controller, gain error and phase lag in motor currents increase at high speeds. As a result of phase lag, current space vector steer away from ideal quadrature direction. Therefore, smaller torque can be obtained with the same amount of current at high speeds. It means that efficiency will be lower at high speeds.

2.3 Field Oriented Control

Field Oriented Control is preferred in relatively advanced applications because of its computational complexity. Unlike trapezoidal commutation, it can provide high torque even in high speeds. Advantages of FOC can be summarized as transforming complex AC model into simpler linear model, decoupled control of torque and flux, fast dynamic response, high torque/current ratio at start-up, high efficiency and opportunity of expanded speed range [36], [45]. It can be said that FOC combines the advantages sides of both trapezoidal and sinusoidal commutation. It has smoothness of sinusoidal commutation at low speeds; on the other hand, it is also easily applicable at high speeds.

2.4 Choice of Commutation Method for Permanent Magnet Motors

Efficiency of commutation techniques shows difference between PMSM and BLDC. It results from variety in back EMF waveform. When produced rotating field and flux vector are optimally alligned, torque becomes smoother. Therefore, it is argued that BLDC has better performance when it is driven with trapezoidal as compared to

sinusoidal technique. The reverse is applicable for PMSM. It means that PMSM has more desirable torque outcome when it is sinusoidally driven [9].

As previously stated, trapezoidal commutation is superior than sinusoidal commutation in aspect of torque ripple. On the other hand, it is observed that BLDC with sinusoidal commutation has faster settling time than the one with trapezoidally driven. Since BLDC is not purely trapezoidal because of inductive nature of motor. Inductance of motor smooths trapezoidal waveform into somewhat sinusoidal. Therefore, BLDC could be driven sinusoidally if transient response has greater importance than torque ripple [34].

Efficiency comparison between BLDC with trapezoidal driven and BLDC with sinusoidal driven is done in terms of motor and inverter efficiency [15]. It figures out that trapezoidal commutation is more efficient at all speed region for BLDC. While efficiency difference between trapezoidal and sinusoidal drive is small at low speed, it becomes higher at high speeds. It proves that trapezoidal drive has bigger torque ripple at low speed as compared to high speed. Additionally, trapezoidal drive has superiority over sinusoidal drive because of higher inverter efficiency.

In theory, BLDC with trapezoidal commutation is expected to produce constant torque. However, this is not the case since current cannot not rise immediately in motor phase. Therefore, torque ripple happens in every 60 electrical degree [2]. This fact is illustrated in Figure 2.1.

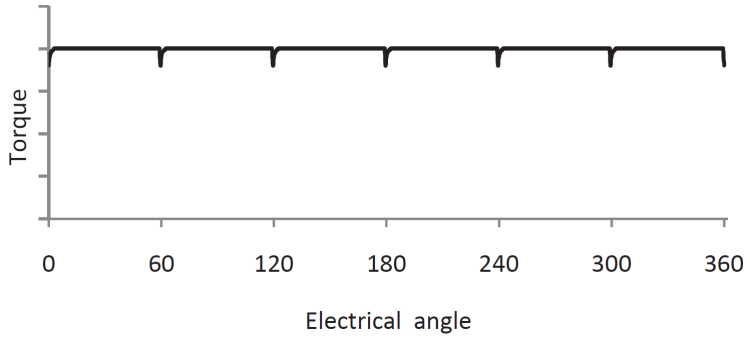

Figure 2.1: Torque Output of Trapezoidal Driven BLDC [37]

In contrast to BLDC example, sinusoidal PWM produces better torque than trapezoidal PWM for the case of PMSM. As can be seen from Figure 2.2, there is considerable amount of torque ripple takes place when PMSM is driven with six step

commutation method. Therefore, sinusoidal or FOC commutation methods should be applied to obtain better torque performance.

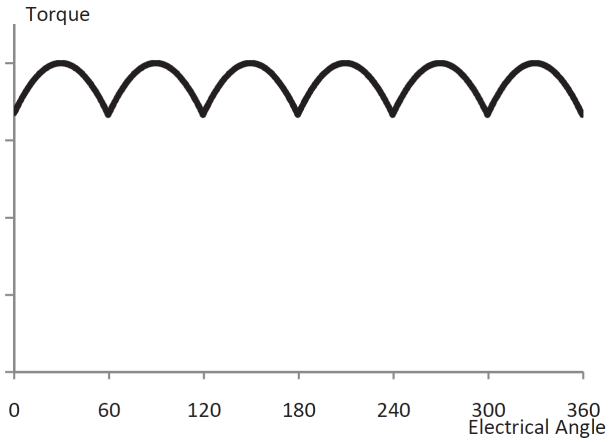

Figure 2.2: Torque Output of Trapezoidal Driven PMSM [37]

However, designers should be aware of the fact that better torque quality comes with a price. First of all, there is a need for more accurate rotor position. Therefore, using only hall effect sensor for commutation is not an option any more. Advanced and precise sensors should be added to the system. Secondly, current controller performance deceases at higher speeds because of increase in current frequency. This deterioration in high speeds results from limitations on frequency and gain response of PI controller. In order to eliminate disadvantages coming from time variant nature of stator phase currents, FOC is recommended for operations with wide speed range requirement [20].

It can be concluded that there is no universal method which is ideal for every kind of permanent magnet motor. Therefore, commutation method should be chosen according to requirements of the system. Important aspects of previously mentioned commutation techniques are summed up in Table 2.1.

Table 2.1: Comparison of Commutation Techniques [25], [38], [37]

	Trapezoidal	**Sinusoidal**	**FOC**
Speed Control	Excellent	Excellent	Excellent
Torque Control at Low Speed	Torque Ripple	Excellent	Excellent
Torque Control at High Speed	Efficient	Inefficient	Efficient
Feedback Device	Hall Sensor	Encoder/Resolver	Current Sensor, Encoder/Resolver
Algorithm Complexity	Low	Medium	High

2.5 PWM Methods for FOC

SPWM, SVPWM and third harmonic injection PWM (THIPWM) methods are proposed for FOC based commutation in [36]. Their models are simulated Simulink environment in order to make performance comparison. As a result of experiments conducted in Simulink, it is measured that THIPWM has the best result in terms of total harmonic distortion (THD). On the other hand, THIPWM is not recommended because of its undesired effect on non-linearity of the system.

Modulation techniques are supposed to reach fundamental output voltage with high amplitude. Additionally, harmonics are intended to be reduced. It is given that SVPWM produced 15% bigger fundamental output voltage with lesser THD as compared with SPWM [22].

2.6 Motivations for FPGA based Design

Similarly, implementation methodology can also be realized on different environments such as pure hardware, combination of hardware-software and pure software. FPGA, DSP, micro-controller can be listed as possible hardware implementation environments [9].

Owing to rapid development in integrated circuit (IC) industry, DSP options with high performance and low cost has been more common for past few decades. Even, dedicated motor controller ICs have been produced. Although the system with dedicated controller IC is advantageous because of simple circuitry and adaptability to various motors, they are generally incapable of meeting the expectations about higher sample rated current control loops [24]. Especially, systems with SVPWM have a very short amount of time for calculation which are necessary for decision about switching pattern. Because of sequential structure of DSP, reaching higher sampling rates in current control loops could be problematic. Therefore, the necessity of DSP with a floating point processor and high frequency could be risen for FOC applications instead of a fixed point DSP. However, this replacement comes with the price.

However, FPGA has been more popular before thanks to progress in VLSI (Very Large Scale Integration) technology. FPGA is superior to DSP in terms of short design cycle, embedded processor option, lower power consumption and higher density [33]. FPGA integrates good sides of application specific integrated circuit (ASIC) and general purpose DSP. Additionally, System on Chip (SoC) alternative for motor control applications is worth to mention. SoC offers designers to integrate power of parallel processing and efficiency of embedded processor IPs. While heavy computations could be done in processor side, control algorithms which need parallel operations could be handled by programmable logic side [23].

CHAPTER 3

THEORY OF OPERATION

3.1 Introduction

As previously mentioned, optimal control strategy for a permanent magnet synchronous motor is determined according to back EMF nature. Therefore, PMSM should be driven with sinusoidal phase currents. It is because of the fact that current references must be in phase with back EMFs for the purpose of reaching maximum torque/current ratio [7].

In the scope of this thesis, field oriented control based on SVPWM is decided to be implemented because of efficiency and torque ripple concerns. This method is based on decomposition of stator current. Thanks to this decomposition, PMSM could be controlled like separately exited DC motor. In order to separate torque and flux generating components of stator current, reference frame transformations are needed. Therefore, domain transformations and mathematical model of PMSM are given first. After then, theory behind the field oriented control is discussed. Finally, space vector PWM, PI and LQR controller design procedures are explained.

3.2 Domain Transformation

Phase currents of the motor depend on rotor position; therefore, complexity of motor equations increases. If reference domain is transferred from stationary to the frame which is rotating with the motor, there will be simplification in complexity of motor equations. This transformation can be done in two steps which are shown in Figure 3.1.

Clarke transformation is used for translation from 3-phase stationary reference frame to 2-phase stationary one. Motor variables, which are referenced to this frame, are still

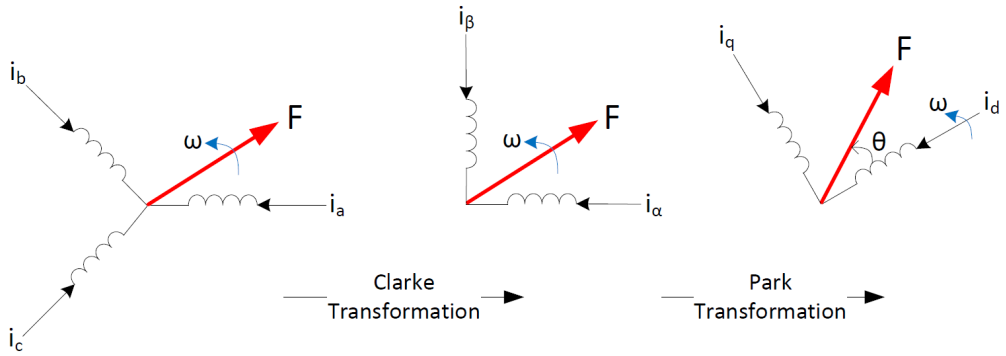

Figure 3.1: Clarke and Park Transformations

position-dependent. Therefore, Park transformation is needed to get rid of position dependency. It enables to transform 2-phase stationary reference frame into 2-phase moving one. Clarke and Park transformations are also named as abc to alpha-beta and alpha-beta to dq (direct-quadrature) transformations respectively.

$$\begin{bmatrix} u_\alpha \\ u_\beta \\ u_0 \end{bmatrix} = \begin{bmatrix} \frac{2}{3} & -\frac{1}{3} & -\frac{1}{3} \\ 0 & \frac{1}{\sqrt{3}} & -\frac{1}{\sqrt{3}} \\ \frac{1}{3} & \frac{1}{3} & \frac{1}{3} \end{bmatrix} \begin{bmatrix} u_a \\ u_b \\ u_c \end{bmatrix} \tag{3.1}$$

$$\begin{bmatrix} u_d \\ u_q \\ u_0 \end{bmatrix} = \begin{bmatrix} \cos(\theta) & \sin(\theta) & 0 \\ -\sin(\theta) & \cos(\theta) & 0 \\ 0 & 0 & 1 \end{bmatrix} \begin{bmatrix} u_\alpha \\ u_\beta \\ u_0 \end{bmatrix} \tag{3.2}$$

By multiplying Matrices 3.1 and 3.2, d-axis aligned abc to dq transformation matrix can be obtained as:

$$\begin{bmatrix} d \\ q \\ 0 \end{bmatrix} = \frac{2}{3} \begin{bmatrix} \cos(\theta) & \cos(\theta - \frac{2\Pi}{3}) & \cos(\theta + \frac{2\Pi}{3}) \\ -\sin(\theta) & -\sin(\theta - \frac{2\Pi}{3}) & -\sin(\theta + \frac{2\Pi}{3}) \\ \frac{1}{2} & \frac{1}{2} & \frac{1}{2} \end{bmatrix} \begin{bmatrix} a \\ b \\ c \end{bmatrix} \tag{3.3}$$

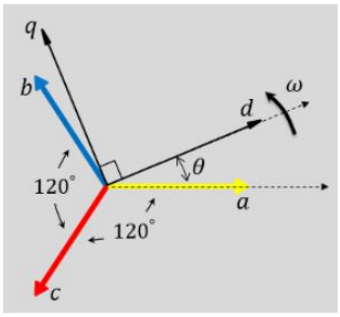

Figure 3.2: abc to dq Transformation [30]

In Figure 3.2, θ is the angle between a and d axes. ω is the rotational speed of the d-q reference frame, where $\theta = \omega t$. It should be noted that all equations in Chapter 3 is based on d-aligned reference frame. In the literature, there is also another set of equations based on q-aligned reference frame. From motor point of view, functionality of abc to dq transform can be visualized with Figure 3.3. It is a fact that the direct axis is aligned with resultant magnetic axis of rotor's magnetic poles. On the other hand, the quadrature axis is placed 90° electrical ahead of the direct axis. Figure 3.3 illustrates two poles condition. As a result of two poles, q-axis is mechanically and electrically 90° ahead of d-axis. However, it is not the case for rotors with higher number of poles. For instance, motor with 6 poles, mechanical angle between d and q axis is 30°. It should be noted that mechanical and electrical angles are not the same thing. Electrical angle (θ_e) is pole pair times of mechanical angle (θ_m). In summary, control strategy does not affected by pole pair number because all motor equations are based on electrical angle [8].

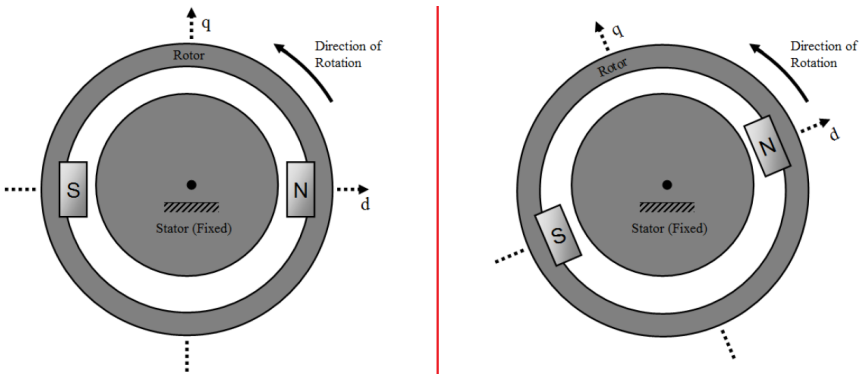

Figure 3.3: Rotating dq Reference Frame [8]

3.3 Mathematical Model of PMSM

When deriving dq frame equations for a balanced star connected PMSM, following assumptions are taken into account [18], [31].

1. Saturations and parameter changes, depending on temperature and frequency, are neglected.
2. Stator windings are balanced.
3. The sinusoidal model assumes that the flux, established by the permanent magnets in the stator, is sinusoidal

4. Eddy currents and hysteresis loses are negligible.

With these assumptions, dq equations in the rotor reference frame are [32]:

$$v_d = R_s i_d + p\lambda_d - Pw_r\lambda_q \tag{3.4}$$

$$v_q = R_s i_q + p\lambda_q + Pw_r\lambda_d \tag{3.5}$$

$$\lambda_q = L_q i_q \tag{3.6}$$

$$\lambda_d = L_d i_d + \lambda_{af} \tag{3.7}$$

$$T_e = 3P\left[\lambda_{af} i_q + \left(L_d - L_q\right) i_d i_q\right]/2 \tag{3.8}$$

In constant flux mode, electrical torque equation is simplified as:

$$T_e = 3P\lambda_{af} i_q/2 = K_t i_q \tag{3.9}$$

$$Power = 3\left(v_d i_d + v_q i_q\right)/2 \tag{3.10}$$

State space representation of these equations are:

$$pi_d = \left(v_d - Ri_d + Pw_r L_q i_q\right)/L_d \tag{3.11}$$

$$pi_q = \left(v_q - Ri_q - Pw_r L_d i_d - Pw_r\lambda_{af}\right)/L_q \tag{3.12}$$

$$pw_r = \left(T_e - Bw_r - T_l\right)/J \tag{3.13}$$

$$p\theta_r = w_r \tag{3.14}$$

3.4 Field Oriented Control

The torque of a synchronous motor depends on the phase difference between the rotating magnetic field and the rotor. The torque will be low when there is a small phase difference between the rotor and the rotating magnetic field. The torque increases as the phase difference increases. Consequently, the torque will be bigger when this phase difference approaches 90 degrees. Therefore, a synchronous motor can produce suitable torque under variable load conditions. The magnitude of the maximum torque is regulated by controlling the peak magnitude of the input current. If the torque is required to be varied independent of the load, vector control can be applied.

The FOC principle is based on separating flux and torque components of stator current. By this way, it is aimed to control PMSM like a separately excited DC machine

wherein the flux producing and torque producing currents are separately controlled [35]. To decouple the torque and flux producing currents, Equations 3.2 and 3.1 are used. These transformations yield i_d, the flux component, and i_q, the torque component. i_q is named as torque component since it is orthogonal to rotor magnetic field and produces the desired torque.

As stated previously, i_d creates rotor flux vector. This vector should be aligned with magnetic poles of rotor in order to produce maximum torque [49]. Maximum torque is achieved in the case of zero i_d current reference. It should also be noted that i_d current could be set to negative values for flux weakening purpose. By setting negative i_d reference value, air gap flux is reduced. As a result of reduced air gap flux, lower back EMF is obtained. Lower back EMF enables the motor achieve higher rated speed [18]. In the scope of thesis, there is no need of increase in maximum operating speed. Therefore, it is decided that the most convenient strategy is to set the flux component (i_d) to zero, which increases the motor efficiency.

Although FOC method eases the control, it requires accurate rotor position to guarantee an improved dynamic response. This can be achieved with a position sensor such as resolver or incremental encoder. For low-cost application, different rotor position observer strategies are applied to eliminate position sensor. In our case, resolver provides position information, in order not to compromise control accuracy.

3.5 Space Vector Pulse Width Modulation

PWM technique is responsible for creating the desired phase voltages for the motor. Duty cycle is determined according to the magnitude of PWM block input signal. PWM decreases average power dissipation as compared to linear power amplifiers. There are different PWM methods for different kind of applications. According to application constraints, the optimum PWM method could differ for each application. However, the main goal of each PWM strategy is achieving and increase in fundamental component while decrease in harmonics and switching loses as much as possible [42].

In the literature, commonly used PWM methods for PMSM can be listed as sinusoidal, third harmonic injection and space vector PWM. SPWM is the earliest ap-

plication among three of them. The utilization rate of the DC voltage is 78.5% of the DC bus voltage, which is considerably low as compared to 100% rate of six-step PWM. The need of higher utilization rate results in development of THIPWM method. THIPWM improves utilization rate from 78.5% to above 90%. THIPWM offers also lower harmonic distortion than SPWM. Afterwards, SVPWM technique is introduced by researchers. It has superior results in aspects of utilization rate and harmonic problems. However, it requires some mathematical manipulations. Therefore, SVPWM method is widely used in DSP and FPGA based servo controller applications [42].

It is convenient to say that SVPWM is an advanced version of SPWM. Thanks to the domain transformations, stator currents could be expressed in a time-invariant way. Therefore, speed variant nature of currents is eliminated. From current controller point of view, feedback currents transform into DC values. Consequently, bandwidth of the system improves in return for increase in processing requirements [37].

Space Vector PWM was developed as sinusoidal three-phase voltage source to realize DC to AC power conversion. Based on a electrical position region, two neighbouring space vectors are chosen out of six vectors. The on-time of each phase is calculated based on magnitude of input vector. Switching instants of MOSFETs can be differ according to chosen switching scheme. There are two zero state vectors on circular locus. They are used for completing remaining time of one switching period. It is noted that sampling time is constant. Two main steps for SVPWM are explained in the following sections.

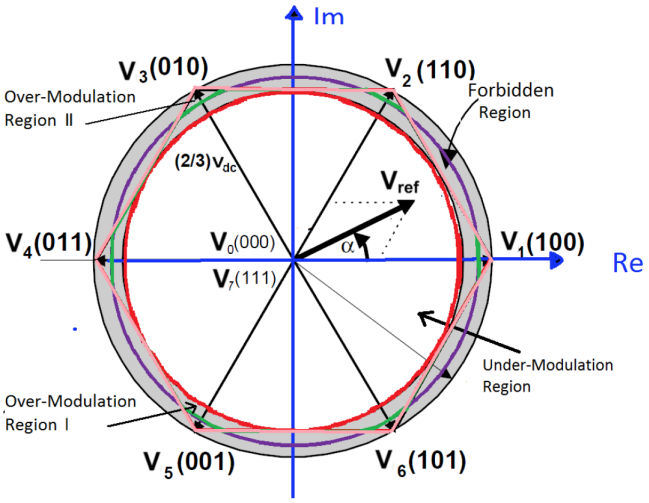

Figure 3.4: Space Vector Representation [42]

3.5.1 Determination of V_{ref} and θ

Output vectors of d and q PI controllers are transferred to alpha-beta domain by using inverse park matrix, which is inverse of Eq. 3.2. V_{ref} is found by taking square root of alpha and beta vectors. Since alpha-beta domain is dependent of electrical position, arctangent of the summation gives electrical position command of next current controller cycle.

$$|V_{ref}| = \sqrt{V_\alpha^2 + V_\beta^2} \tag{3.15}$$

$$\theta = \tan^{-1}\left(\frac{V_\alpha}{V_\beta}\right) \tag{3.16}$$

3.5.2 Switching Time Duration T_a, T_b and T_0

Assuming T_{sample} is sufficiently small so that V_{ref} is constant during that time, switching time durations can be found with Eq. 3.17. V_a, V_b are adjacent active vectors and V_0, V_7 are null vectors. Each switching period starts and ends with one of the null vectors.

$$\begin{aligned} \vec{V_{ref}} T_{switch} &= \vec{V_a} T_a + \vec{V_b} T_b + \vec{V_{0,7}} T_0 \\ T_{switch} &= T_a + T_b + T_0 \\ T_{sample} &= 2T_{switch} \end{aligned} \tag{3.17}$$

After calculating the position by using Eq. 3.16, active sector is found. According to the sector, active space vectors are determined. Then, V_{ref} is projected to these vectors. For Sector-1, this projection results Eq. 3.18.

$$\begin{aligned} Re : V_{ref}\cos(\theta)T_{switch} &= \frac{2}{3}V_{dc}T_a + \frac{1}{3}V_{dc}T_b \\ Im : V_{ref}\sin(\theta)T_{switch} &= \frac{1}{\sqrt{3}}V_{dc}T_b \end{aligned} \tag{3.18}$$

Similar to the above equation, generalized formula for switching time duration can be given as the following equation.

$$\begin{aligned} T_a &= \frac{\sqrt{3}T_{switch}V_{ref}}{V_{dc}}\left(\sin\left(\frac{sector}{3}\pi - \theta\right)\right) \\ T_b &= \frac{\sqrt{3}T_{switch}V_{ref}}{V_{dc}}\left(\sin\left(\theta - \frac{sector-1}{3}\pi\right)\right) \\ T_0 &= T_{switch} - T_a - T_b \end{aligned} \tag{3.19}$$

3.5.3 Space Vector Modulation Scheme

In the literature, there are a number of switching schemes for SVPWM. Basic distinction between them is being symmetrical or asymmetrical. According to designer's choice among power consumption, total harmonic distortion coefficient etc., one of schemes is chosen. Symmetric scheme, equal sharing of null vector, is often chosen since it provides moderate compromise between simplicity and THD [14], [42]. In the scope this thesis, the scheme, given in Figure 3.5, is taken into account. In

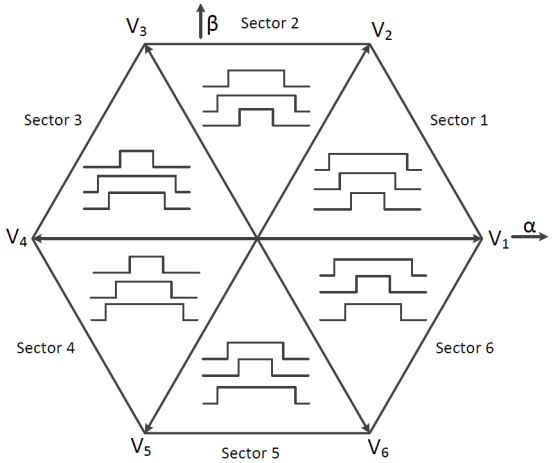

Figure 3.5: Switching Patterns for Six Sectors in Circle [42]

theory, upper and lower MOSFETs of the same phase should change state simulta-

neously in order to create perfect sinusoidal phase currents. On the other hand, it is not applicable in reality because of finite turn-on and turn-off time of MOSFETs. Therefore, there should be certain amount of delay between opening of one MOSFET and closure of other complementary MOSFET, which is in the same line, to prevent short circuit on input line. Delay time can be calculated according to MOSFET's timing characteristics. In our case, IRF7580 N-Channel Power MOSFETs are used. Its dynamic characteristics are given in Table 3.1.

Table 3.1: Timing Characteristics of IRF7580

Symbol	**Parameter**	**Typical**
$t_{d(on)}$	Turn-On Delay Time	20 ns
t_r	Rise Time	38 ns
$t_{d(off)}$	Turn-Off Delay Time	53 ns
t_f	Fall Time	21 ns

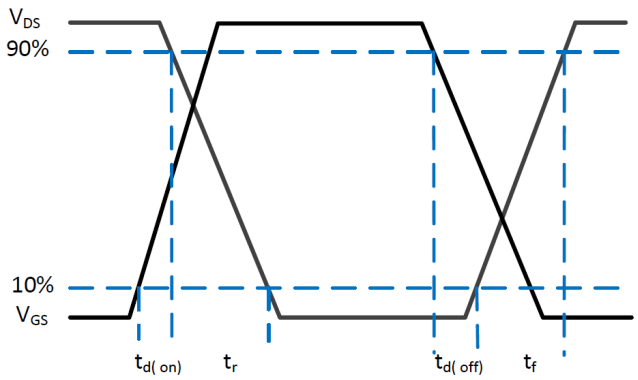

Figure 3.6: Switching Time Waveforms of IRF7580 [17]

According to timing parameters given in Table 3.1, there should be at least 132 ns between switching of upper and lower MOSFETs. It is also be noted that this parameters are measured at ambient temperature. In order to stay in safe side, delay time is extended to 200 ns in this thesis for the purpose of taking different operating conditions into consideration.

3.6 PI Controller Design

Current control loops are necessary to control stator flux position for vector control of synchronous machines. They are responsible for minimization of undesired effects resulting from voltage source inverter and motor non-linearities. If there were no

variations during operation, torque reference command would be enough for desired axis replacement. However, this is not the case because of several reasons. These reasons can be listed as load torque disturbance, error of current control loop and torque constant variation [19].

Since back EMF frequency proportionally increases with rotor speed, current loop's bandwidth should be chosen according to maximum desired speed. Current loops cut off frequency should be higher than current frequency in order to produce desired torque efficiently. If bandwidth of loops is not high enough, current values start to lag references. Additionally, amplitudes of feedback currents decrease [7].

In Figure 3.7, overall block diagram of current controller is given. Firstly, phase currents and rotor position are read by current sensor and resolver respectively. These sensors produce analog output; therefore, they need to be digitized first in order to make calculations in digital domain. Digitalization is realized by ADCs which are configured by programmable logic. Secondly, phase currents and rotor electrical position are used for domain transformation. 'abc to dq' transformation block represents forward domain transformation. As a result of this transformation, phase currents are now in rotating domain and position constant-free. Thirdly, direct and quadrature currents are fed into PI (Proportional-Integral) controller block. Fourthly, outputs of PI blocks are transformed reversely to 2-phase stationary domain. Finally, gate switching scheme is determined according to the chosen SVPWM strategy. In the previous part of the chapter, these blocks are explained in a detailed way.

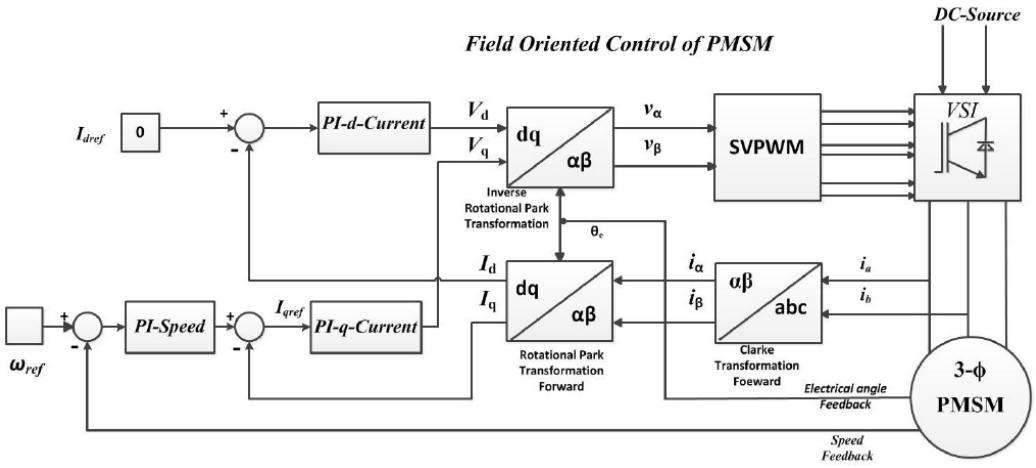

Figure 3.7: Block Diagram of Field Oriented Control [3]

3.6.1 PI Controller Design Procedure

Design procedure should be started from inner loop since its transfer function affects the outer loop directly. By making assumptions on Equations 3.4, 3.5 and 3.8, transfer functions having outputs of i_d, i_q and w_r are found respectively. Transfer functions are created with the following motor constants: $R_s = 1.1, L_d = L_d = 3.25e{-}04, J = 6.36e-05, B = 4.53592e-05, P = 16$.

3.6.1.1 PI Controller Loop i_d

Assuming $w_r = 0$ and ignoring Pw_ri_q term, transfer function for i_d current loop can be written as in Equation 3.20. Pw_ri_q term is neglected because of two main reasons. Firstly, the term is relatively small as compared to $\frac{v_d}{L_d}$ term. Secondly, w_r is generally near to zero for our operational region.

$$G_d = \frac{i_d}{v_d} = \frac{1}{sL_d + R} \tag{3.20}$$

According to $1e^{-3}s$ settling time requirement, gain crossover frequency is determined as $6000rad/s$. By using pid optimization function, PI parameters are found as $K_p = 1, K_i = 1.1e4$. Bode diagram and step response of closed loop system are given in Figures 3.8 and 3.9 respectively.

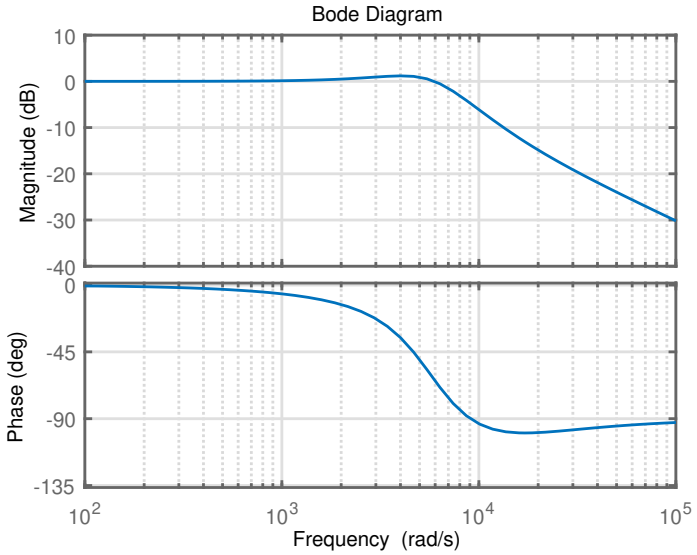

Figure 3.8: Bode Diagram of i_d Closed Loop

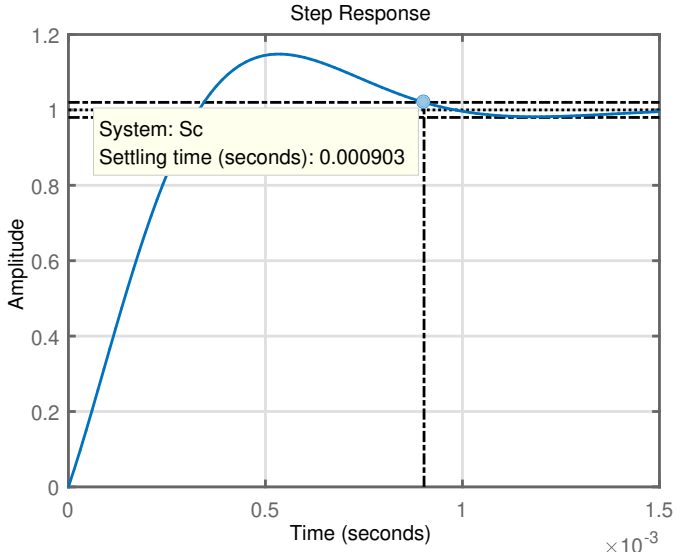

Figure 3.9: Step Response of i_d Closed Loop

3.6.1.2 PI Controller Loop for i_q

Assuming $i_d = 0$, transfer function for i_q current loop can be written as;

$$G_q = \frac{i_q}{v_q} = \frac{sJ + B}{s^2\left(L_q J\right) + s\left(JR + BL_q\right) + \left(BR + 1.5\lambda_{af}^2 P^2\right)} \tag{3.21}$$

According to $1e^{-3}s$ settling time requirement, gain crossover frequency is determined as $6000rad/s$. By using pid optimization function, PI parameters are found as $K_p = 3, K_i = 2.4e4$. Bode diagram and step response of closed loop system are given in Figures 3.10 and 3.11 respectively.

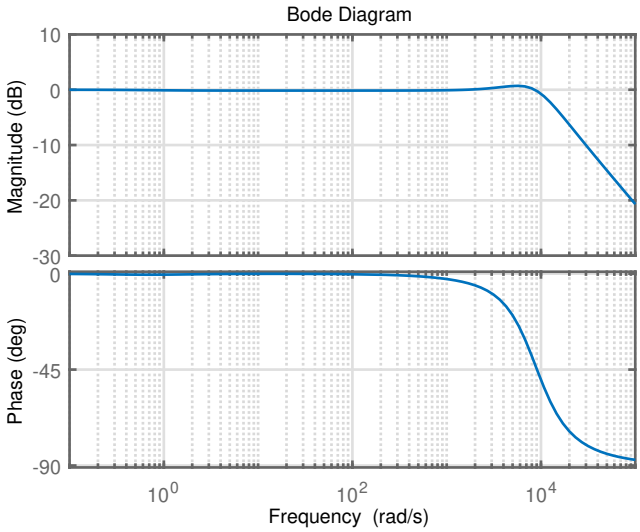

Figure 3.10: Bode Diagram of i_q Closed Loop

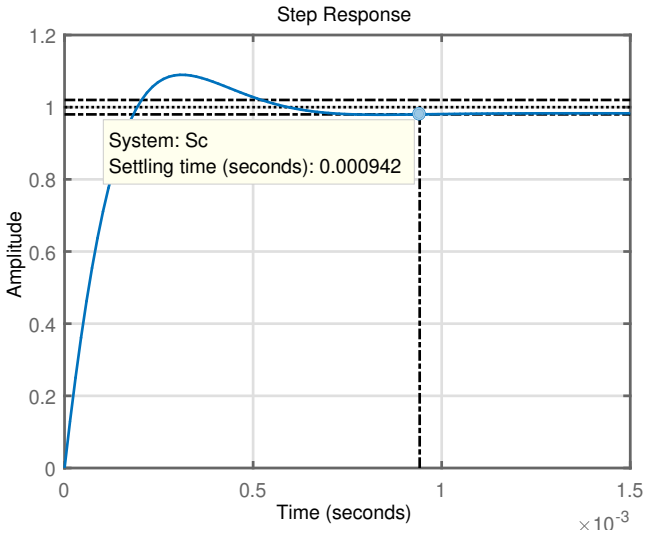

Figure 3.11: Step Response of i_q Closed Loop

3.6.1.3 PI Controller Loop w_r

Since round PMSM is used, it is known that $L_d = L_q$. Assuming $i_d = 0$, transfer function for w_r controller loop can be written as;

$$G_w = \frac{w_r}{i_q} = \frac{1.5P\lambda_{af}}{sJ + B} \tag{3.22}$$

According to $1e^{-2}s$ settling time requirement, gain crossover frequency is determined as $600rad/s$. By using pid optimization function, PI parameters are found as $K_p =$

$1, K_i = 50$. Bode diagram and step response of closed loop system are given in Figures 3.12 and 3.13 respectively.

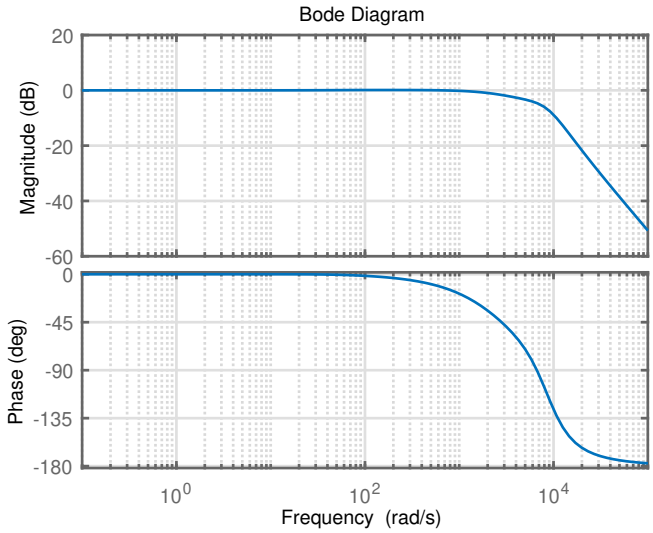

Figure 3.12: Bode Diagram of w_r Closed Loop

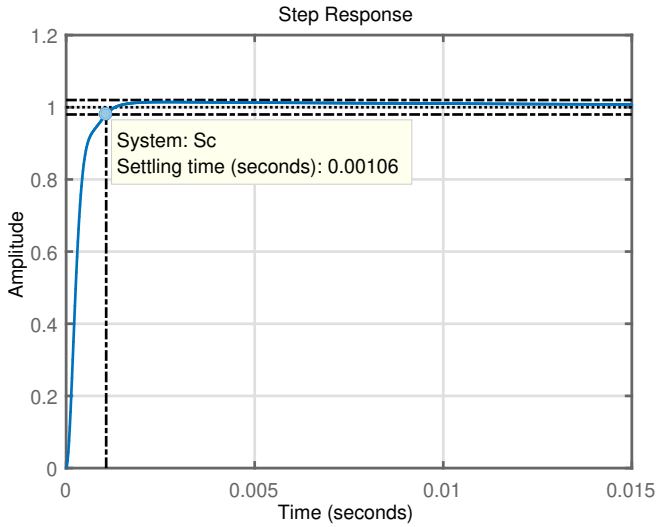

Figure 3.13: Step Response of w_r Closed Loop

3.7 State Feedback Controller Design

Three states are chosen as i_d, i_q and ω. Around the nominal steady state point, derivatives of the states approach to zero. Therefore, Equations 3.23, 3.24 and 3.25 can be expressed in a new form given in 3.27.

$$\frac{d}{dt}i_d = -\frac{R}{L_d}i_d + \frac{L_q}{L_d}P\omega i_q + \frac{1}{L_d}u_d \tag{3.23}$$

$$\frac{d}{dt}i_q = -\frac{R}{L_q}i_q - \frac{L_d}{L_q}P\omega i_d - \frac{P\omega\lambda_{af}}{L_q} + \frac{1}{L_q}u_q \tag{3.24}$$

$$\frac{d}{dt}\omega = \frac{3}{2}\frac{P}{J}\left(\lambda_{af}i_q + (L_d - L_q)\, i_d i_q\right) - \frac{B}{J}\omega - \frac{1}{J}T_l \tag{3.25}$$

$$0 = f\left(x_n, u_n, T_l\right) \tag{3.26}$$

$$y_n = Cx_n \tag{3.27}$$

Linearisation around current operating region should be done in order to transfer nonlinear state equations into linear form. Two methodologies can be accepted through linearisation process. The first one is based on an assumption of limited operating region. Linearisation is made at the beginning of the process. On the other hand, the second approach has capability of working in wider operating regions since linearisation is repeated during operation. Therefore, state feedback matrices could be updated according to new conditions. Although, the second method offers the capability of adaptation to wide range of operations, it results in longer calculation process. At the scope of the thesis, the first approach is adopted since our operating range is narrow at that sense. Linearisation on the state equations is done at the point of $i_{dn} = 0$, $i_{qn} = 0.5$ and $\omega_n = 0$. Consequently, A, B and C matrices can be rewritten as in Equations 3.28, 3.29 and 3.30.

$$\begin{bmatrix} -\frac{R}{L_d} & \frac{L_q P\omega_n}{L_d} & \frac{L_q P i_n}{L_d} \\ -\frac{L_d P\omega_n}{L_q} & -\frac{R}{L_q} & -\left(\frac{L_d P i_{dn}}{L_q}\right) - \left(\frac{P\lambda_{af}}{L_q}\right) \\ \frac{3P(L_d - L_q)i_{qn}}{2J} & \frac{3P}{2J}\left(\left(L_d - L_q\right) i_{dn} + \lambda_{af}\right) & \frac{-B}{J} \end{bmatrix} \tag{3.28}$$

$$\begin{bmatrix} \frac{1}{L_d} & 0 \\ 0 & \frac{1}{L_q} \\ 0 & 0 \end{bmatrix} \tag{3.29}$$

$$\begin{bmatrix} 1 & 0 & 0 \\ 0 & 0 & 1 \end{bmatrix} \tag{3.30}$$

In addition to three states, another two states can be added in order to minimize the steady state errors of previously defined i_d and ω states. The augmented state vector can be defined with Equation 3.31. Consequently, new set of state equations can be defined as in Equation 3.33. Control block is given in Figure 3.14. Control state vector is defined as in Equation 3.32.

$$x_i = C \int (x_{ref} - x(t))\, dt \tag{3.31}$$

$$u(t) = -F_1 x(t) - F_2 x_i(t) \tag{3.32}$$

$$\begin{bmatrix} \dot{x}(t) \\ \dot{x_i}(t) \end{bmatrix} = \begin{bmatrix} A & 0 \\ -C & 0 \end{bmatrix} \begin{bmatrix} x(t) \\ x_i(t) \end{bmatrix} + \begin{bmatrix} B & 0 \\ 0 & C \end{bmatrix} \begin{bmatrix} u(t) \\ x_{ref} \end{bmatrix} + \begin{bmatrix} G \\ 0 \end{bmatrix} T_l \tag{3.33}$$

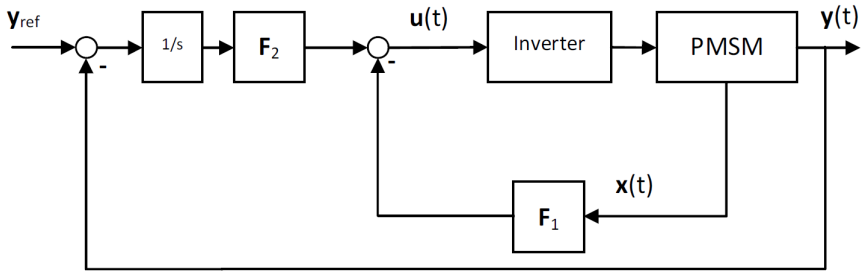

Figure 3.14: Block Diagram of LQR Controller [8]

The weight matrices Q and R are chosen in order to minimize the cost function which is given in Equation 3.1. In article [13], it is said that weights of these matrices have an effect on not only transient but also steady state behaviour. Therefore, it is advised to choose them carefully. As can be seen in Equation 3.34, both state vector $x(t)$ and control input $u(t)$ are weighted in J. It means that $x(t)$ and $u(t)$ cannot be too large if J function is minimized according to optimal state feedback law. The minimized J function implies that $u(t)$ is finite and $x(t)$ approaches to zero [28]. These terms are

enough to guarantee stability of the closed loop system.

$$J = \frac{1}{2}\int_0^\infty \left(x^T Q x + u^T R u\right) dt \tag{3.34}$$

There is no universally optimal weight matrix pair for every system. Q and R matrices are determined by taking design constraints into consideration. If fast transient response and smaller state values of $x\,(t)$ are needed, larger Q matrix should be chosen. On the other hand, larger R matrix results in slower transient response and less control effort [28], [47]. By paying attention to these design rules, our weight matrices are constructed according to Equations 3.35 and 3.36. Chosen weight for each matrices are $q_1 = 0.0025$, $q_2 = 0.0025$, $q_3 = 0.0001$, $q_4 = 10$ and $q_5 = 10$; $r_1 = 0.0025$, $r_2 = 0.0025$, $r_3 = 0.002$, $r_4 = 0.002$ and $r_5 = 0.001$ respectively.

$$\begin{bmatrix} q_1 & 0 & 0 & 0 & 0 \\ 0 & q_2 & 0 & 0 & 0 \\ 0 & 0 & q_3 & 0 & 0 \\ 0 & 0 & 0 & q_4 & 0 \\ 0 & 0 & 0 & 0 & q_5 \end{bmatrix} \tag{3.35}$$

$$\begin{bmatrix} r_1 & 0 & 0 & 0 & 0 \\ 0 & r_2 & 0 & 0 & 0 \\ 0 & 0 & r_3 & 0 & 0 \\ 0 & 0 & 0 & r_4 & 0 \\ 0 & 0 & 0 & 0 & r_5 \end{bmatrix} \tag{3.36}$$

CHAPTER 4

HARDWARE DESCRIPTION

4.1 Introduction

A system on chip (SoC) integrated circuit is used as a controller unit. The used SoC is a member of Xilinx Zynq-7000 family. It integrates Arm-based processor with 28 nm programmable logic. As mentioned in the previous sections, aim of the thesis is design and implementation of vector control for PMSM on FPGA. Experiments are conducted on electronic board which was designed in TÜBİTAK SAGE. In Figure 4.1, block diagram of electronic board and outer parts are given.

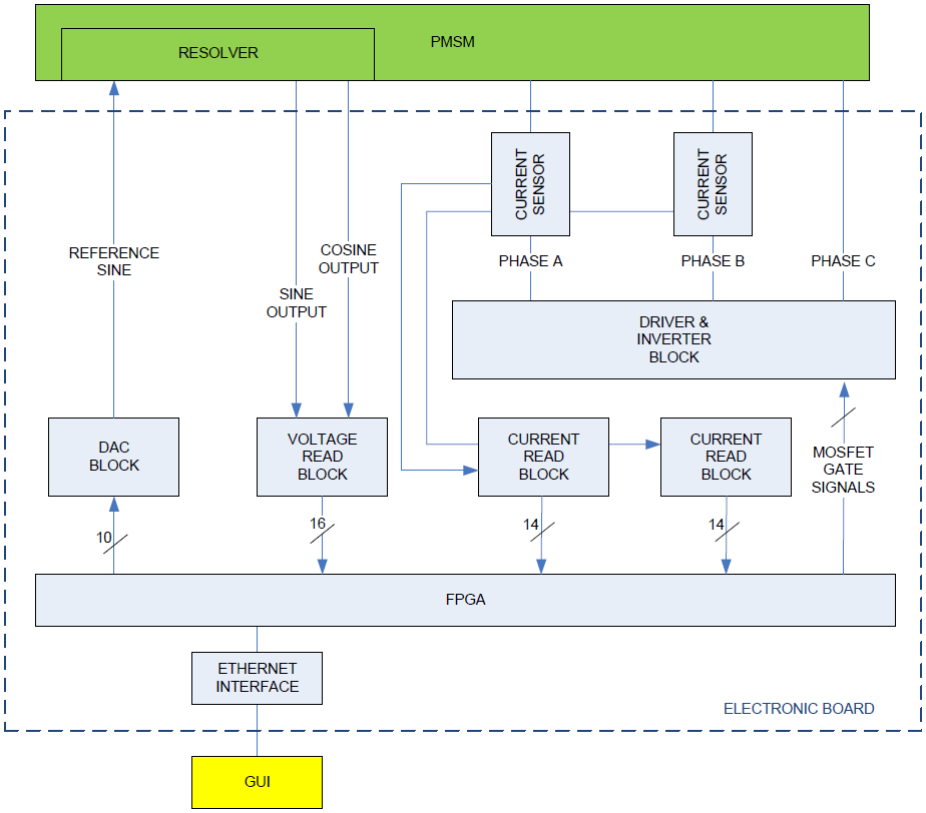

Figure 4.1: Block Diagram of Control System

4.2 Electronic Board

This electronic board mainly consists of components of controller unit and motor driver circuitry. This design is advantageous in terms of compactness as compared to industrial alternatives. Industrial alternatives could be separated into two modules such as driver module and controller module. Generally, driver board is sold with software program to control. Integrating driver and controller functionality in a single board is one of the achievements of the design.

4.2.1 Control Unit

In addition to reduction in number of boards, there is also reduction in total number of components due to use of a SoC. Since PMSM does not have brushes for commutation, PWM module is needed to handle commutation. As a result of PWM module presence, controller unit should also added to the system to regulate current and to handle commutation. In our case, controller source is run on a Xilinx ZYNQ-7000 chip which integrates Arm-based processor with 28 nm programmable logic. Current controller is implemented on the programmable logic side.

In the literature, microcontollers are frequently used in motor driver boards. Some of them are application specific, some are not. Generally, they have limited source; therefore, they are capable of driving certain number of motor at the same time. Because of their limitation on chip size, abilities of monitoring and communication are weaker as compared to FPGAs. FPGAs offer large number of IO pins which enable multiple motor control with single printed circuit board.

Zynq-7000 family offers programmable logic and processing system abilities in a single device. This device also includes on-chip memory, external memory interfaces, and a rich set of IO peripherals. In addition to hardware capabilities, Xilinx shortens the design cycle by producing a large number of soft IP modules.

Control Unit of electronic board also includes Flash, RAM, clock oscillator and Ethernet physical integrated circuits. Quad SPI Flash is a non-volatile memory and stores processor's and programmable logic's configuration data. DDR3 RAM is used as an

external memory for the processor. Processor's instructions set and data are held in RAM.

Last but not least, processing system side of SoC is responsible for connecting VHDL modules and configuration. Additionally, processor is also used for monitoring purposes. Sensed and calculated data are sent to processor. Then, this data is processed and transmitted to PC via ethernet protocol.

4.2.2 Motor Driver Circuitry

In addition to digital electronic circuitry, power electronic components such as inverter blocks are placed on the PCB. As can be seen in Figure 4.2, three-line voltage source inverter topology is used in board. 6 N-Channel power MOSFETs are used for each three-phase inverter circuit. Supply voltage is determined as 28 V_{dc} since this is a recommended bus voltage of the motor. FAN7391 high&low side gate driver IC is placed to control on-off states of MOSFETs.

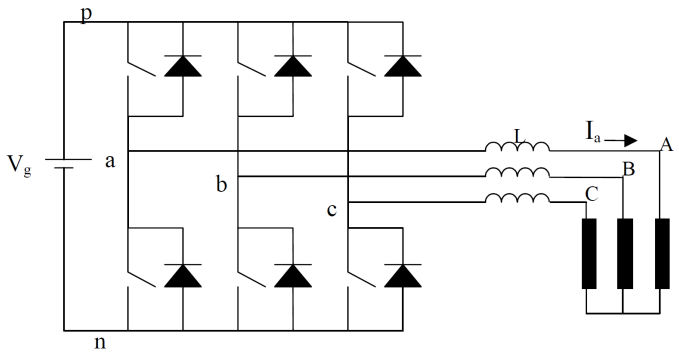

Figure 4.2: Voltage Source Inverter Topology

4.2.3 Current Sensing Block

The electronic board is designed to sense only phase a and phase b currents. There is no dedicated current sensor for phase c. This choice is made to save space on the board. The third one is deduced from summation of the other two. Current sensing block has two main components which are current transducer and analog-to-digital converter.

Current sensor works based on hall effect principle. The conductor that carries sensed current creates magnetic field. This field can be measured in air gap with the help of hall element. The hall element converts measures flux into voltage. Current sensor is capable of measuring currents between -20 and +20 A_{peak} [26]. These limit values are more than enough for our application since peak current limit of the motor is 7.35 A.

In order to convert voltage outputs of current transducers, AD7944 successive approximation analog-to-digital converters are used in system [4]. Output voltage range, sensitivity of current sensor, PWM switching frequency and current sampling rate specifications play critical role in ADC selection.

4.2.4 Position Sensing Block

It should be noted that position information is required to realize space vector PWM method. Sensing rotor position in an accurate way is important since torque control performance is dependent to this accuracy. In the design, resolver is used as a position sensor. Resolver working principle is like an electrical transformer. It has primary winding which is energized by an AC voltage. This primary winding is attached to the rotor. There are also secondary windings which are placed mechanically 90° apart from each other. As the rotor moves, induced sinusoidal voltages on secondary windings change. Induced voltages on secondary windings depend on mechanical position of rotor. From relation between these voltages, absolute position information is obtained.

Figure 4.1 shows block scheme of position sensor reading block. As can be seen from the scheme, there is a digital-to-analog converter to produce reference signal for primary winding. According to the digital input signals of the DAC which are produced by programmable side of SoC, DAC produces analog sinusoidal reference signal. Then, analog outputs of resolver are transformed to digital signals by ADC. These digital signals are interpreted in SoC hence position information is also used in current controller module.

4.3 Focused PMSM

In the scope of thesis, controller is designed for PMSM which is also known as *Brushless DC Motor with Sinusodail BEMF*. Kollmorgen BM series motor is used for experimental work [21]. Motor is wye connected and bus voltage is 28 Volts. Other motor parameters could be found in Table **??**.

Table 4.1: BM-2706 Parameters

Symbol	**Parameter**	**Value**	**Unit**
I_p	Peak current limit	7.35	A
I_{con}	Current at peak continuous stall torque	4.55	A
K_m	Motor constant	0.135	$N.m/sqrt(W)$
K_t	Rated torque sensitivity	0.2	$N.m/A$
K_b	Rated BEMF constant	0.2	$V/rad/s$
R_m	Terminal resistance	2.2	$Ohms$
L_m	Terminal inductance	0.65	mH
J_m	Inertia of the rotor	6.36e-05	$Kg.m^2$
F_i	Viscous damping	4.75e-06	$N.m/RPM$
pp	Number of pole pairs	16	

CHAPTER 5

SIMULINK MODEL

5.1 Introduction

It is beneficial to make simulations of complex systems before attempting to start design procedure. The control system can be examined and easily changed by this way. Moreover, consequences of the chosen algorithms could be observed before experimental tests.

Simulink environment offers plenty of advantages. Firstly, it is helpful in terms of visualization of the system. Creating specific group of blocks for different tasks increases readability. Secondly, it is easy to observe results of small alterations through simulations. In Simulink, it is easy to make trial and error; therefore, design cycle duration could be shortened. Thirdly, it has libraries offering basic ready-to-use blocks which are frequently needed by designers. These libraries shorten design endeavour of simulated model.

In this chapter, it is aimed to create a model of the system, on which experiments are conducted. Sub-modules will be explained individually through the chapter. Additionally, PI and LQR controller blocks are created. Finally, performance analysis of these two controller is made.

5.2 Permanent Magnet Synchronous Motor Block

PMSM block is created according to the previously given Equations 3.4, 3.5, 3.6, 3.7 and 3.8. Figure 5.1 shows inside of PMSM block.

As previously mentioned, Simulink offers some ready-to-use modules. *Permanent Magnet Synchronous Machine*, belonging to Simulink Simscape Electrical library, is

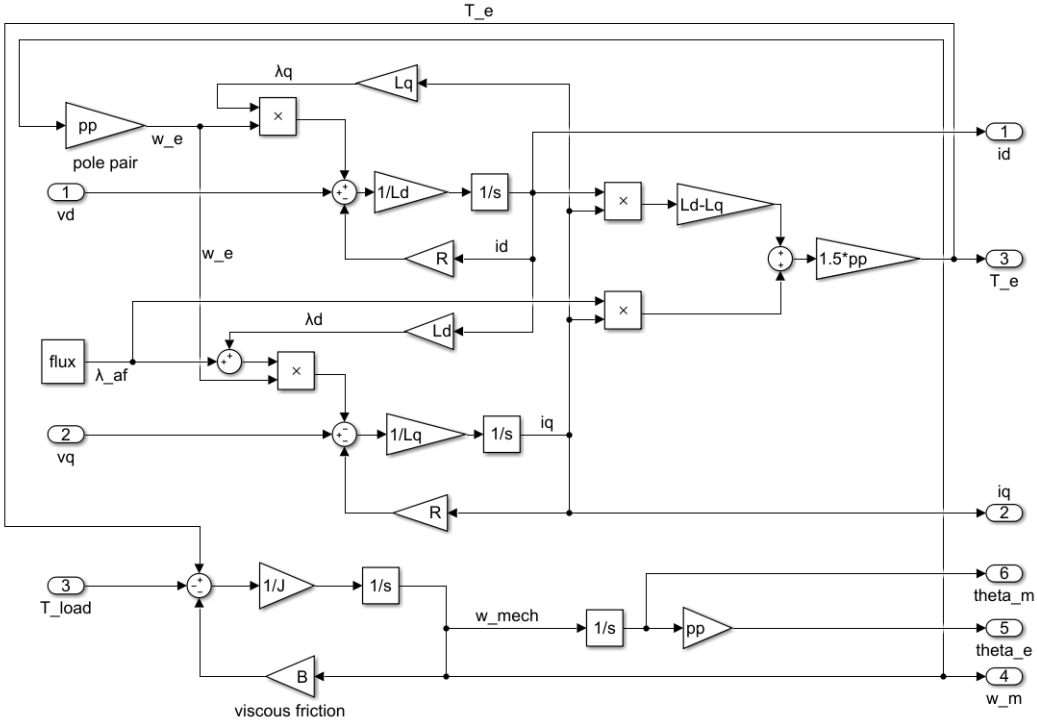

Figure 5.1: Permanent Magnet Synchronous Machine Motor Block

Table 5.1: Motor Parameters for Rotor Reference Frame Model

Parameter	**Value**	**Unit**
R	1.1	Ω
L_q	0.000325	H
L_d	0.000325	H
J	6.3554e-05	$Kg.m^2$
B	4.53592e-05	$N.m/RPM$
pp	16	

one of them. In the scope of the thesis, this module is used in order to validate my custom PMSM block given in Figure 5.1.

Permanent Magnet Synchronous Machine block parameters can be specified by using "Compute from standard manufacturer specifications" option under *Advanced Tab*. By means of configuration window shown in Figure 5.3, it is possible to automatically convert motor specifications from one unit to the other. According to parameters of the interested PMSM, module is manually configured. It eases to make small alterations on model. The designer has opportunity to use the block in different models without consuming much effort. Our motor parameters are entered as shown in Fig-

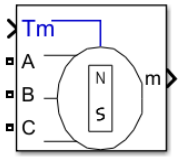

Figure 5.2: PMS Machine Block Symbol

ure 5.3 according to the previously given specifications in Table 4.1. Comparison between custom and ready-to-use PMSM modules shows that my custom model's outputs are very close to outputs of the ready-to-use module.

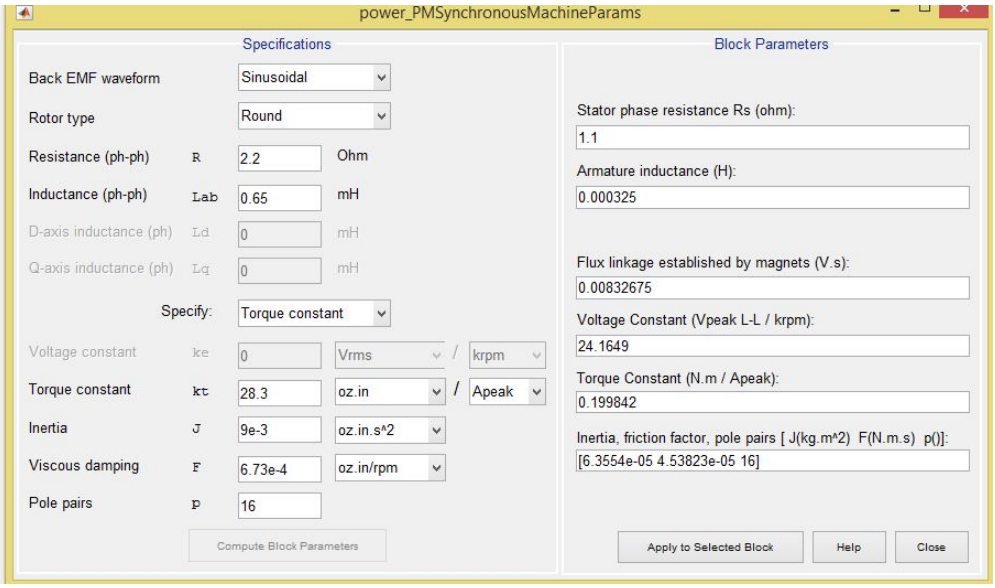

Figure 5.3: Configuration of Permanent Magnet Synchronous Machine

5.3 Park Transformation

As mentioned in *Theory of Operation* chapter, motor phase currents should be transferred into rotor frame by means of Equation 3.3. Figure 5.4 shows inside of the park transformation block.

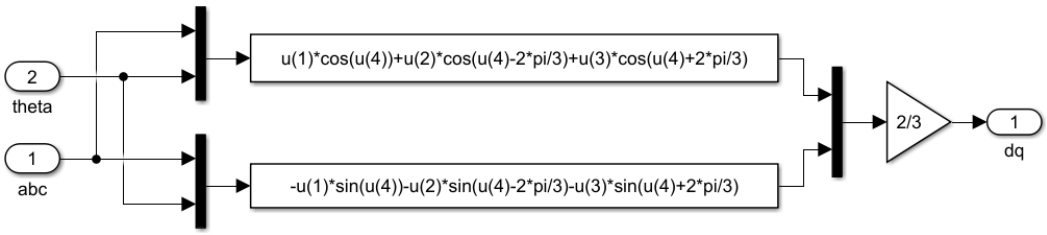

Figure 5.4: Park Transformation Block

5.4 dq to alpha-beta Transformation

Magnitude and angle of the space vector are calculated according to resultant vector in stationary domain. Therefore, dq outputs of current controller are transferred into $\alpha\beta$ domain by using inverse of Park transformation. Transformation matrix is given in Equation 3.2. As can be seen in Figure 5.5, rotor electrical position is needed for transformation. Therefore, the same position information, which is used for Park transformation, is also used for transformation in inverse direction. Position information is held in a register during one period of the current controller.

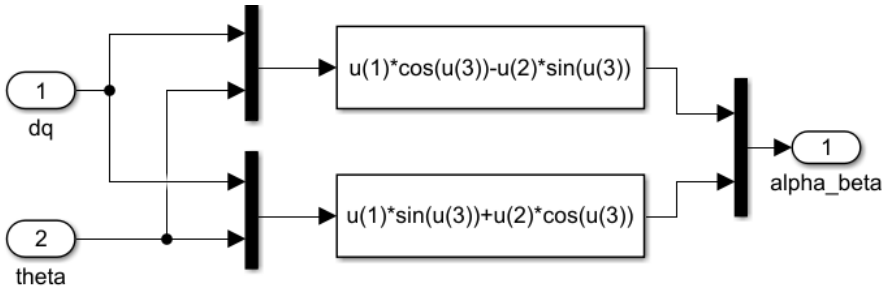

Figure 5.5: dq to $\alpha\beta$ transformation

5.5 Reference Vector Calculation

Reference voltage vector is composed of α and β components. From these components, magnitude and phase angle of a resultant vector are calculated. While magnitude affects duration of MOSFETs open time, phase angle determines active base vectors. In Figure 5.12, *Reference Vector Calculation* block does the mentioned tasks. Inside of the block is shown in Figure 5.6. Outputs of *dq to alpha-beta Transformation* block are fed into *Reference Vector Calculation*. The input vector is composed of real and imaginary components. Magnitude and phase angles are obtained as a result of trigonometric calculations.

As previously mentioned, active vectors could be imagined as diagonals of hexagon. In Figure 3.4, inscribed circle is defined as an under-modulation region. T_0 is reduced to zero at the edge of inscribed circle. After this region, T_0 has negative value. Therefore, different strategies should be applied to reach desired power utilization. These strategies are named as over-modulation techniques in the literature. However, in the

scope of thesis only linear under-modulation region is taken into account. For higher V_{ref} values, reference voltage is set to the saturation value which is determined according to the given formula in Equation 5.1 [42]. If V_{ref} is calculated bigger than V_{limit}, it means that desired reference vector is in over-modulation region. Therefore, V_{ref} should be lower than 16.16 V in order not to exceed under-modulation boundary. For the purpose of creating margin of safety, V_{limit} is set to 16 V [27].

$$V_{limit} = \frac{2}{3} V_{dc} \cos(\pi/6) \tag{5.1}$$

The overall SVPWM block diagram is shown in Figure 5.8. Multiplexer is used to activate valid equation set for current sector.

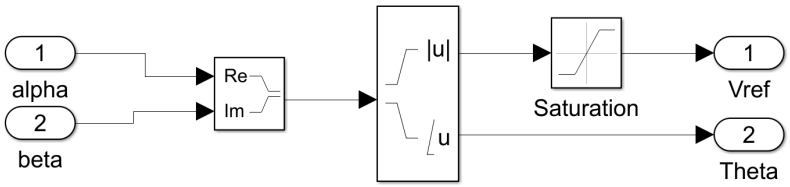

Figure 5.6: Reference Voltage Vector Calculation

5.6 Space Vector PWM

This block is responsible for management of switching scheme. Firstly, theta output of previous block is transferred into degrees from radians. Then, sector is calculated according to look-up table. In every 60 degrees, sector changes. Therefore, comparators are used to detect the current region. Basic elements, used inside of the module, are listed as gain, comparator, logical AND, summation and saturation. Structure of the *Space Vector PWM* block can be seen in Figure 5.7. Secondly, switching durations are calculated based on Equation 3.19. According to calculated durations, PWM switches should be opened in the defined order given in Figure 3.5. s1, s3 and s5 outputs are connected to gates of upper side MOSFETs, given in Figure 4.2.

$$MI = \frac{V_{ref}}{V_{fundamental-sixstep}} V_{fundamental-sixstep} = \frac{2V_{dc}}{\Pi} \tag{5.2}$$

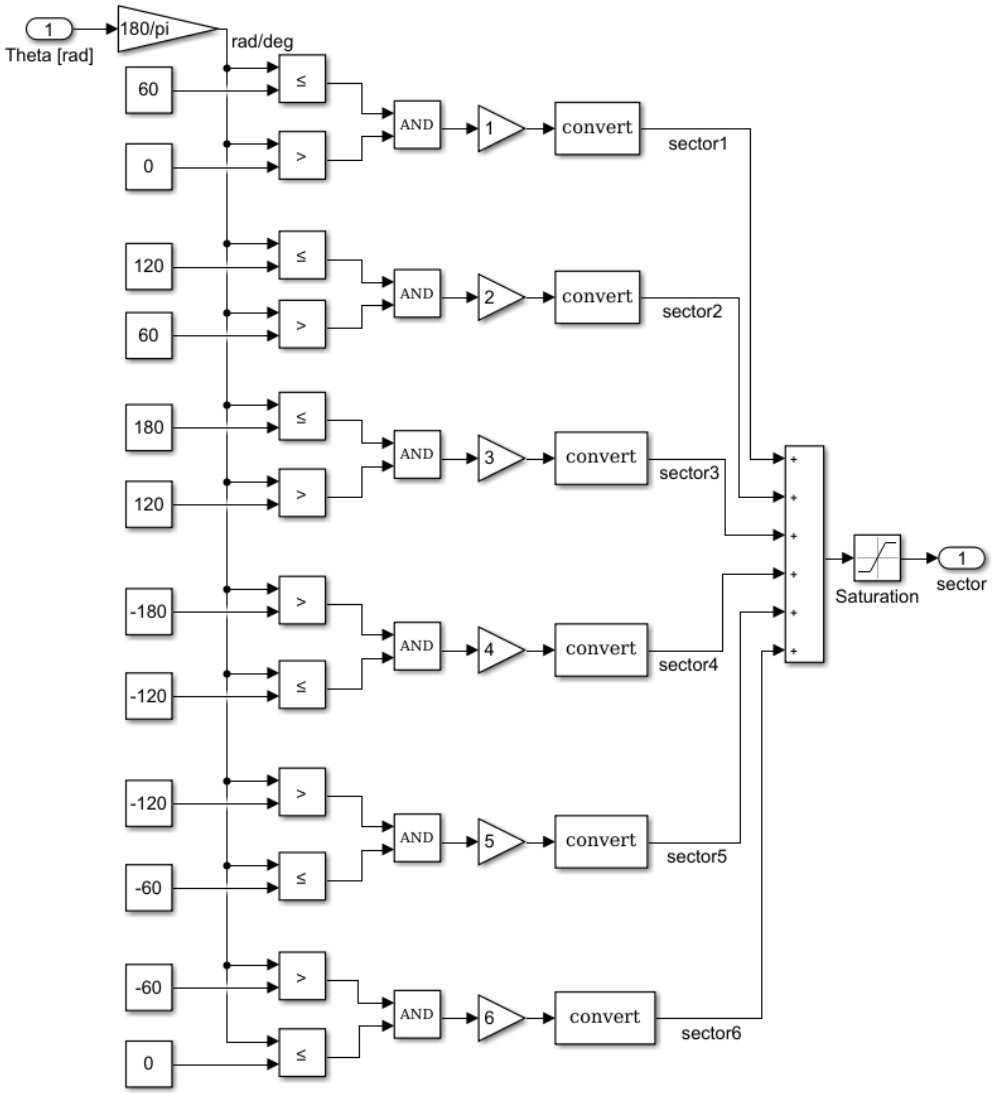

Figure 5.7: Sector Detection

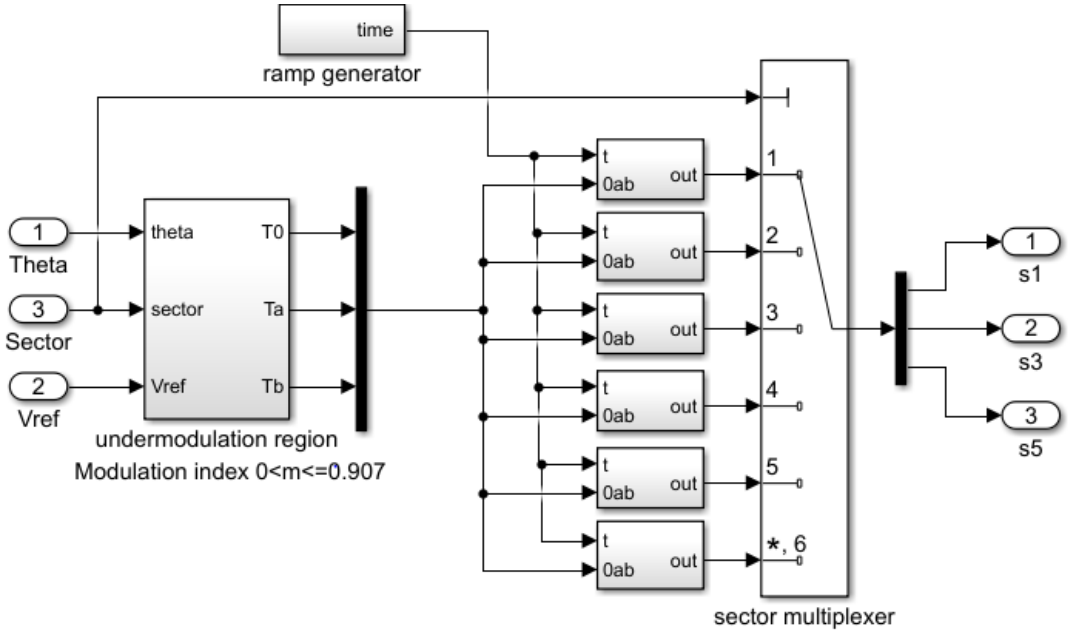

Figure 5.8: SVPWM Block

5.7 Voltage Source Inverter

Voltage Source Inverter block represents model of driver circuitry. It consists of MOSFETs, DC voltage source and logical NOT operators. Internal resistance of MOSFET is set to typical Drain-to-Source On-Resistance, which is $2.9m\Omega$, of used MOSFET [17]. V_a, V_b and V_c outputs are used as physical ports which are responsible for connection to phases of PMSM block. Inside of the block can be seen in Figure 5.9.

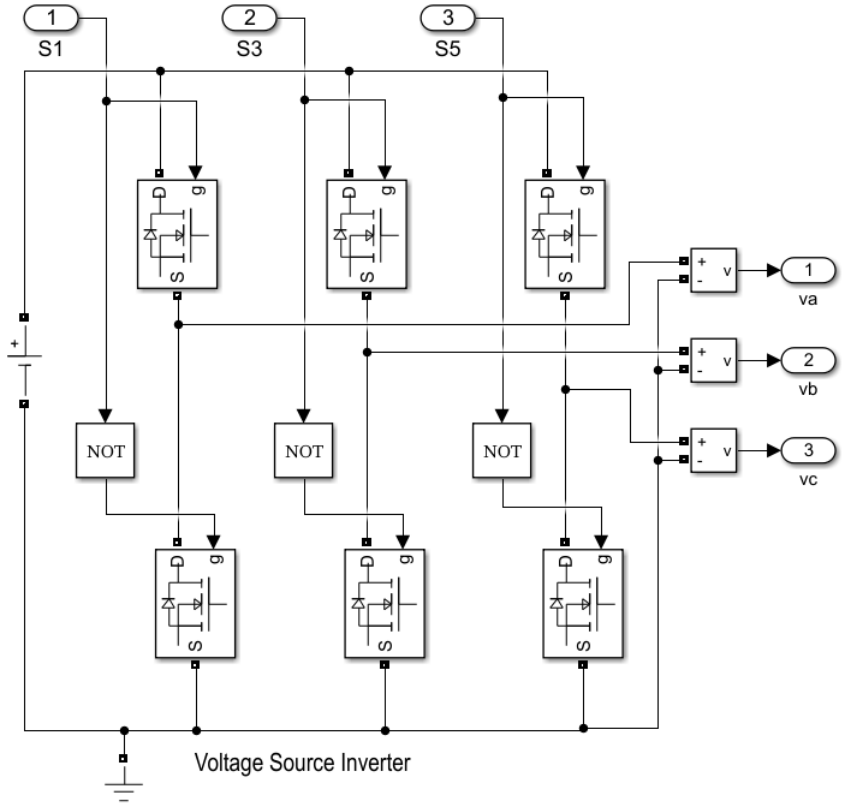

Figure 5.9: Voltage Source Inverter Block

5.8 Verification of the Model

Constant $i_q = 3000mA$ and $i_d = 0A$ current commands are applied. Additionally, load torque is stepped from 0 Nm to 0.2 Nm at time 0.015 s. In Figure 5.10, it is seen that feedback i_q current follows reference i_q value for a short amount of time. After, i_q starts to drop since back EMF increases. Then, i_q starts to increase up to 1 A. This increase results from load torque which is applied at time 0.015 s. $i_{a,b,c}$ current graphs

are also given in Figure 5.10. Since power variant domain transformations are used, $i_{a,b,c}$ amplitudes are equal to i_q amplitude as expected. In Figure 5.11, phase voltages

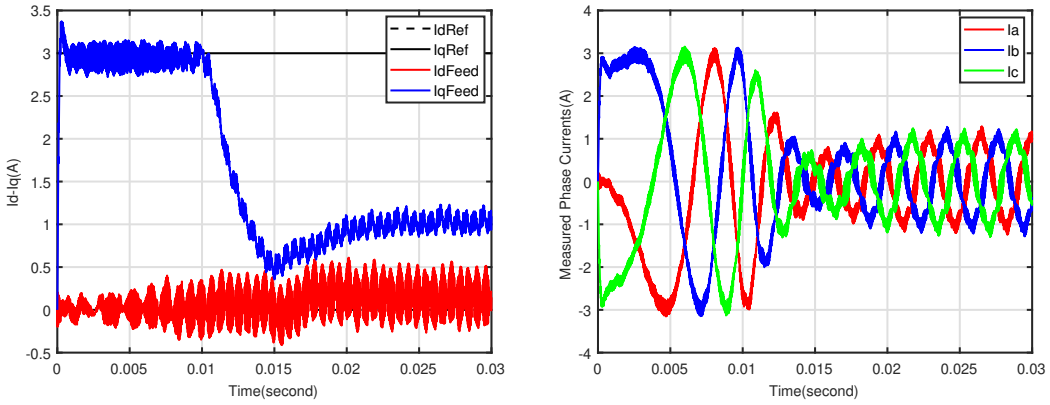

Figure 5.10: Produced abc and dq Currents, Constant i_q Command, 0 to 0.2 Nm Load

are plotted. Maximum amplitude of the waves are equal to $(2/3) * V_{dc}$ because of SVPWM nature. The same amplitude value is also observed in v_{dq} voltages.

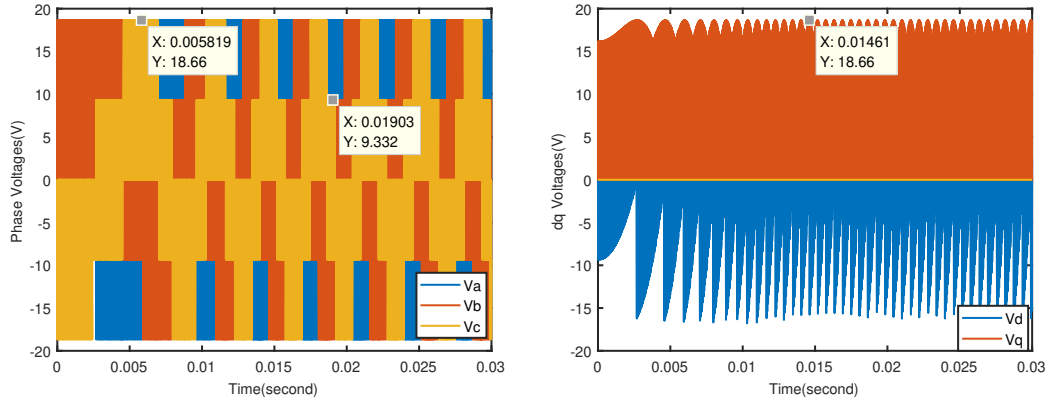

Figure 5.11: Produced abc and dq Voltages, Constant i_q Command, 0 to 0.2 Nm Load

5.9 PI Controller Based Design

In Figure 5.12, block diagram of PI controller based design is shown. PI parameters are taken from *Theory of Operation* chapter. Overall model mainly consists of controller, driver parts of PMSM and PMSM itself. Simulink model is created in MATLAB 2017a version. Some of the blocks, shown in Figure 5.12, are created from sub-blocks. These sub-blocks are gathered together and represented as an unity in order to decrease complexity of diagram. For further information, relatively complex blocks is explained in the previous sections.

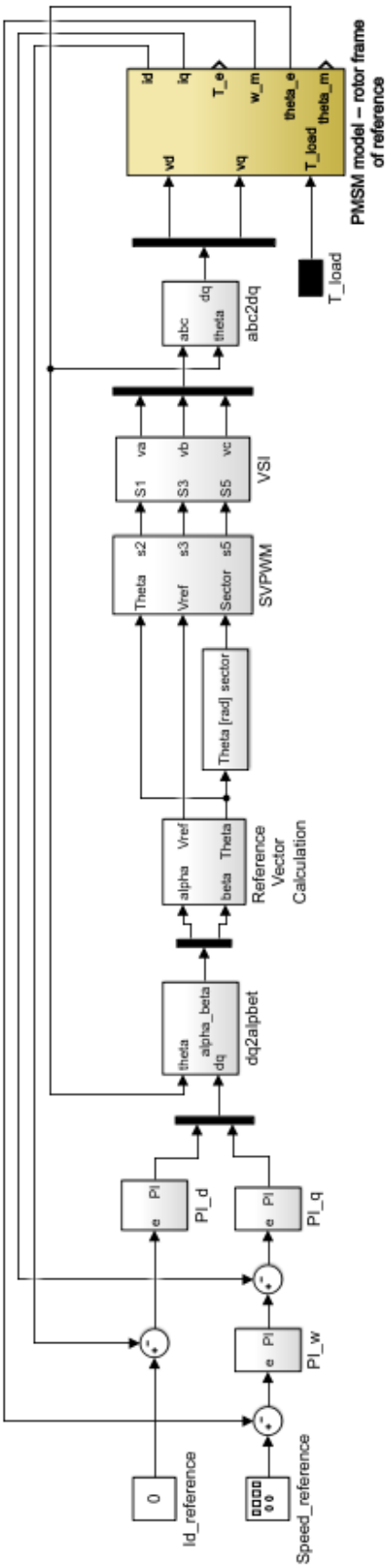

Figure 5.12: Simulink Model of the System with PI Controller

5.9.1 Step Speed Command under Load Torque

80 rad/s step speed command is applied at time zero. Then, 0.2 Nm load torque is increased to 0.5 Nm at time 0.1 s. Speed response is shown in Figure 5.13. After application of additional load torque at time 0.1, mechanical speed continues to track reference speed after 0.04 s later.

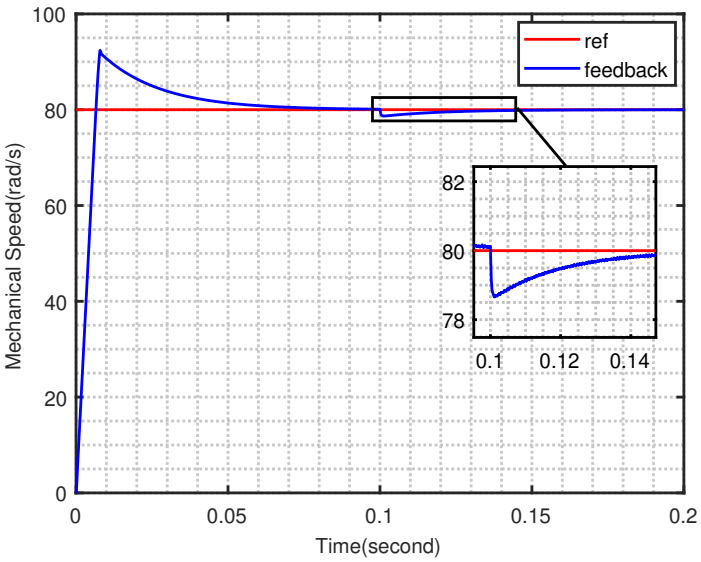

Figure 5.13: Speed Response, Step Command, 0.2 to 0.5 Nm Load

Produced torque and feedback I_q current graphs are given in Figure 5.14. As can be observed from the plots, magnitude of torque curve is proportional to magnitude of I_q current curve. It is an expected result because of relation between torque and I_q, given in Equation 3.9. Torque constant is 0.2 Nm/A as expected.

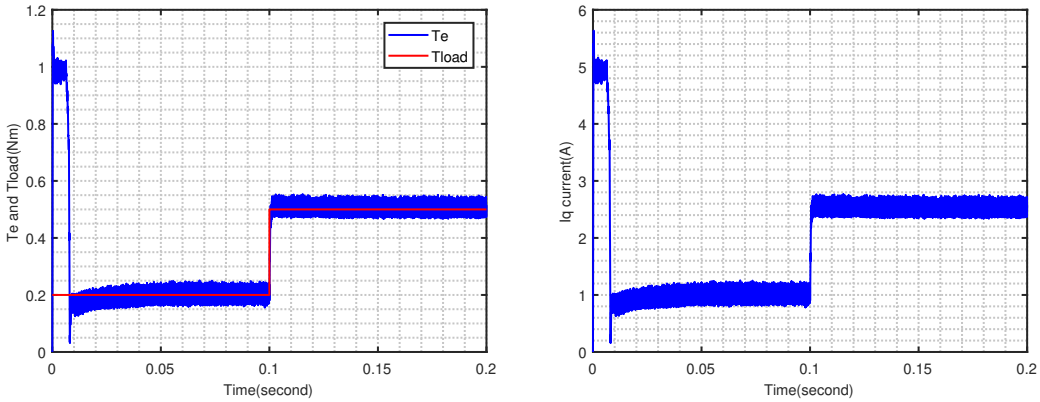

Figure 5.14: Produced Torque and Iq, Step Command, 0.2 to 0.5 Nm Load

Feedback (I_a, I_b, I_c) and (I_d, I_q) currents are given in Figure 5.15. As can be seen from the left figure, phase current magnitudes increase after load torque is applied. Also, I_d current is almost constant around zero as expected.

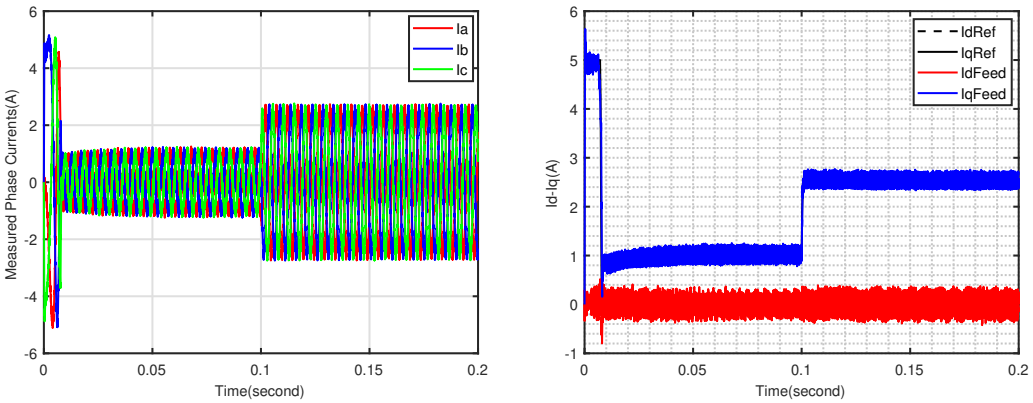

Figure 5.15: Feedback abc and dq axis currents, Step Command, 0.2 to 0.5 Nm Load

5.9.2 Speed Reversal Test under Load

Rectangular 10 Hz, $30 rad/s$ peak-to-peak mechanical speed command is fed into the controller. Load torque is constant and set as 0.3 Nm. Speed graph is given in Figure 5.16. Transient responses to different directions are shown.

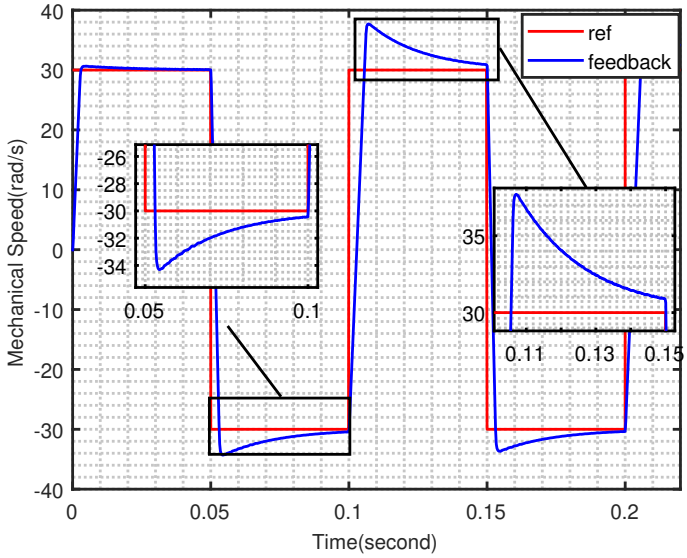

Figure 5.16: Speed Response, Speed Reversal, T=0.3 Nm

Produced torque and feedback I_q current graphs are given in Figure 5.17. Electromechanical torque is produced at the desired value. Fluctuations in torque graph is resulting from speed command change. It should be also noted that feedback I_q does not exceed the saturation limit, which is 6 A.

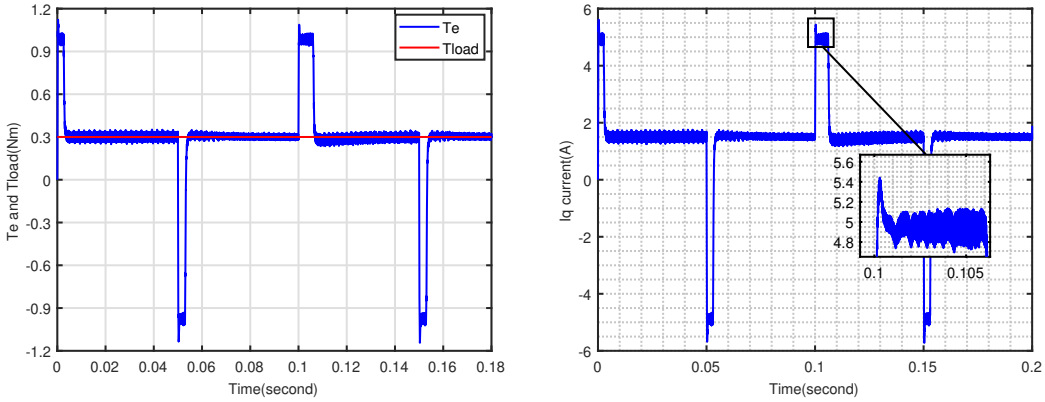

Figure 5.17: Produced Torque and Iq, Speed Reversal, T=0.3 Nm

Feedback (I_a, I_b, I_c) and (I_d, I_q) currents are given in Figure 5.18. It is observed that order of the phase currents reverses at time 0.05 s because of change of rotation direction. Additionally, I_d current is almost constant around zero as expected.

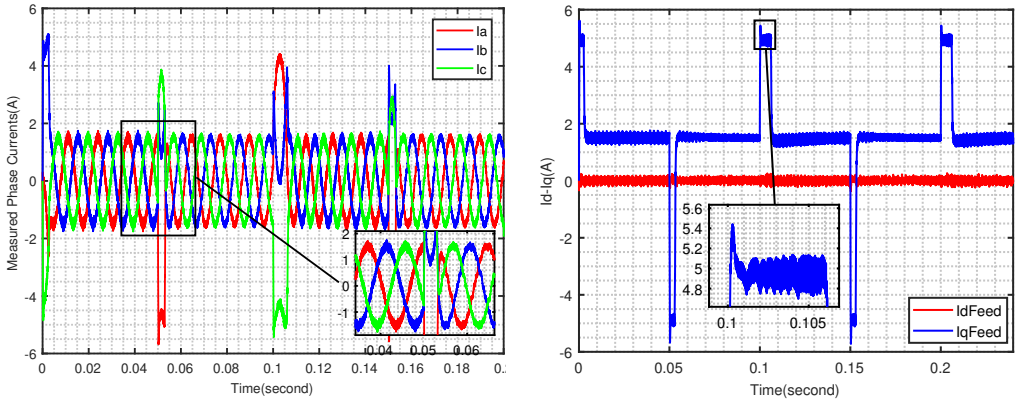

Figure 5.18: Feedback abc and dq axis currents, Speed Reversal, T_{load}=0.3 Nm

5.9.3 Chirp Speed Command

Bandwidth of the system is examined by using sweep signal. Chirp input signal is created according to parameters given in Table 5.2. Constant load torque is applied

as 0.3 Nm. Speed response to this chirp input is given in Figure 5.19. Also, last sine cycle is zoomed to measure lag between input and output signals in Figure 5.20.

Table 5.2: Chirp Signal Parameters

Frequency sweep	Linear
Sweep mode	Bidirectional
Initial frequency (Hz)	50
Target frequency (Hz)	100
Target time (s)	0.4
Sweep time (s)	0.4

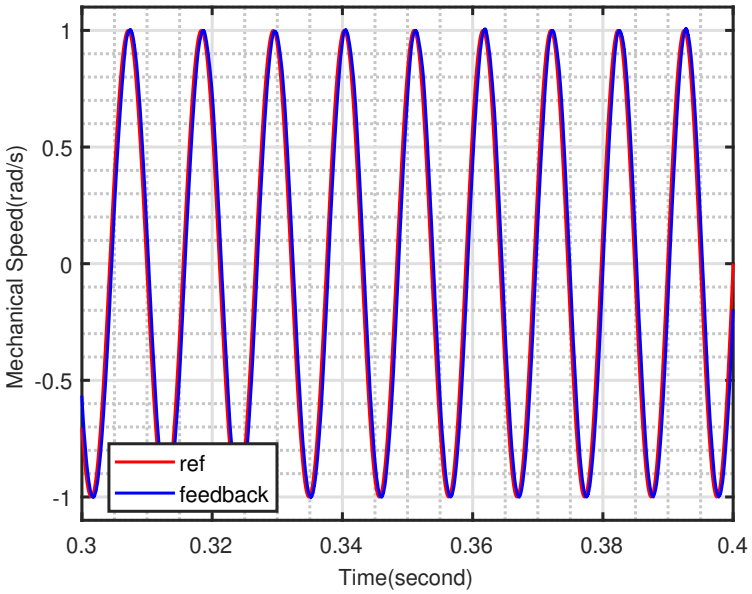

Figure 5.19: Speed Response to Chirp Speed Command

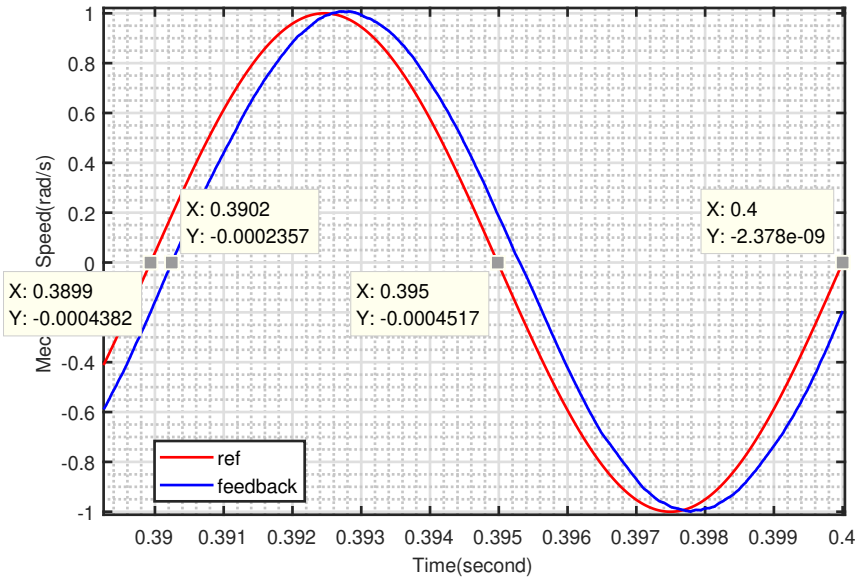

Figure 5.20: Zoom in Speed Response to Chirp Speed Command

5.10 LQR Controller Based Design

In Figure 5.21, LQR controller based block diagram is shown. State space model is constructed based on given formulas in *Theory of Operation* chapter. i_d and w_m states are chosen to be observed. Speed and i_d current reference commands are given with signal generator blocks. Feedback matrices F_1 and F_2 are calculated by embedded .mfile function. Chosen weight for Q and R matrices are $q_1 = 0.25$, $q_2 = 0.0025$, $q_3 = 0.00001$, $q_4 = 0.25$ and $q_5 = 10$; $r_1 = 0.05$, $r_2 = 0.0000025$, $r_3 = 0.0000002$, $r_4 = 0.1$ and $r_5 = 0.001$ respectively.

As mentioned previously, linearisation around current operating point should be done in order to utilize linear quadratic regulator. Therefore, linearisation points are chosen separately for each test to achieve optimal performance. These values are given at the beginning of relevant test procedure.

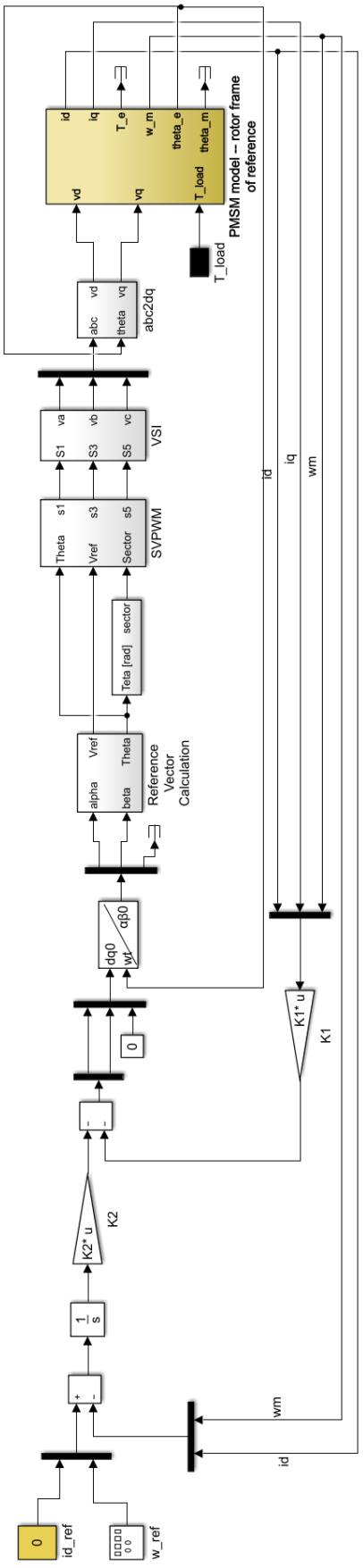

Figure 5.21: Simulink Model of the System with LQR Controller

5.10.1 Step Speed Command under Load Torque

80 rad/s step speed command is applied at time zero. Then, 0.2 Nm load torque is increased to 0.5 Nm at time 0.1 s. Speed response is shown in Figure 5.22.

Chosen linearisation point for i_d, i_q and w_m states is $(0A, 1A, 80rad/s)$. Since i_d is tried to be held constant, it is reasonable to linearise it around zero. As the same manner, w_m is chosen to be linearised at reference speed value. Finally, i_q linearisation point is determined to be equal to *desired torque/torque constant*. After making trial and error, between the range of 0.2 Nm and 0.5 Nm, 0.4 Nm is chosen to determine the value of i_q state.

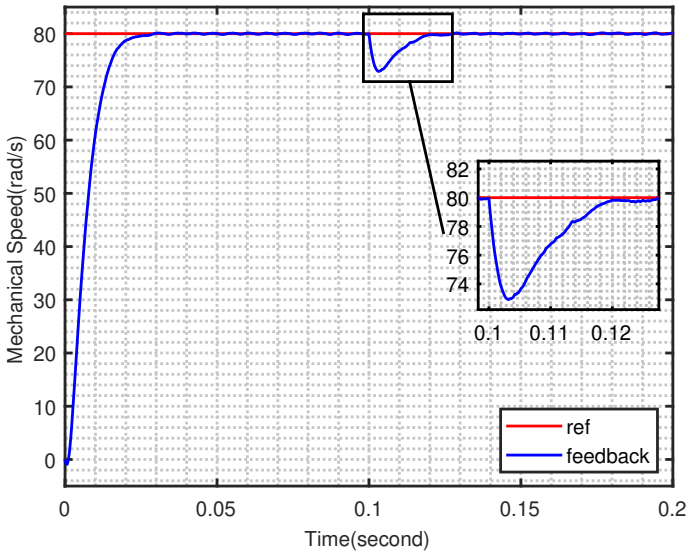

Figure 5.22: Speed Response, Step Command, 0.2 to 0.5 Nm Load

Produced torque and feedback I_q current graphs are given in Figure 5.23. As can be observed from the plots, magnitude of torque curve is proportional to magnitude of I_q current curve. It is an expected result because of relation between torque and I_q, given in Equation 3.9. Torque constant is 0.2 Nm/A as expected.

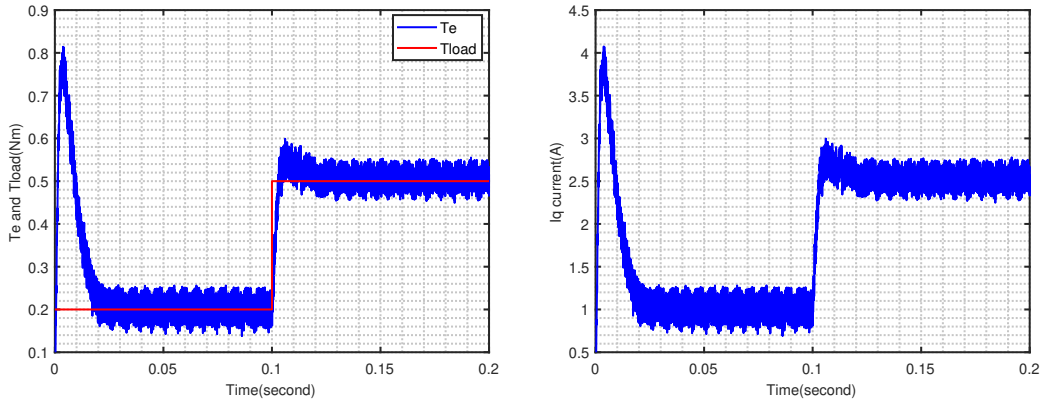

Figure 5.23: Produced Torque and Iq, Step Command, 0.2 to 0.5 Nm Load

As can be seen in Figure 5.24, phase current magnitudes increase after load torque is applied. It is because of the fact that the required electromechanical torque increases. The increased torque results in increase in I_q current. Consequently, phase current magnitudes also become bigger.

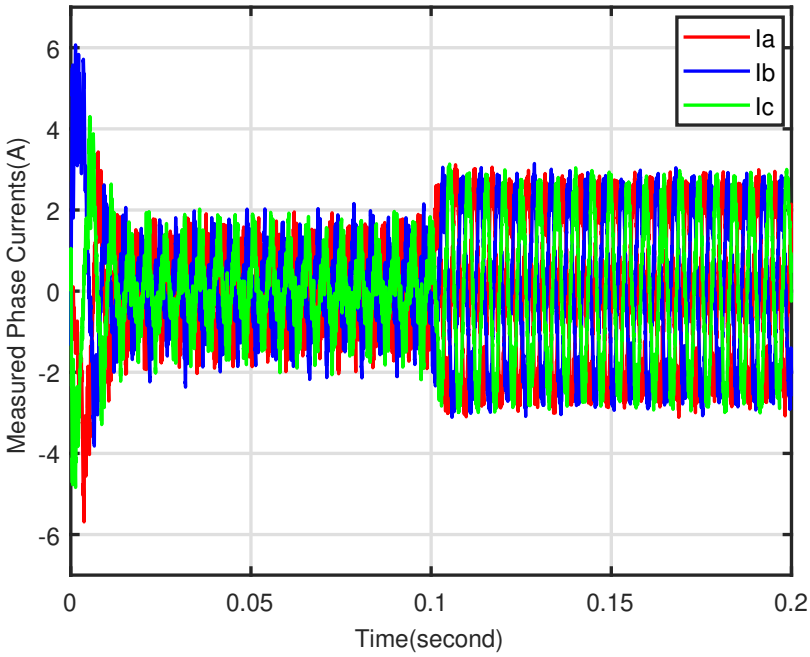

Figure 5.24: Phase Currents, Step Command

In Figure 5.25, I_d and I_q currents are given. I_d current is almost constant around zero as expected. I_q current has about 0.75 A peak-to-peak ripple. This ripple magnitude can be decreased by setting tighter constraint on I_q state.

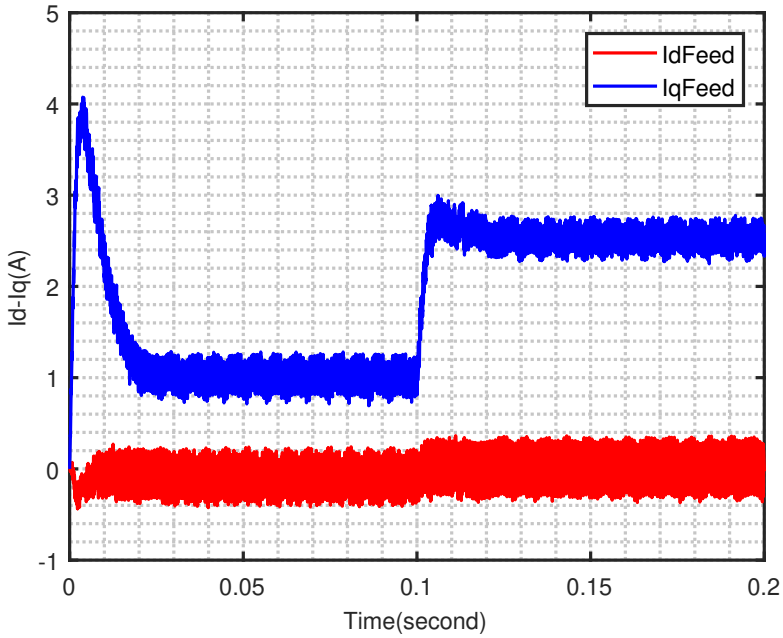

Figure 5.25: dq Current Response, Step Command

5.10.2 Speed Reversal Test under Load

Rectangular 10 Hz, $30rad/s$ peak-to-peak mechanical speed command is fed into the controller. Load torque is constant and set as 0.3 Nm. Speed graph is given in Figure 5.26. Transient responses to different directions are shown. Chosen linearisation point for i_d, i_q and w_m states is $(0A, 1A, 80rad/s)$. i_d point is determined in an similar manner as the previous test. Unlike the step speed command, the speed reference is not constant in this test procedure. It oscillates around zero. Therefore, it is reasonable to choose the middle point which is 0 rad/s. Finally, linearisation value for i_q is found as 1.5 A according to previously given *desired torque/torque constant* formula.

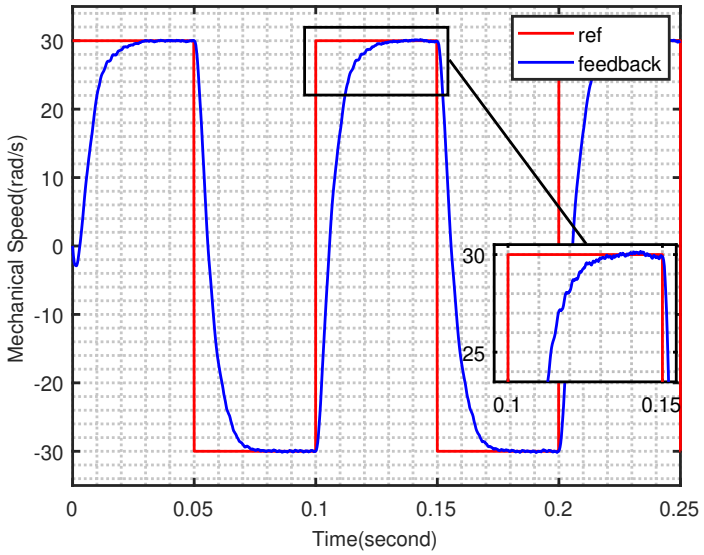

Figure 5.26: Speed Response, Speed Reversal, T=0.3 Nm

Produced torque and feedback I_q current graphs are given in Figure 5.27. Electromechanical torque is produced at the desired value. Changes in torque magnitude are resulting from speed command change.

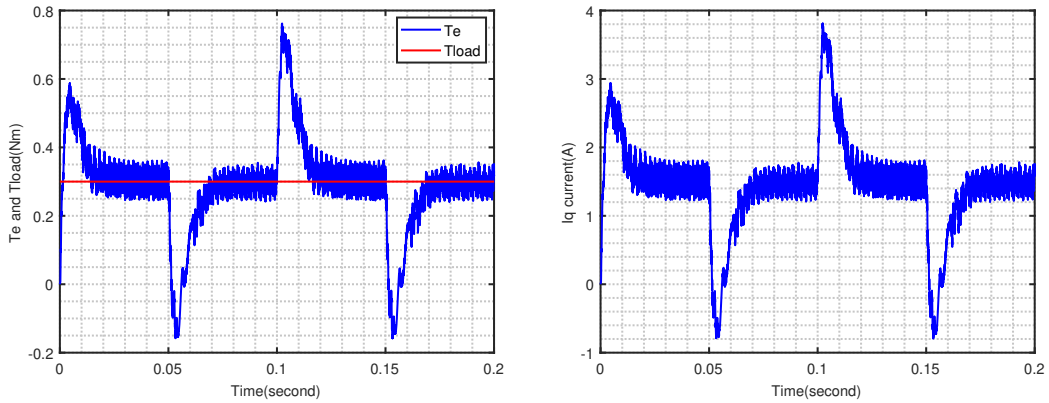

Figure 5.27: Produced Torque and Iq, Speed Reversal, T=0.3 Nm

Phase currents are given in Figure 5.28. It is observed that order of the phase currents reverses at time 0.05 s because of change of rotation direction.

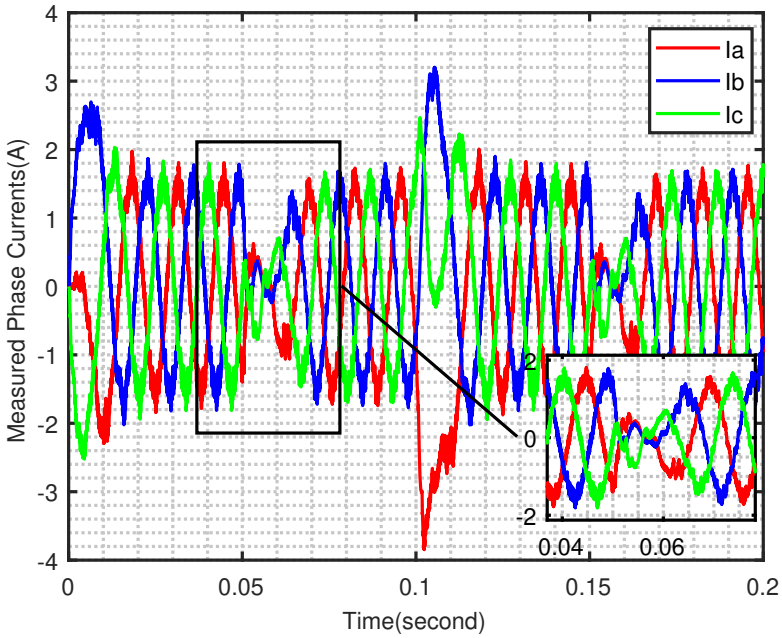

Figure 5.28: Phase Currents, Speed Reversal, T=0.3 Nm

In Figure 5.29, I_d and I_q currents are given. I_d current almost constant around zero as expected.

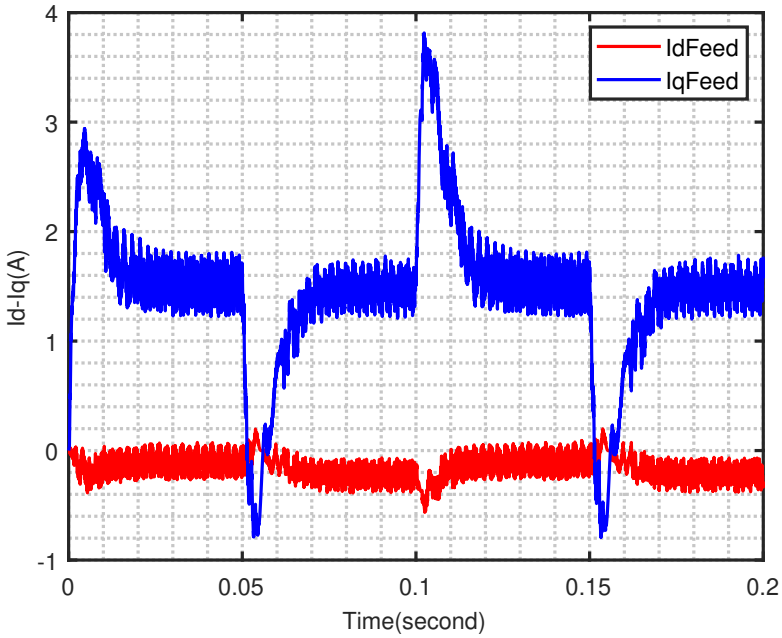

Figure 5.29: dq Current Response, Speed Reversal, T=0.3 Nm

5.10.3 Chirp Speed Command

Bandwidth of the system is examined by using sweep signal. Chirp input signal is created according to parameters given in Table 5.3. Constant load torque is applied as 0.3 Nm. Speed response to this chirp input is given in Figure 5.30. Also, last sine cycle is zoomed to measure lag between input and output signals in Figure 5.31.

Table 5.3: Chirp Signal Parameters for LQR

Frequency sweep	Linear
Sweep mode	Bidirectional
Initial frequency (Hz)	0
Target frequency (Hz)	25
Target time (s)	1
Sweep time (s)	1

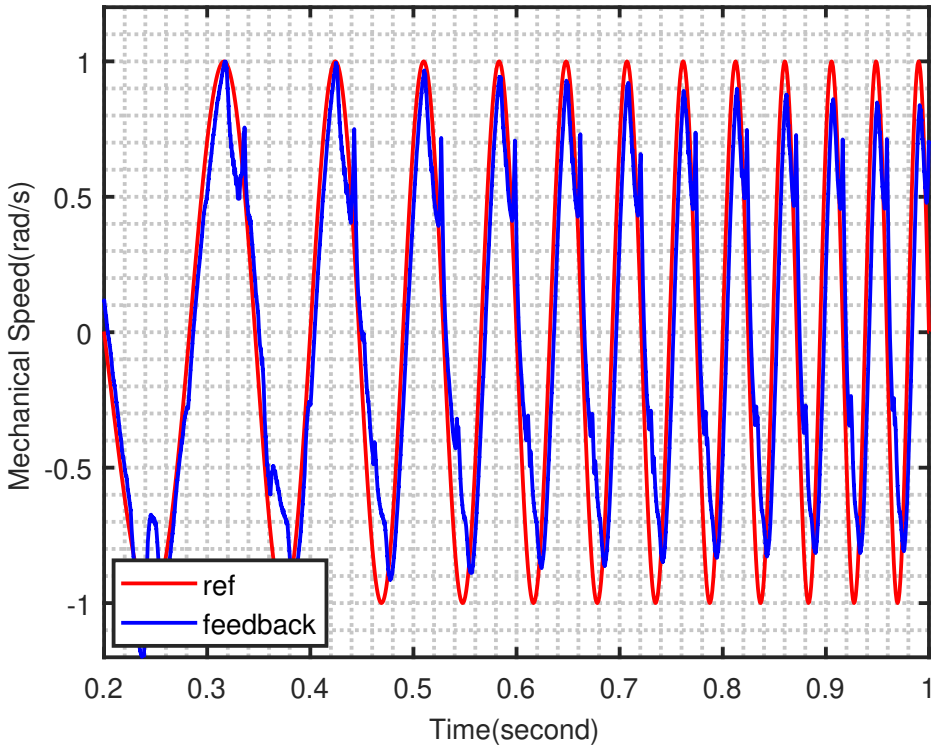

Figure 5.30: Speed Response to Chirp Speed Command

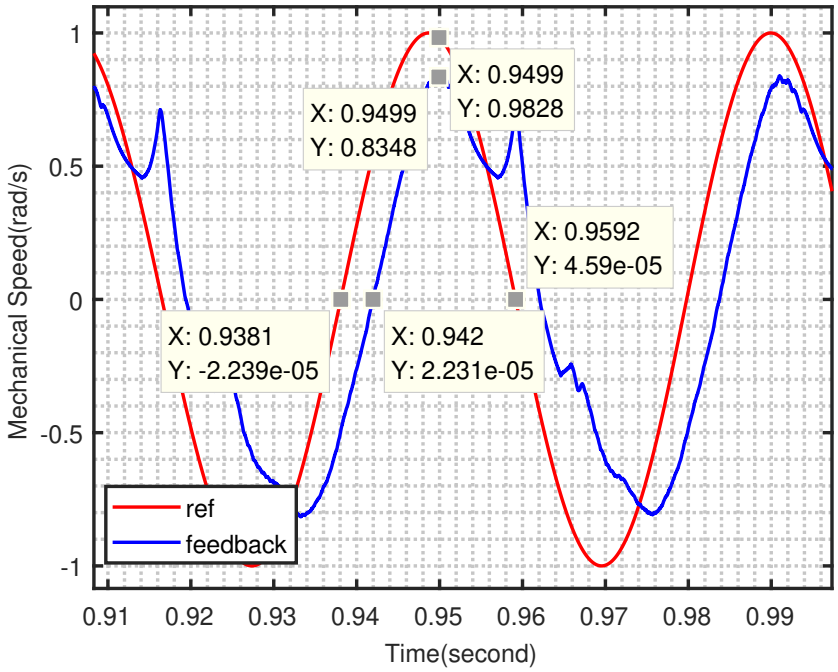

Figure 5.31: Zoom in Speed Response to Chirp Speed Command

5.11 Performance Comparison of the Controllers

As explained previously, different test procedures are applied to analyse performance of the designed controllers. The test outcomes are summarized in the following sections.

5.11.1 Step Speed Response Behaviour of Controllers

The first test procedure is step speed command with changing load behaviour. PI controller has approximately 10 rad/s overshot, 0.05 s settling time. Additionally, it is reasonable to say that PI controller is robust to disturbance. It deviates from the reference speed 2 rad/s after application of additional torque.

Torque ripple is observed as 0.075 Nm, it is independent of load torque value. This ripple results from application of chosen commutation strategy. It is beneficial to have a system which has predictable torque ripple within tolerable range. Additionally, it is seen that I_a, I_b and I_c currents have maximum 5 A amplitude. Final thing to underline that phase currents stay below maximum allowed phase current limit which is 7 A.

LQR response characteristic to the step command can be summarized as follows. First of all, it sets to the desired speed value in 0.03 sec. Secondly, it does not display overshot. Thirdly, it diverges from speed reference 6 rad/s when load is increased at time 0.1.

Torque ripple of LQR changes under different load conditions. The system has slightly bigger torque ripple for load 0.2 Nm than 0.5 Nm. This difference results from the chosen linearisation point for torque which is 0.4 Nm. Since the second half of the test period has closer load value to linearisation point, it is a predictable consequence. Finally, it is observed that LQR causes to creation of bigger phase currents. It is consistent with observed faster setting time as compared to PI controller.

5.11.2 Speed Reversal Behaviour of Controllers

The second test procedure is speed reversal profile under constant load. It is observed that PI controller does not settle as quick as step command. Additionally, it has 8 rad/s overshot.

For inner current control loops, overshot and settling time parameters are more satisfying as compared to parameters of the speed loop. On the other hand, I_q current reaches considerable amount of magnitude at reversal moments. Additionally, I_q current ripple is around 0.5 A in steady state. I_a, I_b and I_c phase current values are under 5 A during test procedure.

In addition to PI controller, LQR based model features can be given as follows. LQR is superior to PI in terms of speed overshot. It does not cross the reference speed value. On the other hand, it has worse settling time performance as compared to step speed test. Therefore, it can be concluded that both of the speed controllers have difficulty to settle after speed reversal moments.

Moreover, it can be said that I_q current loop of LQR works more efficiently than PI's. It is observed that I_q values do not cross 4 A. This superior performance is a consequence of constraints which are specified through Q and R matrices in order to minimize cost function. As a result of smaller I_q and I_d values, I_a, I_b and I_c phase currents are also smaller as compared to currents PI controller.

5.11.3 Conclusion

As a result of the discussion about different test scenarios, it can be said that LQR presents better performance in terms of settling time, overshoot. On the other hand, it suffers from current ripple.

In *Theory of Operation* chapter, both of the controllers are linearised according to some assumptions. Then, the controllers are designed by taking only the motor model into consideration. It is because of the fact that other blocks are also nonlinear. Without making overall system identification, it is not easy to predict system behaviour. That is the reason way conducted tests, in Simulink, reveal results which have differences from theoretical calculations. Still, required system behaviour can be obtained based on simplified system model by asserting stricter constraints than the needed. This gives a designer space for errors resulting from model simplification.

As stated previously, LQR is constructed based on the chosen linearisation points. For the scope of the thesis, it is assumed that choice of the linearisation point is made at the beginning of the operation according to the operating region. Therefore, LQR generally shows better performance with respect to PI controller. On the other hand, it should be noted that LQR may not display better results for all operating region.

In order to guarantee coverage of the overall operating region, system linearisation should be repeated during operation. Repeating the procedures of linearisation according to the latest state vector and calculation of controller gains, based on minimization of cost function, require a huge computational capacity. Therefore, implementation of LQR on hardware is relatively complex solution. Consequently, hardware implementation of PI controller is advantageous over LQR as long as system requirements are met. Therefore, PI controller based design is decided to be implemented because of its cost/performance optimization.

CHAPTER 6

FPGA IMPLEMENTATION

In order to control PMSM, control algorithm should take care of three main tasks which are sense of position data, handling of commutation and control motor torque/speed. This study is implemented on Vivado 2015.3 by using VHDL. Functional block diagram of current controller is shown in Figure 6.1.

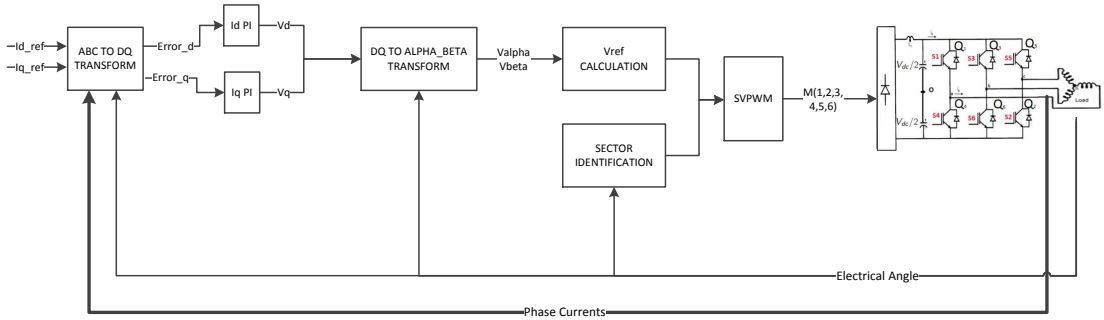

Figure 6.1: Functional Block Diagram of Current Controller

6.1 Current Controller

Current controller module is basically designed for producing motor currents according to commands which are produced by outer control loop. This module can be perceived as a black box, which is fed by motor feedback currents, current commands and rotor feedback position, controls motor driver circuit to create desired current waveform.

In order to have an easy-reading VHDL code, current controller module divided into smaller, more manageable sections. For each motor in the system, there is one top module which is in charge of communication between sub-modules. These sub-modules can be sorted by operation sequence as feedback current acquisition, park transformation, error calculation, PI controller, inverse park transformation, space vector PWM calculation and space vector PWM commutation modules. The above-

mentioned modules have also sub-modules under them. Each one of the modules will be examined in the rest of this chapter.

6.1.1 Motor Feedback Currents Reading

Motor feedback currents are obtained from current transducers which gives voltage output corresponds to measured current. These voltage values are read with ADC7644 chips. First of all, reading mode is specified and parallel 14 bit phase-a and phase-b data are read by using SPI-compatible serial interface. Then phase-c is calculated from these two phase currents. Thirdly, 64 subsequent samples are summed up and divided by 64 in order to eliminate one-time noises. Finally, offset error resulting from non-ideal behaviour of current sensor is subtracted from average current value. Overall diagram of motor feedback current reading block is given in Figure 6.2.

6.1.1.1 Currents Acquisition

This module is essentially responsible for driving analog to digital converter chip. ADC chip converts analog value coming from two current sensors into digital value which can be interpreted by FPGA.

Choice of ADC in servo control systems has an importance in terms of controller tracking performance. For system with high operating speed, phase currents change frequently. Therefore, sampling rate of ADC should be high enough to capture feedback current in an accurate way. Therefore, among three modes of AD7944, which are split reading, reading during acquisition and reading during conversion, split reading mode is selected because of higher sampling rate requirement [44].

The second design aspect is choice of current sensor. Calculation of required current accuracy is important to meet system requirements. On the other hand, designer should be aware of the fact that improved accuracy may cause increase in cost and required PCB surface area for the sensor. For this purpose, it is decided that only two of the motor phase currents are sensed. The third phase current is calculated based on the following equation.

$$I_C = -(I_A + I_B) \tag{6.1}$$

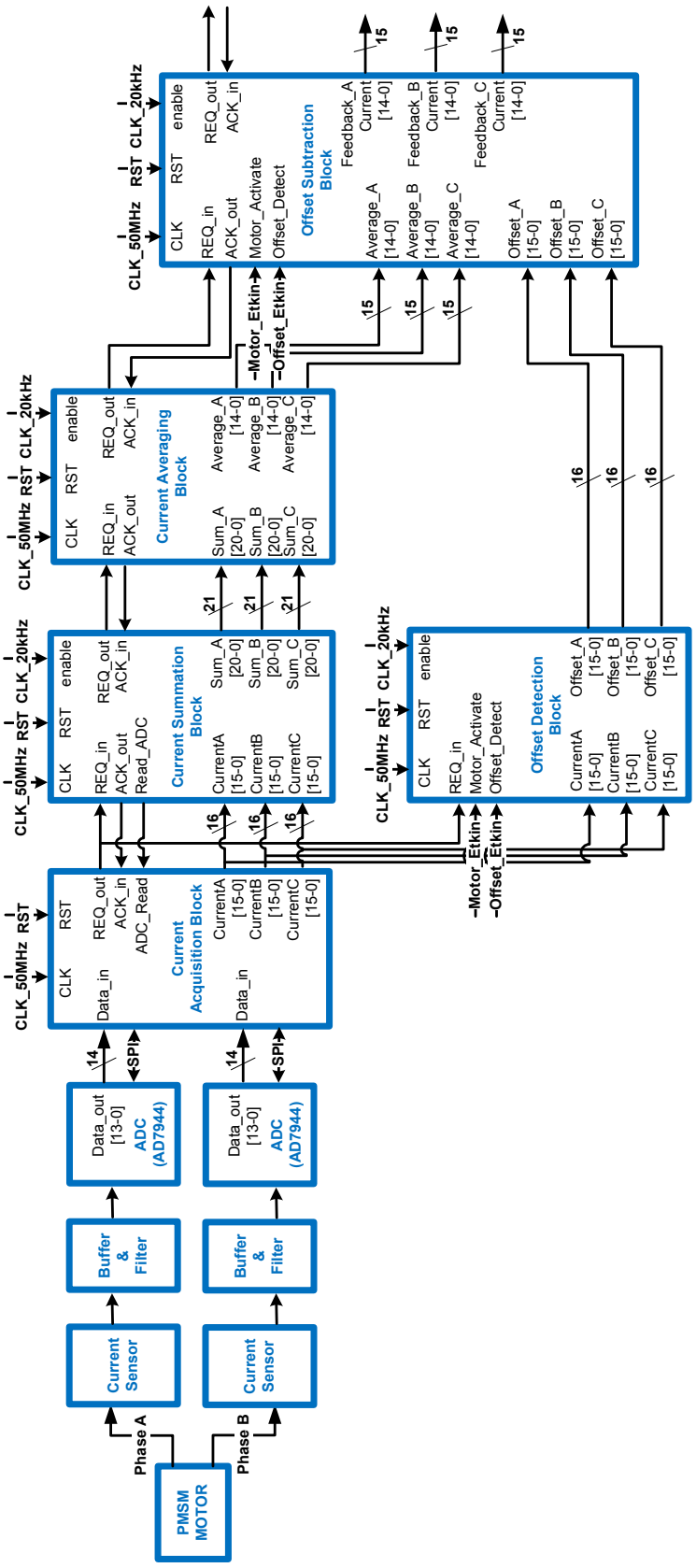

Figure 6.2: Feedback Current Reading Block

Used current transducer produces 2.5 V when there is no current flows through it. For positive currents, it produces higher voltage level than 2.5 V. In same manner, for negative currents, vice versa. Output voltage of current sensor is calculated from the following equation:

$$V_{out} = V_{ref} + (I_P * G_{th}) \tag{6.2}$$

where V_{out} is output voltage of current sensor, V_{ref} is reference voltage which is 2.5 V in our case, G_{th} is theoretical sensitivity and I_P is primary current. Current sensor and ADC parameters are summarized in Table 6.1.

Table 6.1: Current Sensor and ADC Parameters

Parameter	**Value**	**Unit**
G_{th}	100	mV/A
V_{ref}	2.5	V
Primary current, measuring range	-20, +20	A
Output Voltage Range of current sensor	0.5, 4.5	V
Output Voltage Range of the ADC chip	5	V
Resolution of the ADC chip	14	bit
Bit sensitivity of the ADC chip	0.3052	mV
Scale factor of current	327	A^{-1}

Input range of the current sensor is determined according to peak current limit of the used motor. Input range of current sensor should be bigger than current limit value of the motor in order to take precaution for undesired cases. Scale factor calculation is based on resolution of both current sensor and ADC. By means of $0.3052mV/100mV/A = 327A^{-1}$ calculation, 1 Ampere input current corresponds to decimal 327 in digital current register. This scale factor is used in monitor interface to interpret binary values.

6.1.1.2 Offset Currents Calculation

There are many factors which can cause error in current feedback such as non-ideal behaviour of current sensor and filter circuits at input of current sensors and ADC chips.

The overall inaccuracy of current sensors consists of electrical offset, sensitivity error and linearity error. The electrical offset is a voltage produced by magnetic core of transducer when zero current flows through inside of current sensor. Upper and lower value for offset voltages are given in datasheet. This value could be different for each sensor because of uniqueness based on production.

The second error component, sensitivity error, is caused by the temperature. The sensitivity of a sensor is calculated around the definite temperature point. Apart from this optimal value, sensitivity could differ for different temperatures between the limits of upper and lower sensitivity error.

The third error factor is a linearity error which is discrepancy with theoretical linear output signal and real non-linear output signal. Linearity error differs by measured current magnitude.

Because of these non-linear factors affecting measurement accuracy, a moderately simple way is chosen to obtain more accurate measurement. When there is no current flows in sensor, output voltage of current sensor is sampled and summed during definite time. Then this summation is divided and an average offset value is obtained.

This summation and averaging procedure is repeated until motor activation command comes from the processor. With this way errors related to temperature effect and production process will be diminished. However, one cannot claim that the result is error-free. There is one more way to increase accuracy of measurement which is creating a look-up table for operational range of current magnitude and temperature. However, this method increases complexity of design in terms of resources usage and clock domain constraints.

6.1.1.3 Phase Current Summation and Averaging

These modules are responsible for averaging certain amount of current samples which are obtained during one cycle of current control loop. Certain amount of samples are firstly summed up. Then the sum is divided by this number with the aim of improving accuracy of thee measurement. Divisor is chosen according to current controller loop frequency and total amount of time, which is left for other computations.

Pulse width modulation frequency is chosen as 20 kHz; therefore, feedback current reading and calculations, related to current controller, must be completed within 50 us. Each averaging process is completed somewhere near end of the cycle. Then, the remaining time is used for other current controller's submodules which will be explained in a detailed way in the following parts.

In summary, MOSFET's ON scheme and their duration, which were calculated in *cycle n*, are applied to MOSFETs in *cycle n+1*. Figure 6.3 summarizes sampling and PWM cycle relation. Sum and average current register widths are determined

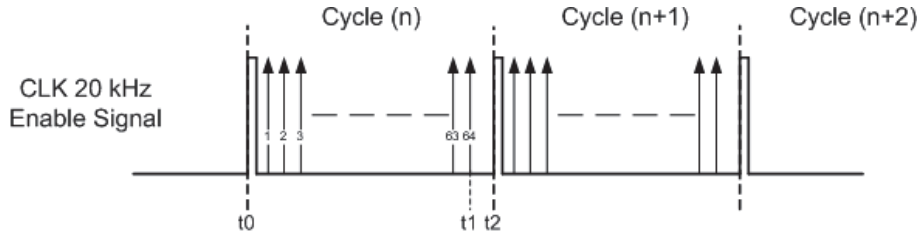

Figure 6.3: Current Sampling Scheme

according to absolute maximum values. Previously, it is stated that the maximum input current which current sensor accepts is 20 A and scale factor was found as 327 A^{-1}. Therefore, maximum value, of which current sum register can take, is 418560 $(= 20 * 327 * 64)$. Consequently, 20 bit register is enough to capture summation value in signed magnitude format.

The division operation is realized by shift right operator. The designer should take into consideration that values are represented in signed magnitude format. It means that the most significant bit is reserved as a sign bit and rest of the bits represent the magnitude. Therefore, shift right operation should be done as a aware of signed format. Firstly, sign bit is saved to another register to remember after shifting. Secondly, sum register is shifted to right 6 bit in order to divide the register with 64. Finally, the sign bit is put into the most significant bit of average register.

6.1.2 Park Transformation

Park module is implemented for calculation of desired direct and quadrature currents which are moving with rotor axis. Basically it is a matrix multiplication of phase

currents with some sine values. Park transformation equation (3.3) is realized in this module. Block diagram of module is illustrated in Figure 6.4.

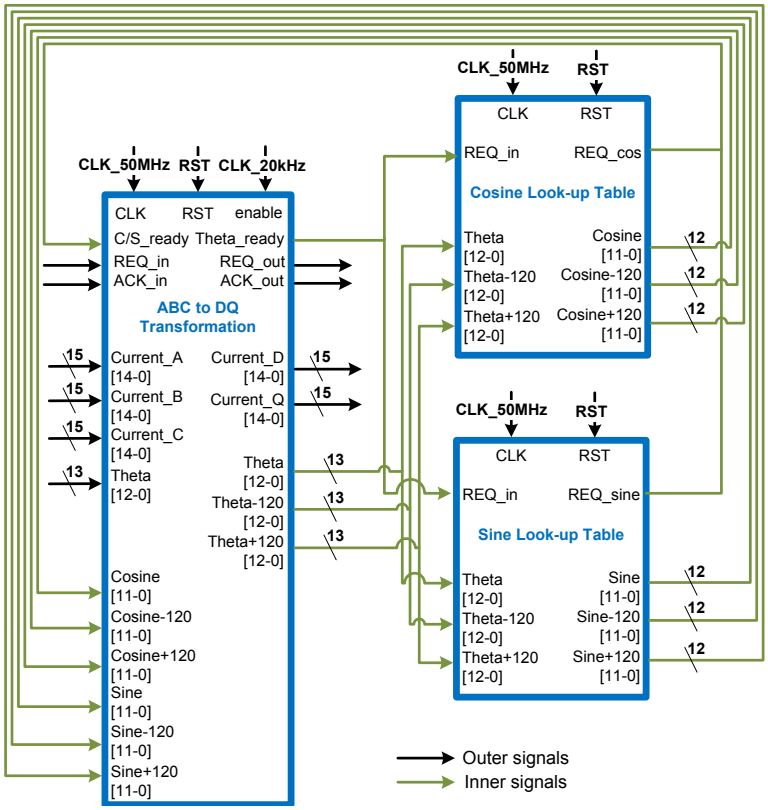

Figure 6.4: Park VHDL Block

Sine and cosine values are directly obtained from sub-modules of park transformation module. These sub-modules are look-up tables for sine and cosine values. The look-up tables are basically arrays which are made up of 3600 elements. It means that it has 0.1 degree input resolution. -1000 and +1000 are absolute maximum values of outputs. For example, output of sine module, which corresponds to $+90°$ and $-90°$, are +1000 and -1000 respectively. Similarly, output resolution can be found with $\frac{1}{2^{output\ register\ width}}$ formula. Since, output register width is 12 bit, output resolution is smaller than 0.00025 $(1000/2^{12} = 0.244)$.

In order to ease the calculations in VHDL point of view, NUMERIC_STD package is added to project's library. Phase currents are defined in signed format at the beginning of the module. Then multiplication and summation steps are done with defined functions of this packages.

As can be seen in Equation 3.3, abc to dq transformation requires fractional multiplication. Since floating point calculations are complex and increase resource use, fixed point arithmetic is often preferred to floating point one. XILINX offers "Divider Generator" IP for integer division. However, using commercial IP comes with the price such as limitations on supported device family, supported used interfaces. It means that design cannot offer flexibility of reusability in other hardware platforms. Additionally, used algorithm demands larger area and longer time to make calculations for larger bits [40]. Faster throughput rate is another factor of increase in hardware resource usage. Therefore, moderately simple method is chosen for fixed point division in the scope of thesis. It realizes the operation in two clock cycles. Instead of division operator, multiplication and shifting operators are used.

For instance, division by 3 could be implemented by simply multiplication with 43 and right shift of 7 bit position. It is obvious that accuracy is directly related to the number of bits which are used to quantize the divider. As stated in Table 6.1, current sensitivity of design is 3.058 (327^{-1}) mA. Therefore, it is acceptable to quantize the divider with 8 bits. In the rest of VHDL design, the same approach is used for fixed point division with different multiplication and shifting parameters.

6.1.3 PI Controller

Current and speed controllers should be designed in such a way that they cannot cross electrical or physical limits such as peak current or maximum motor speed. Therefore, a designer should put saturation limits to avoid overstress on the system.

Integrator Windup is a phenomenon used for situations in which unstable modes of the regulator may drift to undesirable values as a result of actuator saturation [5]. Consequently, it may be harder to reach stable mode for the system. Conditional integration method is chosen to be applied in the scope thesis. In conditional integration, integral term is updated as long as certain condition is fulfilled. Our condition is determined according to the chosen PWM method. As previously mentioned, reference voltage vector is expressed in terms of SVPWM base vectors. Since base vectors are equal to $2V_{dc}/3$, PI windup limit is set to this value. When integral term is calculated

beyond these limit, PI term is not updated to prevent actuator saturation. For the sake of completeness, state diagram of controller is given in Figure 6.8.

Windup problem should be taken into an account if PI controller's output is limited to saturation value. Since controller is limited with capabilities of actuator, steady state error is continued to be integrated. Therefore, anti-windup strategy should be implemented. *Tracking* and *conditioned* architectures are mostly preferred ones in the literature [29].

In tracking anti-windup method, input of integrator is tried to be reduced by feeding back difference between actual controller and saturated output. The difference between these two output value is multiplied K_{lim} gain. Block diagram of PI controller with tracking anti-windup method is shown in Figure 6.5.

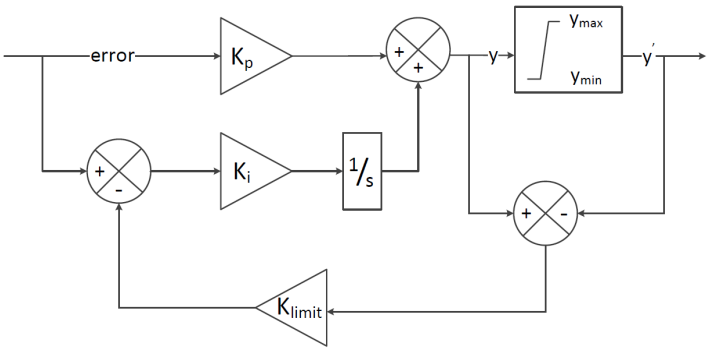

Figure 6.5: PI Controller with Tracking anti-windup [12]

In conditional anti-windup method, output of integrator term is used if its value under pre-determined limit. Therefore, error cannot uncontrollably increase in saturation region. Once the saturation condition disappear, integral term is activated again. Block diagram of PI controller with conditional anti-windup strategy is illustrated in Figure 6.6. This method is chosen to be implemented in our design because its convenience of implementation in digital controllers [29].

As previously mentioned in Hardware Description chapter, PI controller is implemented as a current controller. There are a plenty of methods for discretization of integral term in literature. Among these methods, rectangle approach is chosen for integral approximation because of its simplicity. PI controller continuous domain equation and discrete domain approximation, based on a rectangular method, are given

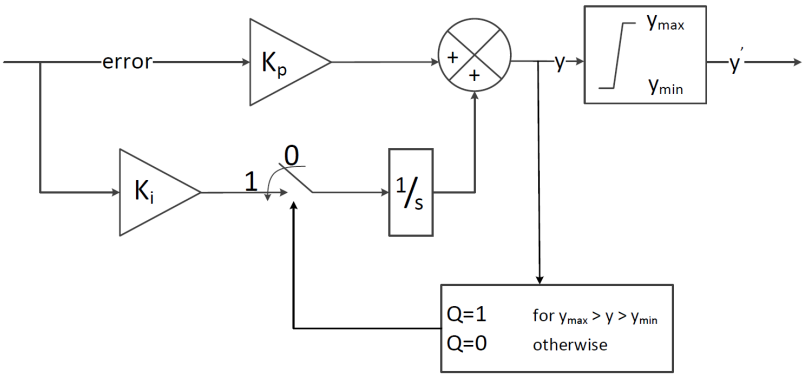

Figure 6.6: PI Controller with Conditional anti-windup [12]

below.

$$PI\left(t\right) = K_i \int_0^t e\left(t\right) dt + K_p e\left(t\right) \tag{6.3}$$

In Equation 6.3, K_i is an integral gain parameter, K_p is a proportional gain parameter, $e\left(t\right)$ is an error term and t stands for an instantaneous time.

$$PI\left[n\right] = TK_i \sum_{n=1}^{N} e\left[n\right] + K_p e\left[n\right] \tag{6.4}$$

In Equation 6.4, K_i is an integral gain parameter, K_p is a proportional gain parameter, $e\left(t\right)$ is an error term and T $(1/20000)$ stands for a time interval. Connections of PI VHDL block with other blocks are shown in Figure 6.7.

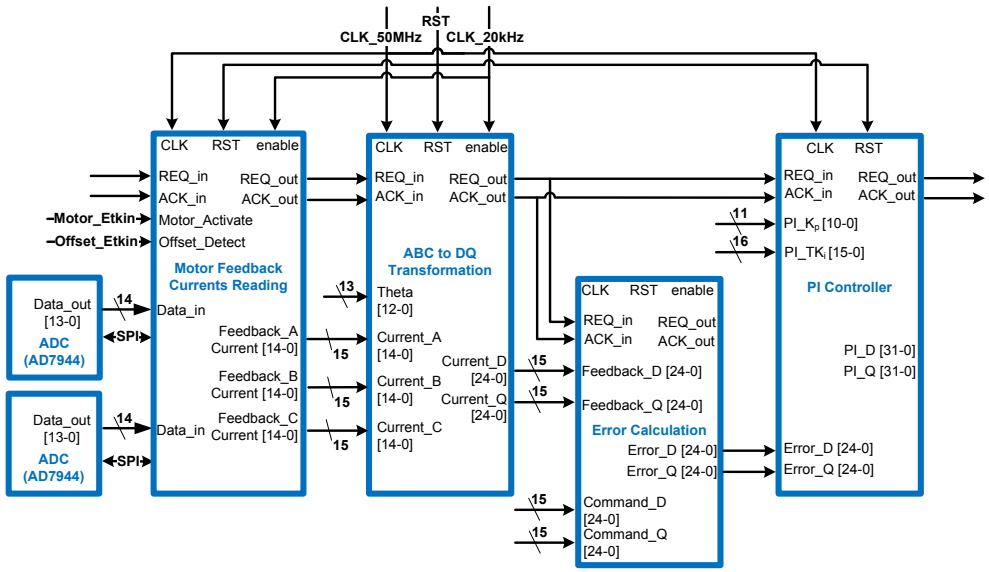

Figure 6.7: PI VHDL Block

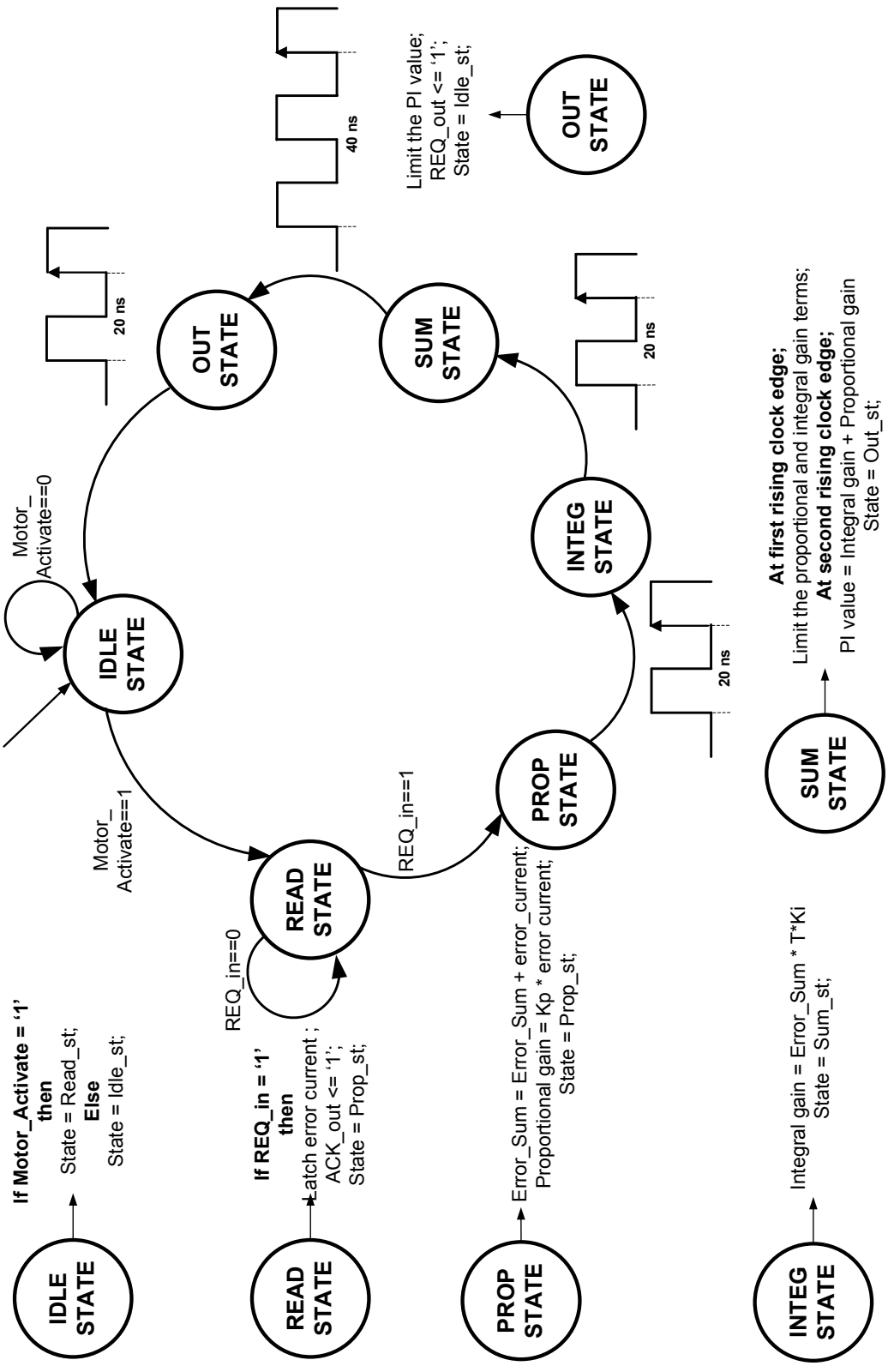

Figure 6.8: PI Module State Machine Diagram

6.1.4 Inverse Park Transformation

Inverse Park module is implemented to transform quantities from rotating reference frame into two-axis orthogonal stationary one. Equation 6.5 is named as Inverse Park transformation. This transformation matrix is calculated by finding inverse of Forward Park transformation matrix (3.2).

$$\begin{bmatrix} u_\alpha \\ u_\beta \\ u_0 \end{bmatrix} = \begin{bmatrix} \cos(\theta) & -\sin(\theta) & 0 \\ \sin(\theta) & \cos(\theta) & 0 \\ 0 & 0 & 1 \end{bmatrix} \begin{bmatrix} u_d \\ u_q \\ u_0 \end{bmatrix} \tag{6.5}$$

Similar to Park transformation, sub-modules are used to calculate needed sine and cosine values. To shorten operation cycle, look-up tables are used for trigonometric calculations instead of using XILINX IP. Since look-up table array length and maximum output values are same with ones used in Subsection 6.1.2, input and output resolutions are also the same. All operations conducted in Inverse Park module are done with pre-defined functions of NUMERIC_STD package. By using this package, signed operations could be handled easily.

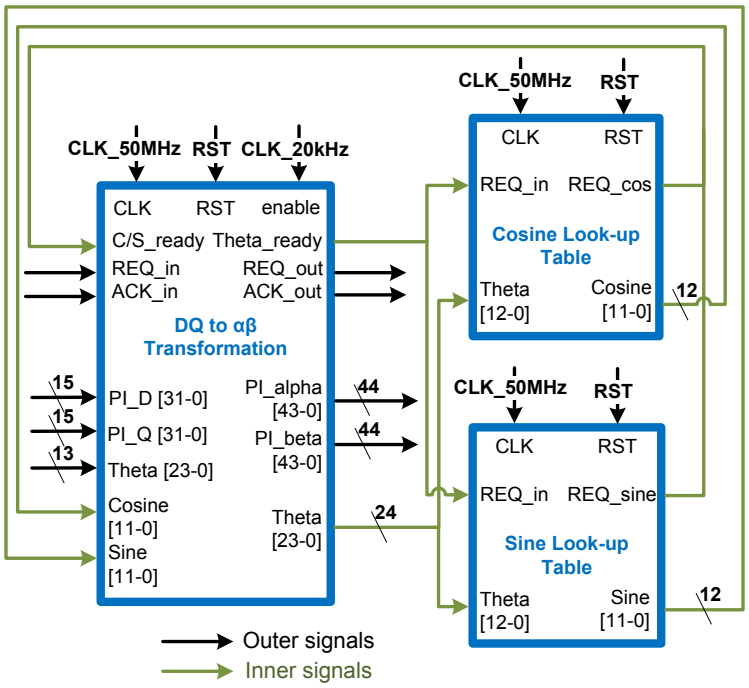

Figure 6.9: Inverse Park VHDL Block

6.1.5 Space Vector PWM Calculation

In this module, reference voltage and theta command are calculated to create pulse width modulation scheme for next cycle. There are two sub-modules of SVPWM Calculation module. They are responsible for calculation of V_{ref} and θ respectively according to Equations 3.15 and 3.16 mentioned in Subsection 3.5.1.

Magnitude of V_{ref} value is correlated with magnitude of active vectors which are shown in Figure 3.4. To reach greater magnitude in active vectors, open time durations of MOSFETs should be increased. Similarly, off time should be longer than on time for smaller V_{ref} values. The second equation is used for calculate θ. θ is an electrical angle and indicates on which angle space vector should be placed on next pwm cycle. Based on calculated θ, active base vectors are determined. It means that θ is used to decide the active sector.

Since magnitude and electrical angle of space vector directly affect produced torque, they should be calculated precisely. Therefore, XILINX Cordic IP is used for these calculations. CORDIC IP offers many mathematical functions for XILINX users. However, designer should define constraints and customize IP according to project's specifications. Tables 6.2 and 6.3 shows chosen adjustments for the scope of thesis.

In upper module which encloses root and arctangent IPs, some manipulations should be done in order to prepare inputs in a requested format. For example, $V_{\alpha}^2 + V_{\beta}^2$ expression is transformed from signed format into integer representation. V_{α} and V_{β} register widths are 24 bit. Therefore, input width of root function is chosen as 48 bit.

Although root function accepts integer inputs, arctangent function requires inputs in 2QN format number. This format is defined in IP manual [46] as "*An XQN format number is an 1+X+N bit twos complement binary number; a sign bit followed by X integer bits followed by an N bit mantissa (fraction).*". After transformation of input values into desired 2QN format, output register is multiplied with application specific constant to obtain theta value in previously defined electrical angle format.

Table 6.2: CORDIC IP for Root Function

Configuration Parameters	**Selections**
Data format	Unsigned Integer
Input Width	48
Round Mode	Truncated
Implementation Parameters	**Results**
Output Width	25
Latency	13

Table 6.3: CORDIC IP for Arctan Function

Configuration Parameters	**Selections**
Data format	Signed Fraction
Phase format	Scaled Radians
Input Width	24
Output Width	24
Round Mode	Truncated
Implementation Parameters	**Results**
Input Transaction Type	fix24_22
Output Transaction Type	fix24_21
Latency	27

6.1.6 Space Vector PWM Modulation

In previous section, working principle of sub-module, which is responsible for calculation of magnitude and angle parameters of reference vector, was explained. Basically, aim of this module is the regulation of PWM scheme for each cycle.

There are two prerequisites to handle PWM scheme such as sector detection and pulse time calculation. They are calculated in sub-modules under Space Vector PWM Modulation block. The following two subsections explain the procedure.

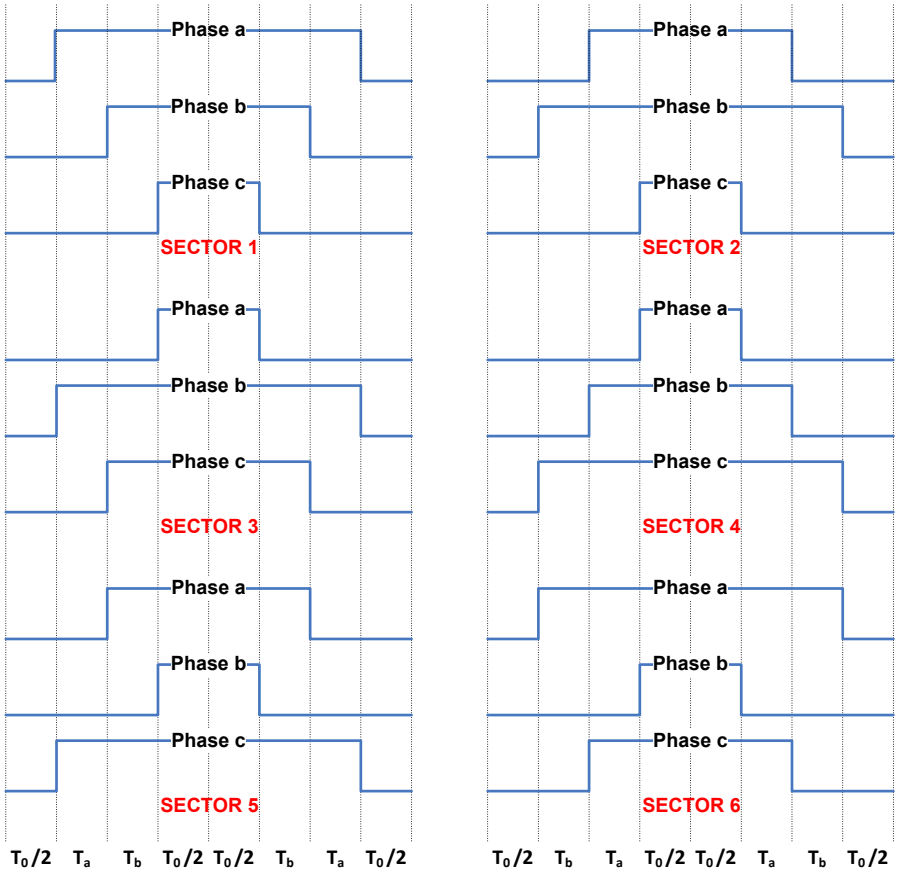

Figure 6.10: Switching Pattern

As previously mentioned in Section 3.5.3, symmetric PWM scheme is applied in our design. In Figure 6.10, pulse patterns for each sector are shown. It should be noticed that activation order of active vectors are different for odd numbered and even numbered sectors such as:

- For sector-2: $\overrightarrow{V_0}$, $\overrightarrow{V_3}$, $\overrightarrow{V_2}$, $\overrightarrow{V_7}$, $\overrightarrow{V_7}$, $\overrightarrow{V_2}$, $\overrightarrow{V_3}$, $\overrightarrow{V_0}$
- For sector-3: $\overrightarrow{V_0}$, $\overrightarrow{V_3}$, $\overrightarrow{V_4}$, $\overrightarrow{V_7}$, $\overrightarrow{V_7}$, $\overrightarrow{V_4}$, $\overrightarrow{V_3}$, $\overrightarrow{V_0}$

6.1.6.1 Sector Detection

The first step is determination of the sector in which V_{ref} lies. Each sector encloses sixty electrical degree and delimited by two of six basic space vectors denoted by V_1, V_2, V_3, V_4, V_5 and V_6. Additionally, there are two more vectors which are null

vectors. V_0 and V_7 have zero magnitude and are defined to complete eight state of active phases.

As can be seen Figure 3.4, each vector is mapped to 3 bit register. From left side to right, each bit represents phase-a, phase-b and phase-c respectively. For example, V_2 is linked by (110) means that phase-a and phase-b should be opened to create V_2. Similarly, assuming that V_{ref} lies in Sector-1, one can deduce that a and b phases should be energized during related pwm cycle.

6.1.6.2 SVPWM Pulse Time Calculation

The second step is calculation of pulse time duration based on sector and V_{ref} informations. By using Equation 3.19, switching time durations of adjacent space vectors could be found. T_a and T_b stand for required ON times of active space vectors which are represented by V_n and V_{n+1}, n is the sector number.

6.1.6.3 Space Vector Modulation Scheme

In Section 3.5.3, symmetric PWM scheme is offered for our implementation. Additionally, necessity of arrangement in SVPWM scheme is emphasized because of non-ideal nature of inverter circuitry. In Figure 6.11, MOSFET gates are numbered as shown.

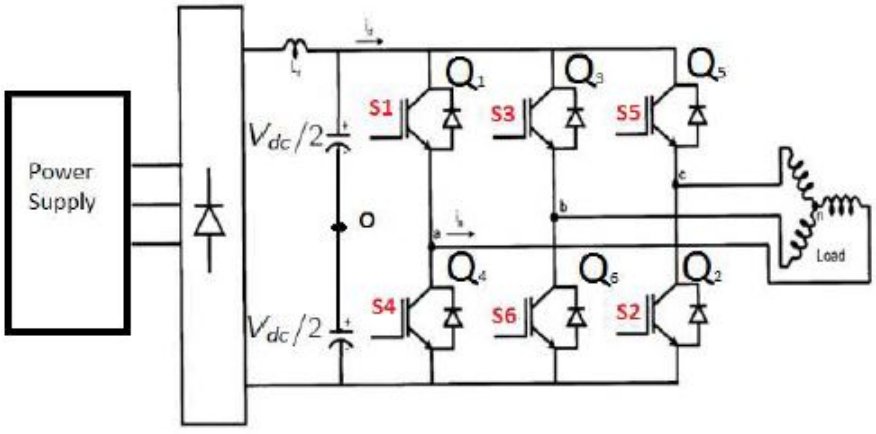

Figure 6.11: Three Phase Bridge Inverter

Figure 6.12 shows ideal switching order. On the other hand, Figure 6.13 represents actual scenario. Blue rows are added to enforce dead time delay. They are transition states and active only for 200 ns.

sector 1	S1	S2	S3	S4	S5
T0	0	1	0	1	0
T1	1	1	0	0	0
T2	1	1	1	0	0
T0	1	0	1	0	1
T0	1	0	1	0	1
T2	1	1	1	0	0
T1	1	1	0	0	0
T0	0	1	0	1	0

Figure 6.12: Ideal Gate States for Sector-1

sector 1	S1	S2	S3	S4	S5
T0	0	1	0	1	0
	0	1	0	0	0
T1	1	1	0	0	0
	1	1	0	0	0
T2	1	1	1	0	0
	1	0	1	0	0
T0	1	0	1	0	1
T0	1	0	1	0	1
	1	0	1	0	0
T2	1	1	1	0	0
	1	1	0	0	0
T1	1	1	0	0	0
	0	1	0	0	0
T0	0	1	0	1	0

Figure 6.13: Actual Gate States for Sector-1

6.2 Resolver Reading

Resolver is used to obtain position information of the rotor. It is known that resolvers are absolute sensors. Therefore, they give the same result whenever the certain positioning happens no matter how many revolutions are done.

Resolvers have some advantages over incremental sensors. Unlike incremental sensors, they do not need to re-home procedure at the start. Since the resolver gives a unique position value for each point in one turn, there is no need to make calculation

for each position command according to initial position. Instead of calculating the difference between target and current position, giving just target position is enough for resolvers.

Despite of advantages of resolver, one should take into consideration that knowing exact initial position is crucial in getting accurate position data. Therefore, a start-up method is suggested in this thesis. In order to map resolver digital data to mechanical position of rotor, certain reference point should be chosen. At the beginning of the operation, pre-determined motor phases are energized in certain amount of time. During this period, rotor is aligned certain electrical position. It should be noted that this aligned position might be different for different starting positions. Although every possible alignment point might differ in mechanical point of view, they have same electrical position value. This difference arises from multiple pole paired structure of the motor. Since electrical degree is multiplication of mechanical degree with pole pair number, one mechanical rotation corresponds to pole pair times of electrical rotation. In our case, there are sixteen pole pair; therefore, there are sixteen possible position for determined initialization pattern. It is expected that rotor is aligned to the nearest equilibrium point among these certain amount of possibilities.

In scope of this thesis, it is chosen that phase A and phase B are energised positively and negatively respectively for five seconds. During this time, alignment procedure is completed and rotor reaches destination point. After being sure of that rotor is stable, 64 samples are picked. Then their average is calculated. It is important to note that motor phases should be kept energized during sampling. Otherwise, rotor might be move away from equilibrium point. Equilibrium point could be found by looking at torque-angle curves of motor. Torque formula of one phase is given as:

$$T_n = -K_T * i_n * \sin\left((pp * \theta) - (n-1)\,\frac{2\pi}{3}\right) \tag{6.6}$$

where,

$T_n =$ Torque produced by phase n (Nm)

$K_T =$ Phase torque constant (Nm/A)

$i_n =$ Current in phase n (A)

$pp =$ Pole pair

$n =$ Phase number

CHAPTER 7

EXPERIMENTAL WORK

7.1 Introduction

Different tests have been conducted to verify the design. In this section, information about these tests will be given and discussed. The test setup consists of electronic board, KOLLMORGEN BM series permanent magnet synchronous motor, two power supplies, power and Ethernet cables, PC, oscilloscope, current probe, resolver and torquemeter. Additionally, a graphical user interface (GUI) is used to monitor controller's data and configure some controller parameters. Observed data is transferred from electronic board to GUI via Ethernet protocol.

In order to monitor data in GUI, it is necessary to collect data from different VHDL blocks and send them to processor side of SoC. Data acquisition block reads data from current controller and resolver VHDL blocks at 4 kHz sampling rate. Then, it sends this data to DDR through AXI (Advanced eXtensible Interface) Direct Memory Access (DMA). AXI is a bus protocol which defines how data is exchanged, transferred, and transformed. AXI DMA is a soft IP providing high-bandwidth direct memory access between memory and AXI4-Stream target peripherals.

For the purpose of proving asserted advantageous of FOC, the design is compared with the alternative one. The other design has PI controller and driven with six step commutation. Both of controller designs are implemented on the same electronic board. Additionally, used test setups are also the same.

7.2 Current Tests

In this setup, the motor is tested under no-load to obtain motor abc and dq currents. Currents are observed via GUI. It is expected that dq feedback currents follow dq

commands. In Figure 7.1, motor mechanism, which is used in current measurements, is given. Pair of dq command-feedback current graph is given in Figure 7.2 for rectangular 1500 mA_{pp} I_q and constant zero I_d current commands. As can be seen in Figure

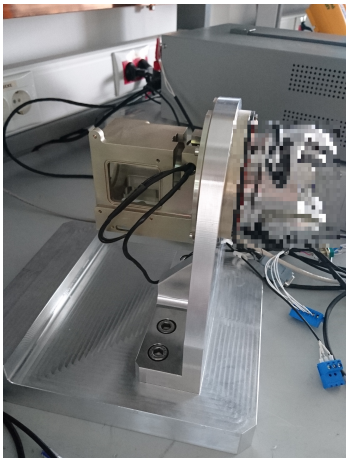

Figure 7.1: Laboratory Setup for Current Measurements

7.2, q axis current, which produces torque, tracks the current command efficiently. I_q current overshoot is measured as $\%4$ of the steady state value. Additionally, I_q current ripple is about 80 mA. Graph of phase currents in stationary domain is also given in Figure 7.3.

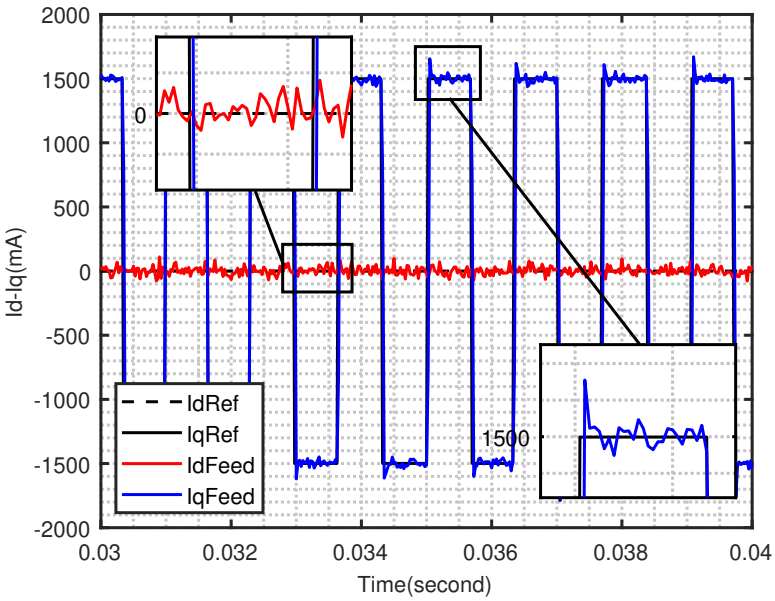

Figure 7.2: dq Current Response, $I_{d_ref} = 0A$, $I_{q_ref} = 1.5A_{pp}$ 300 Hz Rectangular Current Command

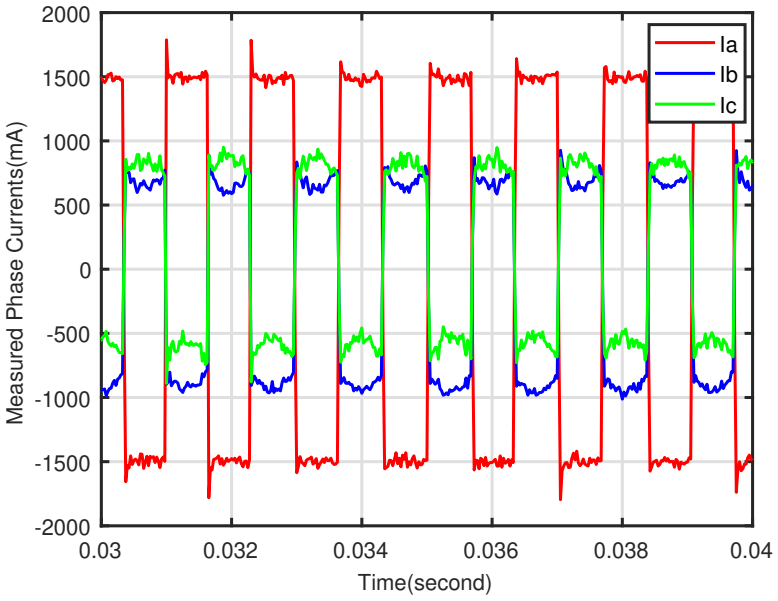

Figure 7.3: Phase Currents, $I_{d_ref} = 0A$, $I_{q_ref} = 1.5A_{pp}$ 300 Hz Rectangular Current Command

7.3 Torque Tests

The torque measurement tests are conducted by using dynamometer for both of the designs which are commutated by FOC and six-step strategy. In the following sub-sections, performances of FOC and six step commutation are illustrated with plots. The test procedure is as following:

1. The rotor is locked through a torquemeter and a coupling.
2. Step current command is applied to the tested motor.
3. Motor phase currents are measured by current sensors which are placed on the electronic board.
4. Collected current data is exported to GUI via Ethernet interface.
5. Measured torque data is collected by an industrial board at 4 kHz sampling rate.

In Figure 7.4, dynamometer, which is used during torque measurements, is given. The load motor, which is necessary for load tests, can be seen right-hand side of the mechanism. The motor under the test, which is marked by a red rectangle, should be

connected to left-hand side of the mechanism. Dynamometer is placed at the middle of two couplings. In torque figures, such as 7.5, the overshoot of the torque should

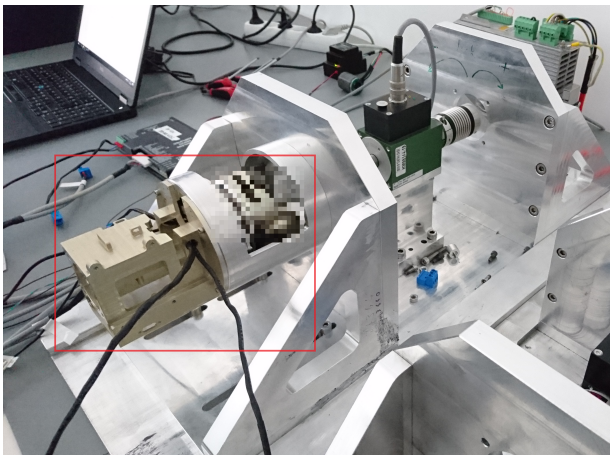

Figure 7.4: Locked Shaft Setup

be neglected due to the movement of the coupling with high spring constant. When a current is applied to the motor, motor applies a sudden torque to the coupling. As a result of this sudden torque, the coupling accelerates and this causes extra torque on the torquemeter for a small period of time.

7.3.1 Load Brake Results of FOC Commutation

Two different I_q values are chosen to be applied in no-load torque test. The first one is 1000 mA step command. Its torque response is given in Figure 7.5. Torque ripple is 5.1% of step command value at the steady state. As can be seen in Figure 7.6, there is

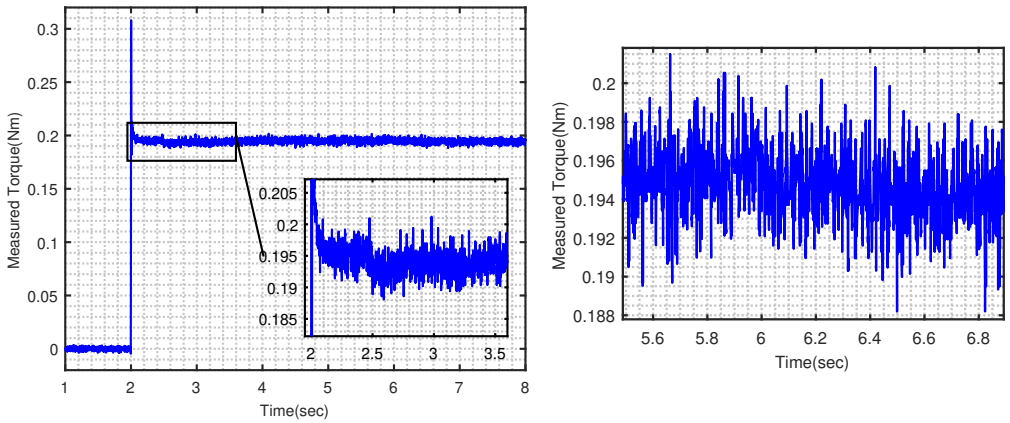

Figure 7.5: Measured Torque, 1000 mA I_q Command, FOC

no such a big overshoot unlike measured torque plot. The overshoot in torque graph results from the stiffness of couplings.

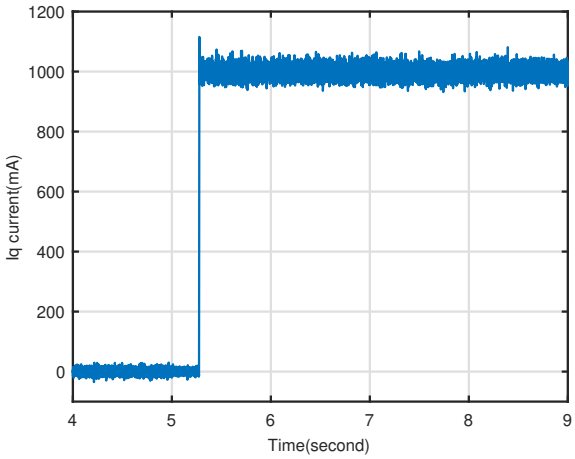

Figure 7.6: Measured I_q, 1000 mA I_q Command, FOC

The second current command has a square waveform. Its amplitude is 2500 mA_{pp}. The resultant torque response is shown in Figure 7.7.

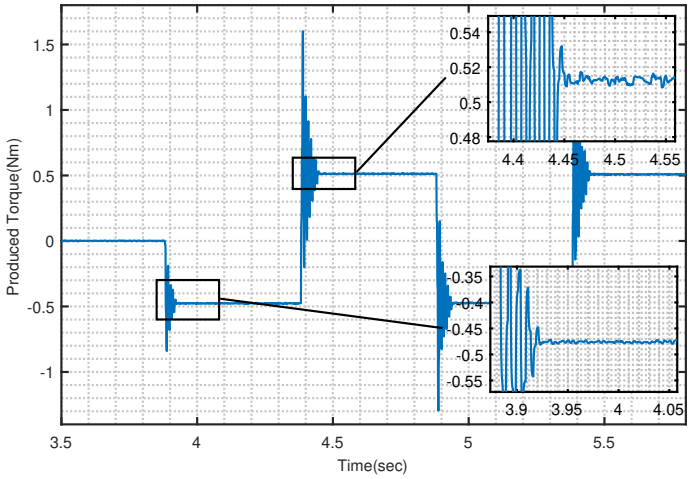

Figure 7.7: Torque Test under 2500 mA-pp Square I_q Current Command for FOC

7.3.2 Load Brake Results of Six-Step Commutation

Two different active phase current reference values are chosen to apply in load brake test. The first current command is 1000 mA. Its torque response is given in Figure 7.8. For 1000 mA current command, mean value of torque between time 8 and 13 is

equal to -0.173 Nm. Torque ripple is 4.6% of step command value. It should be noted

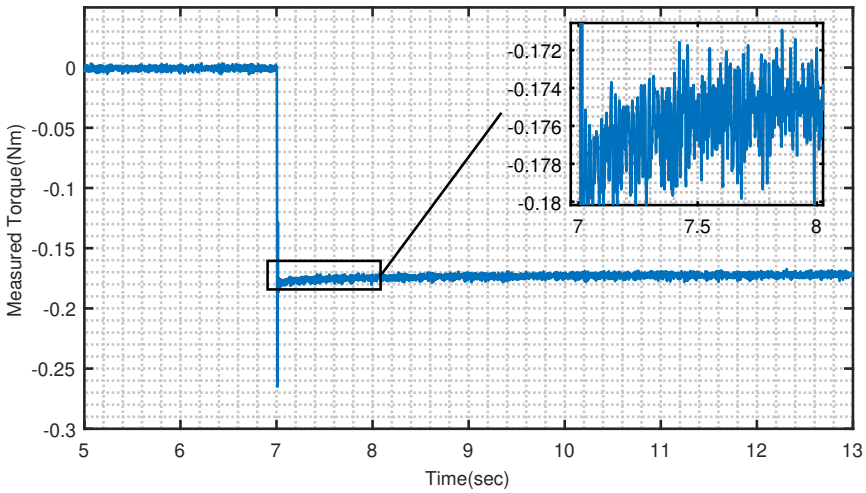

Figure 7.8: Measured Torque, 1000 mA Current Command, Six-Step Commutation

that frequency of current control loop is equal to 80 kHz. Although current loop of six-step driven system runs four times as fast as FOC driven system, current ripples of both systems are close to each other. Therefore, it is reasonable to say that current ripple of FOC based design will be smaller than trapezoidally commutated design when both of them have the same controller frequency. The second current command has a square waveform, which has 3000 mA_{pp} amplitude. The torque response is shown in Figure 7.9.

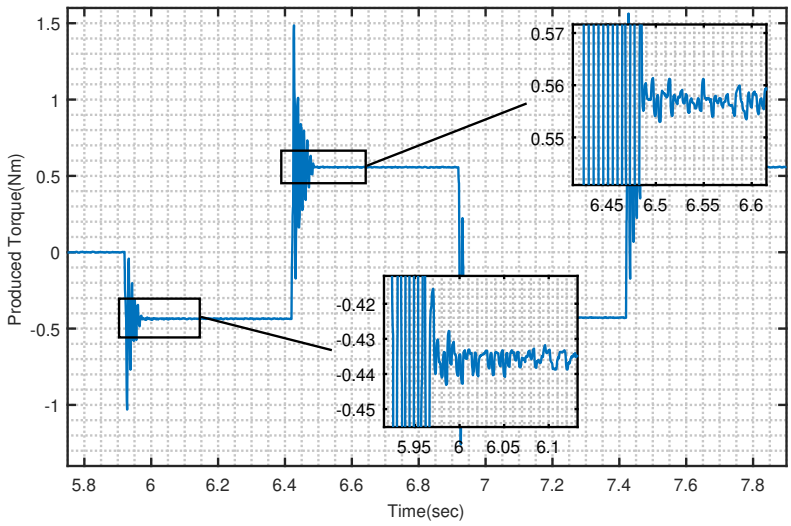

Figure 7.9: Measured Torque, 3000 mA_{pp} Square Current Command, Six-Step Commutation

7.4 Torque-Speed Tests

The torque-speed tests are conducted by using dynamometer for both FOC and six-step driven designs. In this test, load motor is connected to rotor of the tested motor to apply desired torque value. This load motor is externally controlled to produce a constant torque and it works in torque mode. The test procedure is as following:

1. Constant current command is applied to the tested motor.
2. The tested motor starts to rotate.
3. The load motor is started to apply the desired torque on the tested motor.
4. The coupled system (the tested and counter motor) starts to rotate in the direction of the tested motor.
5. Torque and speed graphs of tested motor are plotted.

There are overshoots in the speed graphics. These undershoots result from the resistance of the counter motor. Firstly, tested motor is started. Then, it rotates at no load speed. Secondly, counter motor is started. As a result of this, the tested motor tries to response to the counter motor. The overshoots, observed in the following figures, result from this sudden change of load.

7.4.1 Torque-Speed Results of FOC Commutation

Torque-speed results of FOC under constant current command, which is equal to 2000 mA, are given in Figures 7.10 and 7.11. The applied load torque is 0.3 Nm. Current controller response of FOC to constant current command, which is equal to 2000 mA, is given in Figure 7.11. Torque ripple value is about 7% of the steady state value. Current control loop frequency is equal to 20 kHz.

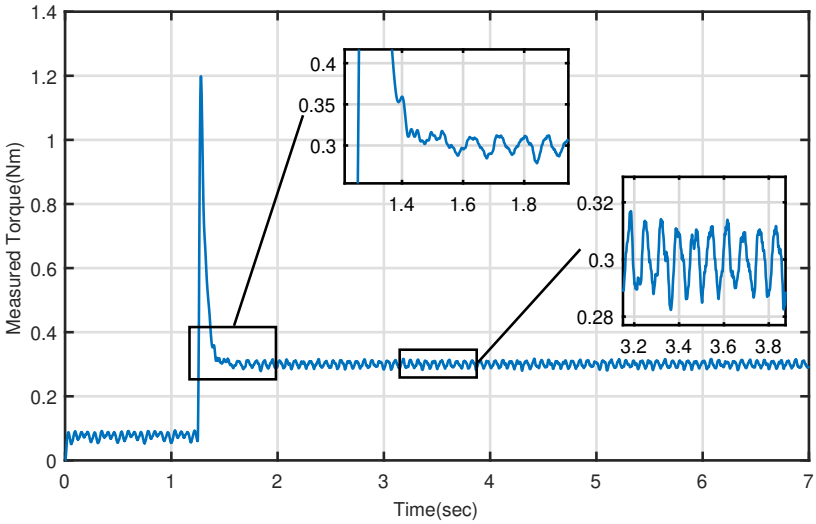

Figure 7.10: Measured Torque, 2000 mA I_q Command, 0.3 Nm Load, FOC

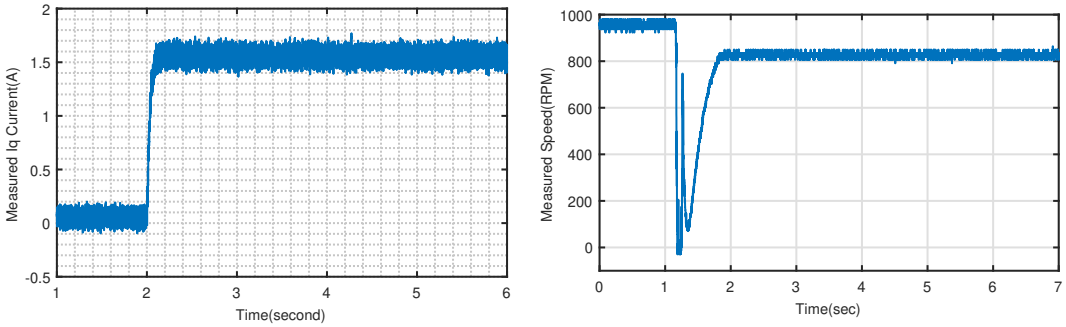

Figure 7.11: Measured I_q and Speed, 2000 mA I_q Command, 0.3 Nm Load, FOC

7.4.2 Torque-Speed Results of Six-Step Commutation

Torque-speed results of six-step commutated design under constant current command, which is equal to 3000 mA, are given in Figures 7.12 and 7.13. The applied load torque is 0.3 Nm. Current response to the constant current command is given in Figure 7.13. Torque ripple percentage is about 7.2% of the steady state value. Current control loop frequency is equal to 80 kHz, which is similar to the locked shaft experiment for six-step based design.

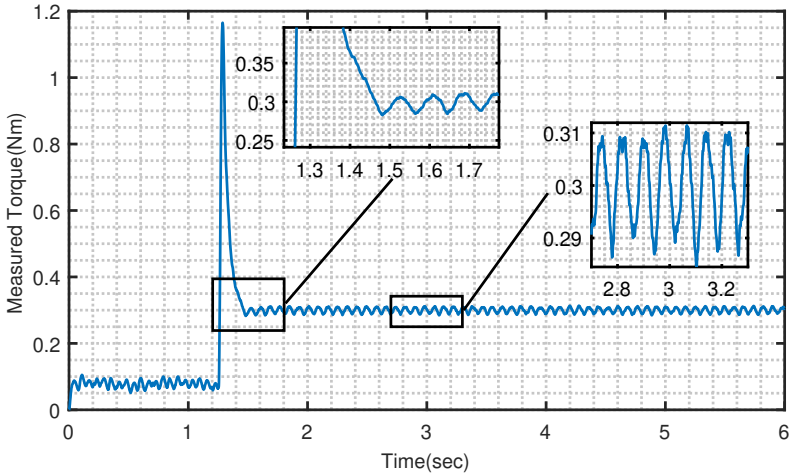

Figure 7.12: Measured Torque, 3000 mA Current Command, 0.3 Nm Load, Six-Step

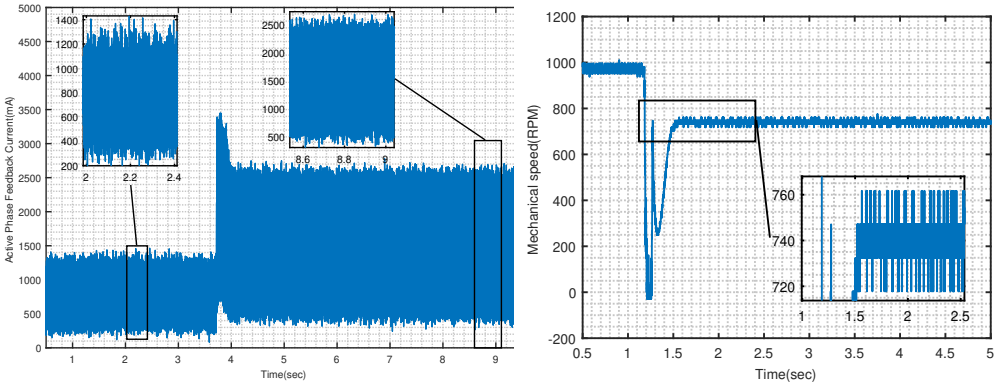

Figure 7.13: Measured Active Phase Current and Speed, 3000 mA Current Command, 0.3 Nm Load, Six-Step

7.5 Supply Current Measurement under Load Brake

The tested motor is locked then step current command is given to the interested control design. Magnitude of the current command is chosen separately for each design in order to force the controllers to produce the same amount of torque. After applying current command to the system, supply current, which is drawn from voltage source, is measured with oscilloscope by using current probe for both FOC and six-step driven designs. The test procedure can be summarized as following:

1. The rotor is locked through a torquemeter and a coupling.

2. Step current command is applied to the tested motor.

3. Drawn supply current from power supply is recorded

Torque and consumed supply current pairs are given in Figures 7.14 and 7.15 for FOC and six-step based designs respectively. While FOC based design requires approximately 670 mA supply current, six-step driven design requires approximately 900 mA supply current to produce the same amount of resultant torque. As can be

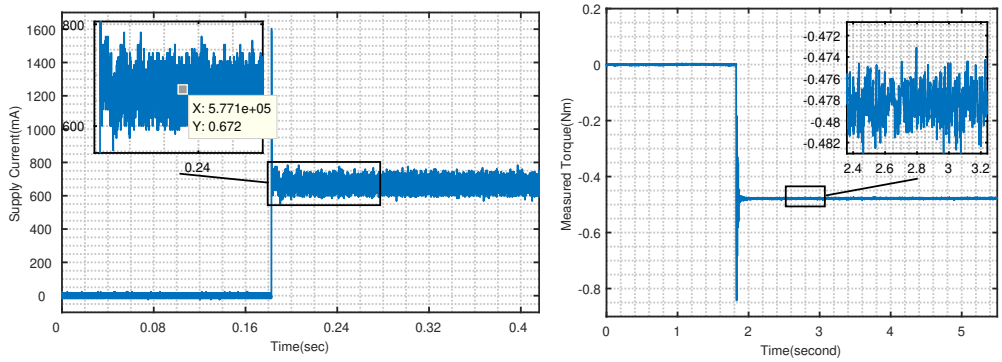

Figure 7.14: Measured Supply Current and Produced Torque, FOC

concluded from current plots, the supply current ripple is bigger in trapezoidal commutation as compared to FOC. Since switching rate of six-step is bigger than FOC, switching losses become bigger. Therefore, difference between observed supply current ripple band is what we have expected. However, ripple distinction cannot be clearly observed in torque plots because of comparatively lower sampling rate of torque measurement setup than sampling rate of oscilloscope.

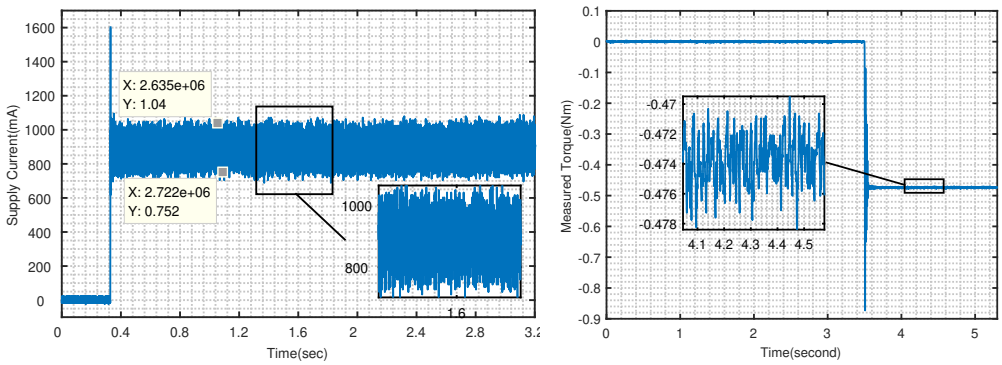

Figure 7.15: Measured Supply Current and Produced Torque, Six-Step

7.6 Discussion of the Results

It is observed that approximately the same percentage of torque ripple is measured during load brake tests of two controllers. Although six-step based design has three times bigger controller frequency rate, it cannot exhibit significant performance improvement in terms of torque ripple. Therefore, it can be concluded that FOC is advantageous over six-step because of lower control frequency rate requirement for approximately same percentage of ripple rate.

As controller frequency rate gets smaller, switching rate of MOSFETs also becomes smaller. Effect of smaller switching rate on power consumption is also demonstrated with previously measured supply current consumption for the same amount of produced torque. The second improvement does also result from decrease in MOSFET switching rate. By switching MOSFETs less frequently, it is expected that electromagnetic interference (EMI) is reduced. Finally, it becomes easier to cool the system due to the reduced amount of power, which transforms into the heat.

CHAPTER 8

CONCLUSION AND FUTURE WORKS

The purpose of the thesis is design and hardware implementation of field oriented control and space vector PWM. First of all, literature search has been done. General approaches to the related topic have been examined. During this examination process, comparison between different approaches has been made. As a result of this survey, the most convenient approach to the specified design has been chosen. Field oriented control method has lots of advantages over sinusoidal and six-step commutation methods such as efficiency and lower torque ripple. In the sinusoidal commutation technique, controlled motor phase currents are time-varying. When mechanical speed increases, it becomes more difficult to control the system because of narrower bandwidth of PI controllers. On the other hand, FOC offers wide operating range in terms of speed. That is why FOC method is chosen for the scope of the thesis.

In order to become familiar with concepts behind relevant theories, Simulink model has been constructed. Firstly, system components are modelled. Then, the controller methods, PI and LQR, are implemented. Their performance analysis under different test scenarios are done. As a result of this testing process based on simplified model, PI controller is decided to be implemented on hardware because of its efficiency/cost ratio.

After the simulation phase, hardware implementation on a SoC has been realized by using VHDL. It is no doubt that hardware implementation has been a challenging part of the thesis. After limitations, which result from hardware, have been detected, VHDL design has been completed. Finally, system performance has been examined under specified test condition in laboratory environment.

In Simulink Modelling and Experimental Work chapters, the design has been verified. The desired sinusoidally shaped phase currents have been obtained. Additionally, superior sides of FOC over classical trapezoidal driven PI based current controller

have been observed. As expected, accuracy of the controller is improved because of decrease in torque ripple.

As a result of the conducted study, improved and efficient version of current controller has been obtained. It is observed that there is a decrease in power consumption because of decrease in torque ripple. Additionally, frequency rate of current controller is reduced while torque ripple percentage is kept constant. As a result of this improvement, unnecessary MOSFET switching is prevented. It is the fact that results of performance test are satisfying. On the other hand, there is also a room for improvement in performance if there is enough resource and time. Some works to do can be summarized in the rest of the chapter.

As previously mentioned in Section 3.5.3, switching scheme is distorted because of non-ideal behaviour of switching circuitry, resulting from turn-on and turn-off time. Dead time worsens current tracking performance since it causes difference between commanded voltage and actual voltage. Decrease in current tracking ability means that distortion in phase currents hence created electromagnetic torque. There are some studies conducted to overcome this disturbance in literature. These studies may be divided into two main groups such as rearrangement of PWM scheme and application of feed forward control approach [39]. As a future direction of this study, dead time compensation control strategy can be implemented in SVPWM VHDL block to suppress distortions.

As mentioned in previous chapters, FOC method gives designer opportunity of working in wider operating region in terms of speed. If working above the rated motor speed is required, it can be accomplished by weakening stator field. Consequently, back EMF decreases and achieved speed increases. Therefore, arrangements on SVPWM strategy in order to create negative direct current component could be considered as the next improvement step.

In addition to improvement in VHDL part of SVPWM block, it is also possible to make rearrangement in hardware design of driver block. If switching MOSFETa and drivers can be faster, it is possible to work in higher switching rates. In consequence, torque ripple can be decreased even more.

REFERENCES

[1] W. Ahmed and S. M. U. Ali. Comparative study of svpwm (space vector pulse width modulation) & spwm (sinusoidal pulse width modulation) based three phase voltage source inverters for variable speed drive. In *IOP Conference Series: Materials Science and Engineering*, volume 51, page 012027. IOP Publishing, 2013.

[2] B. Akin and M. Bhardwaj. Trapezoidal control of bldc motors using hall effect sensors. *Texas instruments*, 2010.

[3] Q. Al azze. Field-oriented control of permanent magnet synchronous motors based on dsp controller. Master's thesis, Graduate School Southern Illinois University Edwardsville, May 2014.

[4] Analog Devices. *AD7944 Data Sheet*, Feb. 2016.

[5] K. J. Astrom and L. Rundqwist. Integrator windup and how to avoid it. In *1989 American Control Conference*, pages 1693–1698. IEEE, 1989.

[6] V. M. Bida, D. V. Samokhvalov, and F. S. Al-Mahturi. Pmsm vector control techniques — a survey. In *2018 IEEE Conference of Russian Young Researchers in Electrical and Electronic Engineering (EIConRus)*, pages 577–581, Jan 2018.

[7] A. Bolopion, D. Jouve, and R. Pacaut. Control of permanent magnets synchronous machines: a simulation comparative survey. In *Fifth Annual Proceedings on Applied Power Electronics Conference and Exposition*, pages 374–383. IEEE, 1990.

[8] S. Colton. Flux observer-based sensorless field-oriented control of surface permanent magnet synchronous motors (gen. 1), 2014.

[9] H. V. Deo and R. Shekokar. A review of speed control techniques using pmsm. *Int. J. Innov. Res. Technol*, 1(11):2349–6002, 2014.

[10] S. K. Dwivedi, M. Laursen, and S. Hansen. Voltage vector based control for pmsm in industry applications. In *2010 IEEE International Symposium on Industrial Electronics*, pages 3845–3850. IEEE, 2010.

[11] X. d. T. Garcia, B. Zigmund, A. A. Terlizzi, R. Pavlanin, and L. Salvatore. Comparison between foc and dtc strategies for permanent magnet synchronous motors. *Advances in Electrical and Electronic Engineering*, 5(1):76–81, 2011.

[12] A. Ghoshal and V. John. Anti-windup schemes for proportional integral and proportional resonant controller. 2010.

[13] M. Gowda, W. H. Ali, P. Cofie, and J. Fuller. Design and digital implementation of controller for pmsm using extended kalman filter. *Circuits and Systems*, 4(08):489, 2013.

[14] A. Gupta and S. Kumar. Analysis of three phase space vector pwm voltage source inverter for asd's. *International Journal of Emerging Technology and Advanced Engineering*, 2(10):163–168, 2012.

[15] A. Hassan, M. Arif, A. R. Abdullah, N. Bahari, M. Sabri, and M. Ihsan. Efficiency comparison of trapezoidal and sinusoidal method for brushless dc motor drive. In *Applied Mechanics and Materials*, volume 785, pages 248–252. Trans Tech Publ, 2015.

[16] S. Hussain and M. A. Bazaz. Comparative analysis of speed control strategies for vector controlled pmsm drive. In *2016 International Conference on Computing, Communication and Automation (ICCCA)*, pages 1314–1319. IEEE, 2016.

[17] International Rectifier. *StrongIRFET IRF7580MTRPbF*, May 2015.

[18] K. Jash, P. K. Saha, and G. K. Panda. Vector control of permanent magnet synchronous motor based on sinusoidal pulse width modulated inverter with proportional integral controller. *International Journal on Engineering Research and Applications*, 3:913–917, 2013.

[19] D. Jouve, J. Rognon, and D. Roye. Effective current and speed controllers for permanent magnet machines: A survey. In *Fifth Annual Proceedings on Applied Power Electronics Conference and Exposition*, pages 384–393. IEEE, 1990.

[20] E. Klintberg. Comparison of control approaches for permanent magnet motors. *Master of Science Thesis*, pages 1–76, 2013.

[21] Kollmorgen. Bm(s) series motors. Technical report, Kollmorgen.

[22] K. V. Kumar, P. A. Michael, J. P. John, and S. S. Kumar. Simulation and comparison of spwm and svpwm control for three phase inverter. *ARPN journal of engineering and applied sciences*, 5(7):61–74, 2010.

[23] Y.-S. Kung and M.-H. Tsai. Fpga-based speed control ic for pmsm drive with adaptive fuzzy control. *IEEE Transactions on Power Electronics*, 22(6):2476–2486, 2007.

[24] C.-K. Lai, Y.-T. Tsao, and C.-C. Tsai. Modeling, analysis, and realization of permanent magnet synchronous motor current vector control by matlab/simulink and fpga. *Machines*, 5(4):26, 2017.

[25] S. Lee, T. Lemley, and G. Keohane. A comparison study of the commutation methods for the three-phase permanent magnet brushless dc motor. *Pennsylvania State Univ. Berks Campus*, pages 3–5, 2014.

[26] LEM. *Current Transducer HO-NSM series*, version7 edition, May 2018.

[27] J. Lemmens, P. Vanassche, and J. Driesen. Pmsm drive current and voltage limiting as a constraint optimal control problem. *IEEE Journal of emerging and selected topics in power electronics*, 3(2):326–338, 2014.

[28] F. Lewis. Linear quadratic regulator (lqr) state feedback design. *Lecture notes in Dept. Elect. Engineering, University of Texas, Arlington*, 2008.

[29] M. Macchini. *Motion control design of a PMSM and FPGA implementation for the Beam Wire Scanner at CERN*. PhD thesis, Pisa U., 2015.

[30] MathWorks. Park transform, Sept. 2019.

[31] P. Pillay and P. Freere. Literature survey of permanent magnet ac motors and drives. In *Conference Record of the IEEE Industry Applications Society Annual Meeting,*, pages 74–84. IEEE, 1989.

[32] P. Pillay and R. Krishnan. Modeling of permanent magnet motor drives. *IEEE Transactions on industrial electronics*, 35(4):537–541, 1988.

[33] N. V. Quynh and Y.-S. Kung. Fpga-realization of fuzzy speed controller for pmsm drives without position sensor. In *2013 International Conference on Control, Automation and Information Sciences (ICCAIS)*, pages 278–282. IEEE, 2013.

[34] A. Rachid and B. I. Badr. Experimental assessment of trapezoidal commutation and foc performances of 3-phase permanent magnet brushless motor.

[35] R. T. Ramamoorthy, B. Larimore, and M. Bhardwaj. Sensored field oriented control of 3-phase permanent magnet synchronous motors using tms320f2837x. 2016.

[36] P. Ramana, B. S. Kumar, K. A. Mary, and M. S. Kalavathi. Comparison of various pwm techniques for field oriented control vsi fed pmsm drive. *International journal of advanced research in electrical, electronics and instrumentation engineering*, 2(7):2928–2936, 2013.

[37] M. T. Ratcliffe and K. A. Gamage. Bldc motor power control techniques appraisal: Novel current control technique. In *4th International Conference on Power Engineering, Energy and Electrical Drives*, pages 1700–1705. IEEE, 2013.

[38] W. A. Salah, D. Ishak, and K. J. Hammadi. Minimization of torque ripples in bldc motors due to phase commutation-a review. *Przeglad Elektrotechniczny*, 87(1):182–188, 2011.

[39] J. Shi and S. Li. Analysis and compensation control of dead-time effect on space vector pwm. *Journal of Power Electronics*, 15(2):431–442, 2015.

[40] N. Sorokin. Implementation of high-speed fixed-point dividers on fpga. *Journal of Computer Science & Technology*, 6, 2006.

[41] M. Y. Sumon. *An Analysis and Improvement of Brushless DC Motor Control System*. PhD thesis, North Dakota State University, 2013.

[42] P. H. Tran. Matlab/simulink implementation and analysis of three pulse-width-modulation (pwm) techniques. Master's thesis, 2011.

[43] A. P. Tripathi, V. Singh, and A. Patidar. Permanent magnet synchronous motor voltage vector control by simulation. *International Journal of Scientific & Engineering Research*, 3(12), 2012.

[44] S. Uygur. An fpga based bldc motor control system. Master's thesis, Middle East Technical University, Feb. 2012.

[45] V. Veena, S. Achari, M. Ravichandran, and R. Praveen. Vector control of three phase pmsm drive using power transformations for future spacecraft application. In *2014 International Conference on Circuits, Power and Computing Technologies [ICCPCT-2014]*, pages 313–319. IEEE, 2014.

[46] XILINX. *CORDIC v6.0 LogiCORE IP Product Guide*, Dec. 2017.

[47] W.-J. Xu. Permanent magnet synchronous motor with linear quadraticspeed controller. *Energy Procedia*, 14:364–369, 2012.

[48] L. Yongdong and Z. Hao. Sensorless control of permanent magnet synchronous motor—a survey. In *2008 IEEE Vehicle Power and Propulsion Conference*, pages 1–8. IEEE, 2008.

[49] J. Zambada and D. Deb. Sensorless field oriented control of a pmsm. *Microchip Technology Inc*, 2010.